Modeling Studies Related to Carbon Dioxide Phase Change on Mars

Thesis by

Xin Guo (郭心)

In Partial Fulfillment of the Requirements

for the Degree of

Doctor of Philosophy

California Institute of Technology

Pasadena, California

2009

(Defended, April 29th, 2009)

To my grandfather

献给我的外公

Acknowledgements

My grandfather passed away before the birth of mine and I have never had the chance to meet him. From the discrete memories of my other family members, I established a great image of him. To me, he is the most talented person with knowledge and integrity who unfortunately lived in an era of turbulence. Perhaps I will never be able to achieve what he had, but I try my best. I believe traditions need to, and will be carried on.

I can not imagine who I would become without the love, help, and support from my family. My father always shows me how to earn others' respect by hard working; my mother teaches me how powerful unselfishness and encouragement can be; my grandparents, along with my uncles, aunts, and cousins, simply spoil me with pure affectionateness. I consider myself to be extremely lucky to have such a wonderful family.

I want to express my most sincere appreciations to my advisors: Prof. Mark Richardson, Prof. Yuk Yung, Prof. Andrew Ingersoll, and Prof. Oded Aharonson. I have been granted a wealth by these distinguished scholars. Not only from the world-class scientific research have they conducted but also from their inspiring ways of living. Prof. Richardson is, in my opinion, an extremely strong person because he remains optimistic and welcoming at any circumstances. Prof. Yung exhibits a superb example of dedication, strictness and generosity. Prof. Ingersoll is an ideal mentor both inside and outside of work. Prof. Ahronson's insightfulness and sharpness are just extraordinary.

I have benefited greatly from my colleagues within Prof. Richardson's research group, Prof. Yung's research group and other co-workers, including Dr. Claire Newman, Dr. Run-Lie Shia, Dr. W. Gregory Lawson, Dr. Chris Lee, Dr. Anthony Toigo, Dr. Inada Ai, Dr.

Vijay Natraj, Dr. Stanley Sander, Dr. Stephen Wood, Dr. Michael Mischnna, Mr. Ian McEwan, Prof. Xianglei Huang, Dr. Jack Magolis, Prof. Xun Jiang, Dr. Liming Li, Dr. Mao-Chang Liang, and Prof. Jess Adkins. In different ways, they have helped me to understand the scientific subjects and to improve my relevant skills.

My first time adapting to a foreign culture was made unforgettable by my precious friends in Geological and Planetary Sciences. I cherish the memories I share with Kevin Lewis, Kristina Barkume, Sloane Wiktorowicz, Colette Salyk, Richard Wildman, Carl Tape, Yoshihiro Kaneko, Kaveh Pahlevan, Alejandro Soto, Margarita Marinova, Dan Feldman, and Ravi Kanda. Nevertheless, life in southern California would not be so wonderful without my friends, including Lin Zhu, Yi Liu, Ling Zheng, Xiao Lu, Zhiyi Li, Ling Shi, Daoyuan Sun, Yu Liu, Changlin Pang, Cheng-Zhong Zhang, George Ouyang, Hao Jiang, Jie Cheng, Li Liu, Bo Li, Yue Zou, Dongping Zhuang, Fei Wang, Ying Wang, Mo Li, Ru He, Lin Han, Ming-Shr Lin, and Hsin-Ying Chiu, who are also far away from their beloved homeland. During my stay in the United States, constant warm supports have kept coming from my adorable friends at distance, including Ralph Wan, Kirby Zhou, Elaine Chang, Collin Xiong, Dirk He, Ken Yuan, Floyd Jiang, Frank Hu, Stewart Yang, Janet Liu, Peimin Zhang, Bill Wang, Rick Liu, Tammy Tan, Penny Yin, Red Zhu, Sonny Song, George Wang, Cavvie Li, Jue Wang, Yong Liu, Min Hu, Rainie Jiang, and Tina Teng. I consider them as my brothers and sisters from my previous lives.

Last but not least, I present my most special thanks to Ms. Susie Zhu, who is the most brilliant, enlightening, graceful, and beautiful woman. I wish we can forever be together to explore this wonderful world.

致谢

我的外公在我出生之前就已经去世，我也从来没有见过他。从我家人关于他零星的记忆中，我只对他有模糊但却又清晰的了解。对我来说，他的天份高不可及。在那动荡的年代，他仍是正直和智慧的楷模。我也许永远无法企及他的高度，但我会尽我最大的努力。我深信传统需要、也必将得到传承。

家人的宠爱、帮助和支持伴随我至今。我的父亲教我如何通过努力工作来得到别人的尊敬；我的母亲让我懂得什么叫做无私，怎样鼓励他人；我的外婆、爷爷、奶奶、叔叔、婶婶和两个堂妹给予我无穷的关心和爱护。我为能拥有这样的一个家庭感到无比幸运。

我把最诚挚的感谢呈给我的博士论文导师们： Mark Richardson 教授、翁玉林教授、Andrew Ingersoll 教授和 Oded Aharonson 教授。从这些杰出的学者身上，我获得了能享用一生的财富。不单是有幸同他们一起进行一流的科学研究，他们独特的生活方式对我也是极大的启发。Richardson 教授在我眼中是个无比坚强的人，他能在任何逆境中保持乐观和进取心。翁玉林教授展示了奉献、严厉与慷慨大度的完美结合。Ingersoll 教授在工作和生活中都是良师益友。Aharonson 教授的智慧和洞察力令人折服。

我在同 Richardson 教授的研究组，翁玉林教授的研究组以及其他同事的合作和交流中受益良多。我要特别感谢 Claire Newman 博士、夏仁立博士、W. Gregory Lawson 博士、Chris Lee 博士、Anthony Toigo 博士、稻田爱博士、Vijay Natraj 博士、

Stanley Sander 博士、Stephen Wood 博士、Michael Mischnna 博士、Ian McEwan 先生、黄向磊教授、Jack Magolis 博士、蒋寻博士、李黎明博士、梁茂昌博士和 Jess Adkins 教授。从各个不同的方面，他们帮助我加深对科研课题的理解，帮助我提高科学研究的技能。

我第一次在陌生的国度生活，就有地质与行星科学系的朋友们热情地帮我融入异国文化。特别要感谢的是 Kevin Lewis、Kristina Barkume、Sloane Wiktorowicz、Colette Salyk、Richard Wildman、Carl Tape、Yoshihiro Kaneko、Kaveh Pahlevan、Alejandro Soto、Margarita Marinova、Dan Feldman 和 Ravi Kanda。与他们共同拥有的美好的记忆将令我终生难忘。在南加的生活能够如此精彩，我还要感谢同我一样在远离我们深爱的家乡生活的好友们。他们是朱林、刘轶、郑聆、陆骁、李智一、施凌、孙道远、刘宇、庞长林、张承中、欧阳晓溪、姜浩、成捷、刘莉、黎波、邹悦、庄东平、王菲、王莹、李墨、何如、韩琳、林明仕和邱馨颖。在美国留学的日子，热情的鼓励源源不断的来自我世界各地的挚友。万聪、周天凌、常青、熊小年、何旷、袁远、姜毅、胡一鹏、阳萌、刘晶、张沛敏、王琼、刘远、谭琳、尹潘嵘、朱丹、宋卓、王智、黎元春、王珏、刘勇、胡敏、姜晓雨和滕牵，他们就像我的隔世兄弟。

最后，我把最特别的感谢送给朱彬小姐。她是一位非常非凡的女性，集聪明和才智，美丽和优雅于一身。我希望我们能永远在一起，看万千世界。

Abstract

Carbon dioxide (CO_2) is the most abundant gaseous species in the atmosphere of Mars. Phase change of CO_2, predominantly between gas and solid, is the most eminent feature in the current Martian atmosphere. Correct and thorough understanding of the CO_2 cycle on Mars is crucial to the scientific research of Mars, including (but not limited to) climatology, meteorology, paleo-climatology, geomorphology, geology, and astrobiology.

I modeled the CO_2 phase change and couple the process with a Mars General Circulation Model (GCM) — the Mars Weather Forecast and Research (MarsWRF) model. Two major forms of the CO_2 phase change are included: direct deposition/sublimation to/from the surface (exchange with surface frost) and atmospheric condensation/evaporation (exchange with "snow", which later will either precipitate to the ground and become a part of the surface reservoir, or evaporate before it reaches the surface).

The first component has been historically simulated by a surface energy balance model. I improved the energy balance calculations in MarsWRF, especially improved the physics module associated with subsurface heat conduction. I fine-tuned the GCM by changing the values of the seasonal ice cap albedos and emissivities and the total CO_2 mass in the system. The resulting pressure cycle, which is a good indicator of the atmospheric reservoir of CO_2 in the system, matches the *in situ* measurements by the Viking Landers extremely well. This linear fitting algorithm can be used for future tuning of other GCMs and for searching for more complicated physics.

The second component can be solved by a simple energy balance model in the atmosphere as well. However, it is widely accepted that sophisticated microphysics models

may be required for more accurate simulations. I incorporated a complete microphysics model, which calculates the nucleation process and ice particle growth process, to MarsWRF. Preliminary simulation results show promising agreement with spacecraft data.

When I include an insolation-dependent frost albedo, as suggested by various spacecrafts, to the GCM, MarsWRF is able to produce a perennial CO_2 cap near the south pole of Mars. This is the first time that any GCM has successfully predicted a residual cap. I show that this mechanism is necessary for a simple energy balance model to reproduce the perennial ice cap, and may shed some light on the ages and the cycles of the perennial caps.

I develop a mass balance model to simulate the non-condensable gas mass mixing ratio variation during the CO_2 phase change. When coupled with MarsWRF, the non-condensable gas cycle agrees qualitatively with the Gamma Ray Spectrometer data and other GCM results. It provides a benchmark check to the GCM itself and an independent way to study the dynamics of the Martian atmosphere.

摘要

二氧化碳是火星大气层最主要的组成部分。它在气态与固态之间的相变过程也是火星大气中最显著的特征。建立对二氧化碳循环正确而全面的理解对火星研究的各个方面——包括气候学、气象学、古气候学、地貌学、地质学和天体生物学，都至关重要。

我把一套完整的二氧化碳相变模拟模型整合到一个火星大气环流模型——MarsWRF，中。这套相变模型一共有两个部分：地表的凝华/生华（大气与地面冰层的交换过程）和大气层中的凝华/生华（大气与二氧化碳冰雪的交换。冰粒有可能通过降雪落到地面，也有可能在降落到地表之前完全升华）。

一般来说，使用简单的地表面能量守恒就能很好的模拟第一部分（地表相变）的相变。通过改进已有的数值计算方法，我让土壤模型能够解决垂直方向上各向不同性介质的热传导问题，并通过精细调节地表冰盖的反照率和吸收率以及系统中二氧化碳的总量对已有数据进行拟合。微调模型后模拟得到的地表压强与维京人号火星登陆器测量到的数据非常吻合。所使用的线性回归方法也能在其他很多问题上使用，比如它可以被拓展到关于火星土壤性质的探索。

第二部分（大气中的相变）也能用类似的能量守恒方程求解。但随着对精确的需求的提高，学界对微观物理模型也越来越受到重视。我把一套精确的微观物理模型整合到 MarsWRF 中来计算二氧化碳冰粒的聚核过程和生长过程。在现阶段简化模拟的结果也与卫星观测基本吻合。

如果在 MarsWRF 中假设二氧化碳冰盖的反照度会随着入射太阳光强变化，在火星南极的附近会产生一个永不消失的结冰区域。这是第一次用火星大气环流模型成功模拟这一现象。我证明了这一反照度与入射光的关系是解释形成永冻区域的基础。此结果可能会影响到对火星极区永冻区域存在周期的分析。

此外，根据质量守恒，我建立了一套模型用来模拟伴随二氧化碳相变的惰性气体混合度变化。我把用 MarsWRF 模拟得到不凝固气体的周期并同伽玛射线光谱仪的观测结果和其他模拟结果进行比较。这一工作为进一步检测所使用的大气模型的正确性和研究火星大气动力学提供了一个独立方法。

Table of Contents

Chapter 1: Introduction

Mars is the closest neighbor to our very own Earth in the solar system. The earliest observation of Mars dates back to the ancient Greece, when Aristotle described it passing behind the moon. Telescopic observation of Mars was started by Galileo in 1609. In the 19th century, pioneered by Giovanni Schiapareilli and followed by Percival Powell, surface map of Mars was compiled. The discovery of *canali* (channels, mistranslated to canals in English) and seasonal polar cap caused great public interest at that time. Most of the speculation was about life on Mars[1].

The flyby of Mariner 4 in 1965 marks the beginning of modern Mars exploration, which the United States, the Soviet Union (later Russia), Europe, and Japan have put much effort into ever since. The booming age of Mars exploration started with the Viking missions in 1970s. While the returned data suggested a frigid and life-less Martian environment, the attention was moved away from Mars. Starting from late 1990s, a new generation of space missions revolutionized people's view of this red planet. A treasure of data was provided by the Mar Global Surveyor, the Mars Pathfinder, the 2001 Mars Odyssey, the Mars Express orbiter, the Mars Exploration Rovers, the Mars Reconnaissance Orbiter, and the Phoenix Lander. It makes research in Mars' evolution history, current environment, and even future utilization of human possible and valid.

[1] http://en.wikipedia.org/wiki/Mars

Among many research topics in Mars Science, atmospheric science is one of the most interesting and important subjects. This dissertation is devoted to different modeling studies related to the phase change of the most abundant atmospheric species, carbon dioxide (CO_2), on Mars. My work is designated to contribute to human being's understanding of Mars and to improve the current tools available for relevant scientific research.

1.1 Cycles in the atmosphere of Mars

CO_2 is the most abundant gas in the atmosphere of Mars. 95% of the atmosphere is comprised of CO_2, alone with nitrogen (N_2, 2.7%), argon (Ar, 1.6%), oxygen (O_2, 0.13%), carbon monoxide (CO, 0.07%), water vapor (H_2O, 0 to 300 ppm), and methane (CH_4, 0 to 50 ppb) [*Krasnopolsky et al.*, 2004; *Mumma et al.*, 2009; *Owen et al.*, 1977].

Phase change of CO_2, predominantly between gas and solid, is the most eminent feature in the current Martian atmosphere. In this annual (or seasonal) CO_2 cycle, up to 30% of the atmosphere condenses[2] at the winter polar region (in this sense, we address the rest of the gaseous species, except for water vapor, "non-condensable" gas as opposed to the "condensable" CO_2), causing the surface to vary by a few hundreds of Pascal [*Hess et al.*, 1977; *Hourdin et al.*, 1993; *Kelly et al.*, 2006], which is very different and more volatile compared to earth's atmosphere. On the other hand, as on earth, CO_2 is the leading greenhouse gas on Mars. The much denser CO_2 atmosphere in ancient times is speculated to

[2] Strictly speaking, condensation/evaporation refers to the phase change from gas to liquid, while deposition/sublimation refers to the phase change from gas to solid (http://en.wikipedia.org/wiki/Phase_change). However, the Mars science community has had a history of loosely using the verbs condense/evaporate to describe the gas/solid exchange of CO_2. Therefore, I will follow the convention of the community by using condense/evaporate interchangeably with deposit/sublimate.

aid the long term existence of liquid water on the surface of Mars [*Mischna et al.*, 2000]. More importantly, CO_2 is the dominant gas in the atmosphere, or essentially the atmosphere itself. In the air-land system, it is the most active element, which buffers the solar power, distributes atmospheric mass, energy, momentum and tracers, and interacts with the surface. An accurate understanding of its behavior is crucial to every aspect of scientific research on Mars including (but not limited to) climatology, meteorology, paleo-climatology, geomorphology, geology, and astrobiology.

Another important cycle on Mars is that of the airborne dust. The first half of a Martian year (Ls[3] 0° to 180°) is usually characterized by clear air while the second half (Ls 180° to 360°) is very dusty, sometimes even with global dust storms [*Smith et al.*, 2002]. Repeatable cycles with inter-annual variability is evident from spacecraft observations [*Smith*, 2004]. Airborne dust increases the air temperature by absorbing solar radiation [*Richardson*, 1998] and participates in the cloud formation process as nuclei [*Colaprete et al.*, 2008; *Wood*, 1999]. When landed on surface, it may also modify the surface albedos in a global scale [*Fenton et al.*, 2007; *Szwast et al.*, 2006]. Much modeling studies about the origin, annual variation and inter-annual variability of the dust cycle have been done in previous literatures [*Basu et al.*, 2004; *Basu et al.*, 2006; *Newman et al.*, 2002a; b]. In my thesis, if not specified, I usually model the dust cycle on Mars using climatology data ensemble from satellite observation and exclude the inter-annual variability for radiative calculations.

[3] Ls, an abbreviation to solar longitude or heliocentric longitude, is used to define the location of a planet on its elliptical orbit. A year is divided to 360° of Ls. Once the planet is at the northern vernal equinox, Ls is defined as 0°; consequently, 90° for northern summer solstice, 180° for northern autumn equinox and 270° for northern winter solstice. It roughly maps to the 365 days on earth. A Martian year has roughly 669 sols (Mars days), therefore 1 degree of Ls is roughly 2 sols. 12 months can be defined as each month contains 30° of Ls. See also http://www-mars.lmd.jussieu.fr/mars/time/solar_longitude.html

Water vapor is released from the northern cap in northern spring and summer. It allows the formation of a water ice cloud belt over the equatorial region during northern summer [*Smith*, 2002; 2004]. The water cycle has also been explored by modeling studies [*Richardson and Wilson*, 2002b; *Richardson and Mischna*, 2005]. However, due to its relatively small amount, I consider its impact to the current Mars climate as second order, especially when compared to the CO_2 and aerial dust.

Argon (Ar) in the atmosphere of Mars makes another noticeable cycle [*Sprague et al.*, 2004]. Phase change of CO_2 modifies the local mass mixing ratio of Ar (and other non-condensable gases). Further atmospheric convection and diffusion mix the gases and redistribute them around the planet. The entire non-condensable gas group can be considered as a passive tracer assuming that they are well mixed within themselves. It is another indicator of the Martian general circulation.

1.2 CO_2 phase change on Mars

Under certain conditions, usually extremely cold, the major constituent of the Martian atmosphere, CO_2, starts to condense out from the atmosphere and become dry ice. In other environments, usually warm, dry ice sublimates and becomes CO_2 gas. There are two major components of CO_2 phase change on Mars: 1. direct deposition/sublimation to/from the surface frost (exchange with surface reservoir); 2. atmospheric condensation/evaporation (exchange with "snow", which will either precipitate to the ground and become a part of the surface reservoir, or evaporate therefore rejoin the atmosphere before it reaches the surface).

The first component dominates the mass exchange. It is historically simulated by a surface energy balance model (described in Chapter 2). Such model has been proved to be a very simple but efficient way to capture the majority of the annual atmospheric behavior correctly, including matching the surface pressure records from the Viking Landers (VLs) [*Forget et al.*, 1999; *Leighton and Murray*, 1966; *Wood and Paige*, 1992], which is a good indication of the total atmosphere abundance. The energy balance is among the incoming solar radiation, the surface emission, the latent heat exchange during CO_2 phase change, sensible heat of the atmosphere, and the subsurface heat conduction. Each segment contributes to the energy balance in a significant way that more precise characterizations of these segments are constantly being demanded. As a result, much labor in this dissertation has been devoted to improve the modeling methods and parameterizations in a Mars General Circulation Model (GCM[4]), the Mars application of the planetary Weather Research and Forecast (MarsWRF) model, accompanied by experiments with different segments trying to explain the associated myths that have not yet been solved.

The second component can also be treated as a simple energy balance in the atmosphere. However, it is widely accepted that sophisticated microphysics models may be required for more accurate simulations, especially for modeling snowing events, convective available potential energy, radiative effects, and surface processes [*Colaprete and Toon*, 2002; *Colaprete et al.*, 2005; *Colaprete et al.*, 2008; *Forget et al.*, 1998]. Building on the foundation of previous researchers, I have coupled a complete microphysics model [*Wood*,

[4] GCM usually refers to earth GCM. In this dissertation, unless specifically specified, GCM (sometimes MGCM) is used to denote Mars GCM.

1999], which calculates the nucleation process and the ice particle growth process, to MarsWRF.

When the mass exchange between CO_2 solid and gas is determined, the mass mixing ratio change of the non-condensable gas can simply be determined by mass conservation. I implemented such treatment after finishing the phase transit calculations in corresponding physics subroutines in MarsWRF. The mass mixing ratio field of CO_2 is then fed to the internal convection and diffusion schemes of the dynamic core as a tracer.

1.3 Dissertation overview

Chapter 2 provides the description of the models that are used in the dissertation, including the GCM (MarsWRF), the energy balance model, the non-condensable gas exchange model, and the microphysics model that simulates the CO_2 cloud formation. I also provide an overview of how they coupled to each other in MarsWRF.

In **Chapter 3**, I fine tune MarsWRF by changing the values of the seasonal ice caps' albedos and emissivities and the total CO_2 mass in the system. The resulting pressure cycle, which is a good indicator of the atmospheric reservoir of CO_2 in the system, matches the *in situ* measurements by the VLs extremely well. This is the best fit for the surface pressure cycle by a GCM so far in the published literature. The fitting algorithm can be utilized to future GCM tuning and can be considered as a roadmap to unveiling relevant physics. For example, it is later extended to explore the effects of subsurface water ice.

In **Chapter 4**, I incorporate a linear relationship between the surface CO_2 frost albedo and the incident solar insolation (which is supported by observations) to MarsWRF. I then show how this insolation-dependent albedo leads to perennial CO_2 ice on the ground of Mars. Experiments with various orbital parameters and surface boundary conditions are presented to show their contribution to permanent CO_2 frost. This study may potentially shed some light on the lifetime and the cycles of the perennial CO_2 ice cap.

Chapter 5 presents the modeling effort for the non-condensable gas cycle and comparison with the Gamma Ray Spectrometer data and other GCMs. This is an independent check for the CO_2 cycle and a diagnostic for the atmospheric dynamics in the GCM. The results suggest that the GCMs may be excessively diffusive for tracer transportation, especially in southern winter near the south polar regions.

Chapter 6 describes the microphysics model for CO_2 cloud formation and how I integrate it to MarsWRF. Preliminary results from 1D and 3D simulations are shown and discussed.

The numerical simulations of this dissertation are performed on the Dell cluster (CITerra) in the Division of Geological and Planetary sciences, California Institute of Technology.

Chapter 2: Numerical models

Modeling works represent the state-of-the-art physical knowledge of human being. For phenomena that are too difficult to observe with existing instruments, too expensive to reconstruct in laboratories, or too time-consuming to record in one's lifetime, people especially have to rely on theoretical models. Recent advances in modern computational techniques make complicated and intensive numerical simulations feasible. The creation of General Circulation Models (GCMs) specifically allows human being to start exploring long term global change of climate. On the other hand, before any conclusion is drawn from the model results, thorough understanding of the physical models is crucial, especially in defining the achievable scientific goals. In this chapter, I present a brief introduction to the models that I have been using for my thesis. Major components of the model and their interactions are discussed. It provides an overview to the readers who are less familiar with the Mars atmosphere models. It also sketches the advantages and limits of the different segments of the simulation.

2.1 MarsWRF

For atmospheric science and climate research, GCM is arguably one of the most useful tools. It provides long-term climatology results (such as temperature, pressure, humidity, wind field, etc.) with complete coverage of the atmosphere, the surface, and the subsurface. For my thesis research, I used a Mars GCM, MarsWRF, which is the Mars

application of the planetary Weather Research and Forecast (WRF) model [*Richardson et al.*, 2007]. The WRF model was originally a mesoscale model developed by the National Center for Atmospheric Research (NCAR) and was later modified by Professor Mark Richardson's research group to be a global model. On top of the robust dynamic core provided by NCAR, the model provides complete and convenient physics modules (or subroutines) and interfaces, including radiative transfer, microphysics, tracer advection, subsurface physics, etc. It can be configured to perform 1D (in vertical direction), 2D (on horizontal plane), and 3D simulations, as well as mescoscale experiments. Other superb features include the "rotated pole" calculation, which redefine the projection of the model space to reduce numerical errors in the polar region, and nesting calculation, which allows a "zoom in" to smaller scale features.

A typical 3D setup of MarsWRF contains a grid structure yielding 36 × 64 × 40 (latitude, longitude, vertical) points. This setting provides a global coverage of Mars with the top of the model reaching up to 0.006 Pa, or about 80 km above the surface. Its horizontal resolution is 5.0 degree of latitude by 5.6 degree of longitude. Broad band radiative calculation covers visible and infrared spectral region with climatology aerial dust background. Boundary conditions, including topography, surface albedo, thermal inertia, terrain slope and slope orientation, are taken from spacecraft measurements. The temperature at the lower boundary of the subsurface layer is obtained from previous long-term simulations and stays fixed. Therefore, the subsurface reaches thermal equilibrium in a relatively short period of time (usually less than 100° of Ls). Nevertheless, data starting at the second year (after 360° of Ls) is typically used for the analysis in this dissertation.

2.1.1 Energy balance model for CO_2 phase change

Energy balance models are usually utilized to resolve the CO_2 annual cycle. The instantaneous surface energy balance equation when CO_2 frost exists on the surface is

$$S\,(1 - a)\,cos(i) - \varepsilon\sigma T^4 + k\,dT/dz + L\,dm/dt + H = 0, \qquad (2.1)$$

where S is the incoming solar flux at the current Mars-Sun distance; a is the albedo, either that of bare soil or frost; i is the solar incidence angle; ε is the surface emissivity, either that of bare soil or frost; σ is the Stefan-Boltzmann constant for black body emission; T is the surface temperature, either that of bare soil or fixed to the frost temperature when the surface is covered by CO_2 ice; k is the thermal conductivity of the soil; dT/dz is the vertical temperature gradient at the surface with z positive downwards (therefore, $k\,dT/dz$ is the upward conductive heat flux at the surface); L is the latent heat of CO_2 phase transfer between gas and solid; dm/dt is the CO_2 frost deposition/sublimation rate; H represents the sensible heat contribution induced by the atmosphere. The thermal conductivity of a material is related to its thermal inertia (I) by the equation $I^2 = k\rho c$, where ρ is the density and c is the heat capacity [*Wood and Paige*, 1992]. The product of ρ and c is assumed to be 1.26×10^6 J kg m^{-6} K^{-1} for the soil in MarsWRF. The atmospheric sensible heat (H) is usually smaller than the rest of the component in Equation 2.1 and earlier model even ignores this term completely (e.g. *Leighton and Murray* [1966] and *Wood and Paige* [1992]). However, it represents the advantage of the GCM compared to simpler models.

At any given time and location, when the radiative and sensible heating terms are negative, latent heating is required to balance the cooling and maintain the temperature at the frost point (the temperature remains at the condensation point because any infinitesimal

temperature drop would yield a drop in the required saturation vapor pressure. The difference between the actual surface pressure and the infinitesimally lower saturation vapor pressure would drive CO_2 from the atmosphere onto the surface, liberating latent heat that would tend to bring the temperature back up to the point where the atmospheric pressure and the saturation vapor pressure again agree). As a result, negative net radiative and sensible heating yields CO_2 gas conversion to ice and deposition on the surface. When net heating is positive and CO_2 ice is present on the surface, some amount of CO_2 frost becomes gas until the surface is exhausted of all its CO_2 ice cover. These phase exchange processes are usually assumed to be instantaneous in GCMs.

Similar model can be applied to the atmospheric condensation process. We write

$$dm_N = C_p M_N (T_{cN} - T_N) / L, \tag{2.2}$$

where C_p is the specific heat of the Mars atmosphere, M_N is the atmospheric mass of the N-th layer, T_N is the model projected temperature of the layer, T_{cN} is the critical temperature of the layer. dm_N amount of atmosphere is transferred to CO_2 ice and put to the ground instantaneously, and the temperature of this layer is reset to T_{cN}. Note this model assumes zero initial atmospheric CO_2 ice, therefore is only active when T_N is lower than T_{cN}, i.e., it only calculates condensation but not evaporation. Similar treatment has been used in previous literatures, such as *Forget et al.* [1998], *Pollack et al.* [1990], and *Wilson and Hamilton* [1996].

2.1.2 Subsurface heat conduction

The third term in Equation 2.1 describes the upward conductive heat flux at the surface. Within the soil, the one-dimensional heat conduction equation

$$dT/dt = k\,(\rho c)^{-1}\,d^2T/dz^2 \tag{2.3}$$

is solved numerically [*Wood and Paige*, 1992]. For a homogenous conductor, finite element differentiation for such second order derivative is standard. At some other situations, however, an inhomogeneous conductor is sometimes required. More attention is needed at the transition layer when numerically solving Equation 2.3. This equation can be rewritten as:

$$dT/dt = (\rho c)^{-1}\,dF/dz, \tag{2.4}$$

where $F = k\,dT/dz$ is the local heat flux. The finite differentiation therefore should treat the flux, which contains inhomogeneous heat conductivity at different grids, as the differentiable quantity.

2.1.3 Non-condensable gas concentration adjustment

We group all non-condensable gases together as a tracer. Its mass mixing ratio (q_{tra}) is:

$$q_{tra} = 1 - q_{vCO2}, \tag{2.5}$$

where q_{vCO2} is the mass mixing ratio of CO_2 vapor. This is simply a mass conservation of the tracers and the CO_2 vapor. When there is CO_2 phase change, the mass mixing ratios of CO_2 vapor is adjusted accordingly (to be described shortly). Assuming a constant mixing ratio of Ar (q_{Ar}) within the non-condensable tracers, we have

$$q_{\mathrm{Ar}} = c\, q_{\mathrm{tra}}, \tag{2.6}$$

where c is the mass fraction of Ar in the entire non-condensable gases. We set c = 0.458 assuming the non-condensable gases are dominated by N_2 and Ar [*De Pater and Lissauer*, 2001]. Thus we can always calculate the mass mixing ratio of Ar as long as we know the mass mixing ratio of CO_2, which is carried as a tracer in MarsWRF.

When CO_2 condenses to the ground, we calculate the amount of CO_2 gas dm that needs to be converted to ice:

$$dm = dm_{\mathrm{s}} + \sum dm_{\mathrm{N}} \; (\mathrm{N} = 1, 2, \ldots 40), \tag{2.7}$$

where dm_s is the direct surface condensation provided by solving Euqation 2.1. q_{tra} is then adjusted accordingly in the surface layer. If this amount (dm) is larger than the amount of CO_2 available in the lowest layer ($m_1 = q_{\mathrm{vCO2,1}} \times M_1$, $q_{\mathrm{vCO2,1}}$ being the mass mixing ratio of CO_2 vapor in layer 1, M_1 being the atmospheric mass of layer 1), we set the mass mixing ratio of CO_2 in the lowest layer ($q_{\mathrm{vCO2,1}}$) to zero and remove dm' of CO_2 in the layer above where

$$dm' = dm - m_1 = dm - q_{\mathrm{vCO2,1}}\, M_1. \tag{2.8}$$

q_{vCO2} is changed accordingly in the layer above. This adjustment keeps going upwards recursively if the next layer does not contain enough CO_2 to match dm'. When there is sublimation, the reverse adjustment of q_{tra} is only performed for the lowest layer of the atmosphere. This algorithm guarantees column mass conservation for both CO_2 and the

tracers while holding σ values[5] constant. It also ensures the mass mixing ratio profile of Ar to be a function decreasing with height, which was not achieved by *Nelli et al.*, [2007]. The tracer field is then coupled to the atmospheric advection and molecular diffusion in MarsWRF.

2.1.4 Microphysics model for CO_2 cloud formation

I developed a microphysics module for CO_2 cloud formation and incorporated it in MarsWRF. There are two sequential parts of this microphysics model: a nucleation model and a particle growth model [*Wood*, 1999]. The nucleation model calculates the number density of nuclei in 15 size bins depending on the ambient environment, including the super saturation ratio of the condensing gas, the potential number density of potential nuclei, and the size of the nucleus assuming they are spherical. Two kinds of possible nucleation mechanisms are considered: homogeneous nucleation, which does not require a core to nucleate to, and heterogeneous nucleation, which requires a nucleating core. At a given time step, the mechanism yielding higher nucleation rate is assumed. Knowing the number density distribution of the nuclei, the iterative growth model predicts the growth rates of ice particles of different sizes. Atmospheric temperature and mass are adjusted based on the latent heat and mass exchange. Details of this microphysics driver are provided in Chapter 6.

Heterogeneous nucleation usually generate larger nucleation rate with relatively low super saturation ratio [*Maattanen et al.*, 2005]. Martian aerial dust is a perfect candidate for

[5] σ coordinate system is commonly used in GCMs. σ value is defined by the pressure at any given model grid divided by the surface pressure. Therefore at the surface, the σ value is 1 while 0 at the top of the model. A series of σ value is usually prescribed for a GCM; the *in situ* pressure can be derived from the surface pressure.

the nucleation core. Ideally, the nucleation model should be coupled with the dust cycle in the GCM. Such coupling is very complicated and will significantly slow down the model. I made some simple assumptions about the distribution of the potential nuclei. A fixed background of dust weight density is prescribed. I assume the size distribution of the dust particles is log-normal, with an average size of 2 micron [*Newman et al.*, 2002a; b]. I also assume there is no replenishing source for this background dust species.

2.2 The full GCM

A schematic map, Figure 2.1, is provided to show how the different segments couple to each other in MarsWRF. This figure is reproduced and updated after Figure 1.1 of *Wood* [1999]. For the Mars GCMs, solar power, atmospheric dynamics, radiative transfer, surface and subsurface physics, and CO_2 physics are the most fundamental and necessary parts. As discussed before, the CO_2 physics has close interactions with the energy exchange of the atmosphere, the tracer transport, the aerosol distribution, and the radiative effects. Indeed, my dissertation focuses on the CO_2 physics and its interaction with other parts of MarsWRF.

Nothing more needs to be said about the complexity of the GCMs. Many of the aspects were heavily simplified, sometimes with naïve parameterizations and sometimes with less or zero verified assumptions. In principle, preciseness of each segment is attainable with careful tuning, comparison with observations, and eventually data assimilation. Indeed, much effort is currently being devoted to polish the GCMs. While the details of different GCMs may differ, or should them have different advantages and weakness, the ability of predicting long term climatology is the most essential.

As noted earlier, this chart may not be the complete view of an idealized GCM that "solves" the planet completely. More components relevant to the climate are currently being unveiled. The next chapter can be considered as a general roadmap for this unbundling process. As the human being's physical knowledge advances and the computation technology matures, GCMs will definitely improve in every aspect over the foreseeable future.

Figures

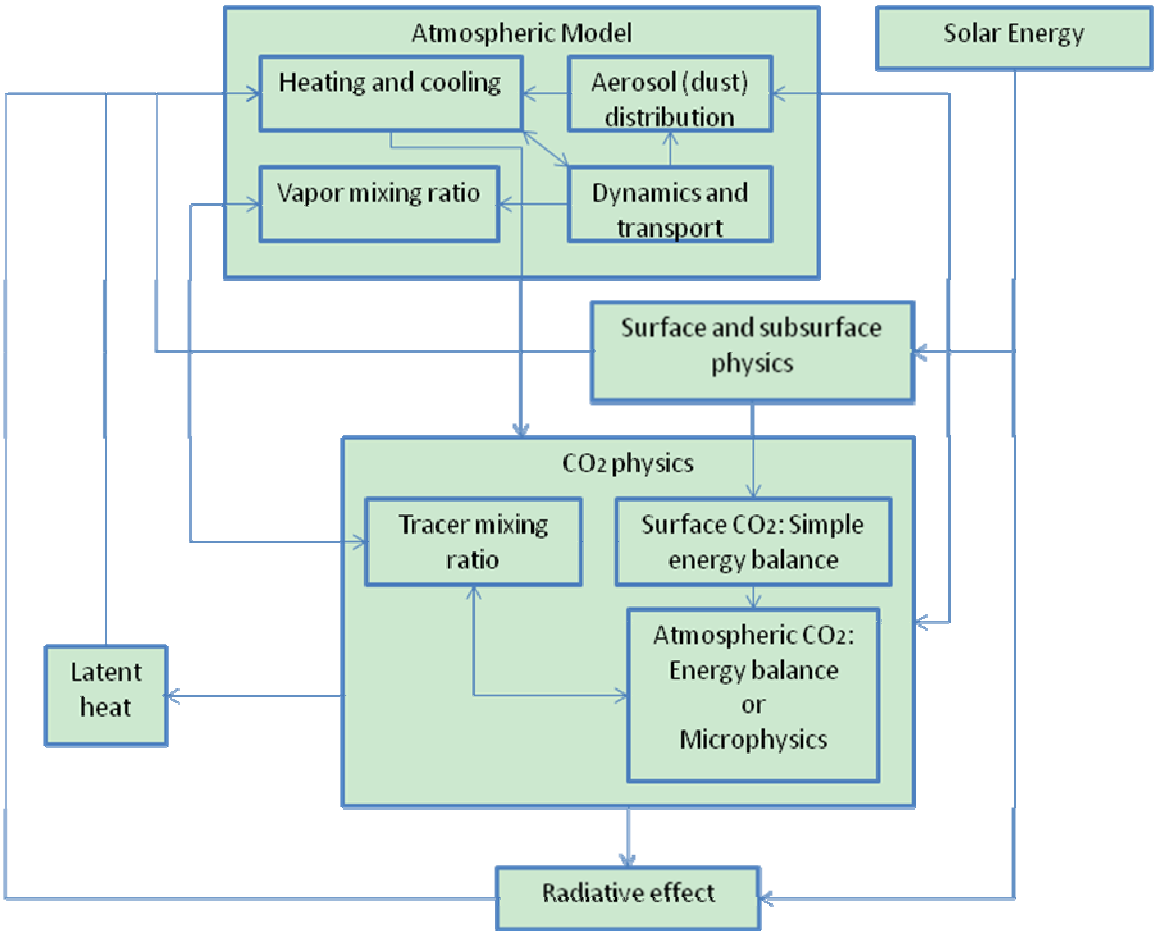

Figure 2.1: Schematic flowchart of MarsWRF.

Chapter 3: Modeling the Viking Lander pressure cycles

Abstract

We present a systematic attempt to fit the Viking Lander surface pressure cycle using a Mars General Circulation Model, MarsWRF. High-precision fitting was achieved by tuning five time-independent parameters: the albedo and emissivity of the seasonal caps of the two hemispheres and the total CO_2 inventory in the atmosphere-frost system. We used a linear iterative method to derive the best-fit parameters: albedo of the northern cap = 0.795, emissivity of the northern cap = 0.485, albedo of the southern cap = 0.461, emissivity of the southern cap = 0.785 and total CO_2 mass = 2.83×10^{16} kg. If these parameters are used in MarsWRF, the smoothed surface pressure residual at the VL1 site is always smaller than several Pascal through a year. As in other similar studies, the best-fit parameters do not match well with the current estimation of the seasonal cap radiative properties, suggesting that important physics contributing to the energy balance not explicitly included in MarsWRF have been effectively aliased into the derived parameters. One such effect is likely the variation of thermal conductivity with depth in the regolith due to the presence of water ice. Including such a parameterization in the fitting process improves the reasonableness of the best-fit cap properties, mostly improving the emissivities. The conductivities required in the north to provide the best-fit are higher than those required in the south. A completely physically reasonable set of fit parameters could still not be attained. Like all prior published GCM simulations, none of the cases considered are capable of predicting a residual southern CO_2 cap.

3.1 Introduction

In every atmospheric General Circulation Model (GCM), one of the first and foremost issues to consider is the total mass of the atmosphere. Its value affects all subsequent calculations performed in the GCM, including dynamics, radiative transfer, tracer and energy transport, chemical reactions, etc. When a component of the atmosphere is volatile (changes state for commonly encountered environmental conditions), the surface pressure may be affected. For the Earth, where the abundance of water vapor is modestly high, many GCMs include the varying contribution of water vapor partial pressure when calculating the full surface pressure. For planets where their major atmospheric constituents condense (such as Mars, Triton, and Pluto), consideration of the role of phase change in varying the surface pressure is important.

Carbon dioxide (CO_2) is the leading gaseous species on Mars, comprising 95% of the atmosphere [*Owen et al.*, 1977]. Throughout a Martian year, up to 30% of the total CO_2 condenses onto the surface in winter polar regions [*Kelly et al.*, 2006]. The condensation of CO_2 occurs because the Martian atmosphere is sufficiently thin that transport of sensible heat is unable to sustain the winter polar atmosphere. As a result, the temperatures fall until the frost point of CO_2 (also loosely referred to as "condensation point", although condensation usually refers to the phase change from gas to liquid) is reached, after which thermal infrared losses are buffered by latent heating.

The Viking Landers (VLs) provide the only inter-annual records of surface pressure on Mars. These records contain variability on several different time scales. Variations on timescales of seconds, hours, and days are associated with boundary layer turbulence,

thermal tides, and large-scale weather systems, for example. However, when the high frequency component is ignored, the surface pressure variation at a specific location on Mars (Figure 3.1) is largely determined by the bulk mass of atmosphere, though small contributions due to standing systems over long periods like the condensation flow and the inter-tropical lows and sub-tropical highs are also present. Therefore, to some significant degree of precision, the VL pressure records can be taken as topographically shifted records of the bulk atmospheric mass [*Hess et al.*, 1977]. Fitting the observed VL pressure cycle also establishes a baseline for climate studies, both short-term and long-term. As shown in Figure 3.1, the dominant long period signal is the very repetitive annual cycle that can be identified with the atmosphere freezing out to form the seasonal polar caps, followed by the caps' decay due to sublimation back to the atmosphere [*Hourdin et al.*, 1993]. Models are often tuned to match this annual cycle, though small errors in amplitude and (especially) phase are often tolerated, depending on the interests of a particular study [*Forget et al.*, 1998; *Haberle et al.*, 2008; *Hourdin et al.*, 1993; *Pollack et al.*, 1993; *Richardson and Wilson*, 2002a]. Indeed, the quality of fits in GCMs is in some sense surprisingly poor. For a system that should be driven primarily by radiative, latent, and thermal conductive heating processes at the caps, it would seem that a near perfect fit should be attainable. An accurate simulation of the pressure cycle would also be desirable for many applications where good prediction of the surface pressure is needed as a boundary condition, such as surface wind stress calculation, spacecraft entry-descent-landing analysis, etc. In reality, the main reason that ideal fits have not been attained is due to the computation involved: the problem reduces to one of searching for the best-fit parameters using a relatively large number of simulations (certainly "large" by standards prior to the early 2000's).

There are historical attempts to "fit" the CO_2 cycle. *Wood and Paige* [1992] proved that it is possible to fit the VL data to within several Pascal using a one-dimensional (1D) diurnal and seasonal thermal model without any explicit atmospheric contribution to the heat balance. The albedos and emissivities of the northern and southern seasonal CO_2 caps and total mass of CO_2 in the system were tuned and kept constant with time. In their 1D study, the residual between the modeled pressure in the best case scenario and the observed was as small as a few Pascal. However, their best-fit parameter values differ from the current estimates for the caps' radiative properties. If values from *Wood and Paige* [1992] are used in a GCM, the resulting pressure curves are not unreasonable, but the lack of an atmosphere and the use of constant thermal inertia translates to offsets that yields a GCM cycle notably worse than what the same parameters produces in the 1D model.

It is clear from 1D modeling that tuning of the cap properties will allow the modeled CO_2 cycle to be improved. It seems the standard for Mars GCMs is to accomplish this tuning "by-eye". However, the resulting parameters are not physical compared with spacecraft observations. For example, the cap albedos have to differ dramatically between the poles, with the northern values required to be much higher than observed [*Haberle et al.*, 2008; *Kieffer et al.*, 2000; *Kieffer and Titus*, 2001]. One possible way to improve the reasonableness of the parameters is to include other effects, such as the thermal conductivity induced by subsurface water ice [*Haberle et al.*, 2008]. However, to date there has not been an attempt to systematically determine the cap properties needed in a GCM to produce a seasonal pressure cycle within the VL instrument error. Here, we present a recipe that can be used to calibrate a GCM pressure cycle, and we provide some discussion of what areas of uncertainty still remain in the understanding of the CO_2 cycle on Mars.

In this chapter, we describe the development and execution of a benchmark study for reproducing the observed surface pressure cycle in a Mars GCM. We specifically use the Martian implementation of the planetWRF model [*Richardson et al.*, 2007]. The reason that *Wood and Paige* [1992] were able to generate excellent fits of the VL pressure cycle is that their 1D model is simple and computationally cheap: hundreds of runs were made to cover the parameter space so that a best fit can be identified. Hundreds of runs for any sophisticated GCM is generally not feasible in a reasonable amount of time, nor are such runs necessary with our proposed method. Our technique involves the creation of an ensemble of simulations that are used to understand how the model's representation of the VL surface pressure cycles responds to perturbations of different parameters. Knowing these relationships, we use an iterative linear method to find the best set of parameters to fit the VL data. The method can fit the VL data with a very high degree of accuracy — comparable to, if not better than, the fit using the simpler 1D model [*Wood and Paige*, 1992]. This approach is non-model specific and is suggested as an efficient means of finding the parameters for a best-fit pressure cycle for any GCM. After demonstrating the method for the set of parameters chosen by *Wood and Paige* [1992], we proceed further to study how changes in soil thermal properties due to subsurface water ice affect the model's representation of the VL surface pressure record.

The fact that *Wood and Paige* [1992] were able to fit the pressure cycle using a simple model has profound meaning. It suggests that the physics included in the model, namely the surface heat balance at the poles, is the controlling physics for modeling the CO_2 and pressure cycles. The non-physicality of the cap parameters retrieved from the *Wood and Paige* [1992] scheme does not invalidate the approach – instead it demonstrates that there

exists a range of processes that affect the polar energy balance that are not incorporated ("resolved") in the model and hence their effects are "aliased" (or "bundled") into the estimated best fit parameters — for example, an unrealistically high albedo value may effectively compensate for model missing clouds. Further progress in understanding the CO_2 cycle, which is tantamount to understanding the polar energy balance, is now a question of unbundling the various processes that are aliased into the retrieved parameters. The way this can be done is by applying models with more complete sets of explicit physics. Applying the same fitting routines within a hierarchy of increasingly complex models will allow the progressive unbundling of important physics affecting the polar heat balance. Where will it all end? At some point a set of physically plausible radiative parameters (potentially in the form of time and spatially varying parameters defined by a physical understanding of the ice microphysics and formation history) will signal the completion of the unbundling process. For example, in this study, we apply a GCM to the problem studied in 1D by *Wood and Paige* [1992]. Explicit treatment of atmospheric dynamics, spatially varying topography, regolith albedo, and thermal propertie of soils can thus be unbundled from the parameters found by *Wood and Paige* [1992]. The complexity of implementing this task arrives from the very large number of runs required to find excellent data fits. Such a brute-force method is not available when running computationally expensive GCM simulations. Hence, much of our discussion in this chapter is in the demonstration of a method to allow data fitting with a relatively small number of runs. In principle, modified versions of this approach can be applied to fit various other data sets (e.g., temperature). In essence, it is a limited implementation of a prototype form of data assimilation (here we are pursing "parameter estimation" while most data assimilation attempts "state estimation"). Obviously, an ideal

approach would be to simultaneously fit the surface pressure data along with records of air temperature, dust, water ice, etc. This in fact would require a full parameter-and-state data assimilation system, which is a future goal of our research. That notwithstanding, the approach and schemes presented here allow some new insight into the CO_2 cycle without having to resort to a full data assimilation system.

In section 3.2, we discuss the relevant physical processes contributing to surface energy balance, and we present the initial sensitivity study for several important contributing parameters. In section 3.3, we introduce the iterative linear fitting method. We show the fitting results in section 3.4. Physical interpretation of the best-fit parameters is discussed in section 3.5. Section 3.6 concludes this chapter.

3.2 Surface energy balance and sensitivity study

3.2.1 Surface energy balance

The key physics for the Martian annual CO_2 cycle is the surface energy balance. The instantaneous surface energy balance equation when CO_2 frost exists on the surface is:

$$S\,(1-a)\,cos(i) - \varepsilon\sigma T^4 + k\,dT/dz + L\,dm/dt + H = 0, \qquad (3.1)$$

where S is the incoming solar flux at the current Mars-Sun distance; a is the albedo, either that of bare soil or frost; i is the solar incidence angle; ε is the surface emissivity, either that of bare soil or frost; σ is the Stefan-Boltzmann constant for black body emission; T is the surface temperature, either that of bare soil or the frost temperature when frost presents; k is the thermal conductivity of the soil; dT/dz is the vertical temperature gradient at the surface

with z positive downwards (therefore, $k\ dT/dz$ is the upward conductive heat flux at the surface); L is the latent heat of CO_2 frost; dm/dt is the CO_2 frost deposition/sublimation rate; H represents the sensible heat contribution induced by the atmosphere. The thermal conductivity of a material is related to its thermal inertia (I) by the equation $I^2 = k\rho c$, where ρ is the density and c is the heat capacity [*Wood and Paige*, 1992]. The product of ρ and c is assumed to be 1.26×10^6 J kg m^{-6} K^{-1} for the soil in MarsWRF. This is a simplified view of the problem. The GCM contains additional terms associated with the atmospheric components that contribute to this energy balance, which are usually much smaller when compared to the rest. Thus for simplicity without losing clarity to the readers, we will refer to this equation, which captures the majority of the physics.

At any given time and location, when the radiative and sensible heating terms in Equation 3.1 are negative, latent heating is required to balance the cooling and maintain the temperature at the condensation point (the temperature remains at the condensation point because any infinitesimal temperature drop would yield a drop in the required saturation vapor pressure. The difference between the actual surface pressure and the infinitesimally lower saturation vapor pressure would drive CO_2 from the atmosphere onto the surface, liberating latent heat that would tend to bring the temperature back up to the point where the atmospheric pressure and the saturation vapor pressure again agree). As a result, negative net radiative and sensible heating yields CO_2 gas conversion to ice and deposition on the surface. When net heating is positive and CO_2 ice is present on the surface, some amount of CO_2 frost becomes gas until the surface is exhausted of all its CO_2 ice cover. These phase exchange processes are usually assumed to be instantaneous in GCMs.

Extensive work has been done examining water ice cloud and CO_2 ice cloud formation. Modeling studies found evidence showing their importance in the polar energy budget by influencing the surface properties, temperature, and dynamics [*Colaprete et al.*, 2005; *Colaprete et al.*, 2008; *Richardson et al.*, 2002]. Because the microphysics modeling of clouds in the Martian atmosphere is a subject under investigation, we do not include CO_2 cloud formation or a water cycle in this study (these processes will await further unbundling at a future date).

In selecting parameters to use for the fitting of the CO_2 cycle, we take into account what variables are going to have a major effect on the polar energy balance and also what aspects of the model are relatively well constrained. For the radiative transfer, we use our standard solar and thermal infrared radiative heating schemes and also chose to prescribe the dust opacity distribution with the Mars Climate Database "MGS" scenario parameterization. Global soil albedo, emissivity and surface thermal inertia are used as derived from spacecraft observations [*Richardson et al.*, 2007]. The parameters chosen to vary for the simulation are those associated with the seasonal caps and the bulk inventory of CO_2: the albedo and the emissivity of the seasonal CO_2 ice caps (potentially separate values for each pole), the global CO_2 mass (both gaseous and solid phase), and the thermal inertia of the polar regolith, which is a mixture of soil and water ice. All the parameters are crucial to the energy balance and the pressure cycle. In the sections following, we first discuss the conventional tuning parameters, namely albedo, emissivity, and total CO_2 inventory. Then we discuss the less-studied varying thermal property of the subsurface.

3.2.2 The usual suspects: albedo, emissivity, and total CO_2 inventory

The albedo determines the fraction of incoming solar energy reflected back to space. In general, increasing the albedo decreases the absorbed energy available to the land-air system. In the Martian polar winter, as temperatures drop to the CO_2 frost point and CO_2 deposits on the surface, the high (bright) ice albedo further lowers solar heating, and more CO_2 freezes out. The magnitude of this feedback effect depends on the value of the frost albedo. Thus, surface pressure tends to lower as a result of an increased CO_2 cap albedo, and vice versa. We note that this effect is only relevant when CO_2 frost is present and it is receiving insolation (an example of this is shown in panel (a) of Figure 3.3, discuss later).

The emissivity of the seasonal caps participates in maintaining surface energy balance differently than albedo does. The larger the emissivity of a CO_2 frost cap, the more energy it releases to space. Thus a larger emissivity yields a larger energy deficit, which in turn requires more condensation of CO_2 to release latent heat and compensate for the energy deficit. The net effect is that an increase in emissivity leads to a decrease in the surface pressure. Similarly to albedo's effect, we note that the effect of emissivity on surface pressure is only relevant when CO_2 frost is present, though it can operate throughout polar night (this is also present in panel (a) of Figure 3.3, discuss later). This means that the effects from albedo changes and from emissivity changes have different longevity and prominence: while albedo only acts when the seasonal caps are exposed to the sun, emissivity acts as long as the surface frost exists. Therefore, the albedo "footprint" (the effect on the surface pressure cycle due to variations of albedo) for a given pole is non-zero only later in its season of frost coverage, whereas the emissivity footprint is present throughout the frost coverage season.

The total mass of CO_2 in the system influences the surface pressure cycle in a very linear manner. Since none of the terms in Equation 3.1 is very sensitive to total atmospheric mass, the surface frost amount changes very little when total mass of CO_2 is changed (this is also present in panel (a) of Figure 3.3, discuss later). Of course, one should not make very large perturbations to the CO_2 inventory lest the planet migrates to another climate regime [*Mischna et al.*, 2000]. It should also be noted that since the model does not predict the development of a residual CO_2 ice cap (nor does any published GCM), increasing the surface pressure is possible by increasing the total CO_2 inventory.

3.2.3 Water ice in the subsurface layer

In Equation 3.1, the vertical heat flux is determined by the temperature gradient near the surface and the soil's thermal conductivity. Subsurface thermal structure is determined by the energy input from the surface and the thermal property underneath. Typically, the subsurface thermal conductivity is assumed to be the same as that of the surface. It has recently been suggested that the subsurface water ice would affect the exchange of CO_2 between the atmosphere and the seasonal caps greatly [*Haberle et al.*, 2008]. The presence of water ice increases the thermal conductivity of the soil. In the summer, when the surface is not covered by frost, more heat conducts downward compared to the situation where homogenous dry soil is assumed. When this extra amount of heat is released in the winter, surface CO_2 ice formation is reduced, and surface pressure increases accordingly. Changing the thermal inertia (equivalent to the thermal conductivity) of the regolith changes the thermal structure and heat flux of the soil. Eventually, it changes the surface pressure cycle.

In order to investigate how subsurface water ice affects the CO_2 cycle, we modified the subsurface model in the MarsWRF to handle vertical gradients of soil thermal conductivity. At depth where water ice becomes stable and has significant mass, we increase the thermal conductivity of the soil. This is similar to the two layer model used by *Haberle et al.* [2008], in which the regolith beneath a certain depth (8.05 cm for the northern hemisphere and 11.16 cm for the southern hemisphere) was fully filled by a water ice table from 55° to 90° latitude (Figure 3.2, panel (b)); however, we do not use fixed depths across the two hemispheres.

In order to parameterize the three-dimensional distribution of water ice in the subsurface, we include the water ice content map provided by the Mars Odyssey Gamma Ray Spectrometer (GRS) [*Boynton et al.*, 2002; *Feldman et al.*, 2002; *Feldman et al.*, 2004] and the depth of the permanently stable subsurface water ice predicted by *Schorghofer and Ahronson* [2005] to MarsWRF (Figure 3.2). Water ice is only seasonally stable at mid-latitudes [*Schorghofer and Aharonson*, 2005], and the available water vapor in the atmosphere does not seem to be enough to fill meters of regolith [*Smith*, 2002]. Therefore, we set the water ice table depth to be the cutoff line of the permanently stable water ice, which changes with latitude and longitude.

The other parameter to decide upon is the thermal conductivity, or equivalently the thermal inertia, of the soil mixed with water ice (hereafter, we loosely call it a water ice table even though it is not pure water ice). Viking Infrared Thermal Mapper (IRTM) observations show that the apparent thermal inertia of the dry Martian surface ranges from 46 to 630 J m^{-3} K^{-1} , with a global average of 275 J m^{-3} K^{-1} [*Paige*, 1992]. This agrees with observations from the Thermal Emission Spectrometer (TES) on board of the Mars Global Surveyor

(MGS) [*Putzig et al.*, 2005]. Pure water ice has a thermal inertia of 2200 J m^{-3} K^{-1}. Assuming a mixture has 80% of water ice, the thermal inertia of the mixture can range from 100 to 1200 J m^{-3} K^{-1}, depending on the thermal inertia of the host regolith. These numbers provide physical constraints for the fitting parameters in later sections. We do not assume the water content provided by GRS for the water ice table because that data set is not vertically well resolved. The water information from GRS is only used for the geographical distribution. We set the threshold for water content to 9% in order to cover the latitudes of 55° and poleward.

Of course, we do not have to limit ourselves to these numbers in the sensitivity study. We find that the VL pressure cycle is very sensitive to the thermal inertia assumed for the water ice table (panel (b) of Figure 3.3). A change in the assumed water ice table thermal inertia changes the VL pressure cycle significantly. As expected, larger thermal inertia leads to higher surface pressure. We find that the water ice table thermal inertia shows a very similar footprint to that of the emissivity: the increasing phase of their signals lasts from Ls 210° to 360° in the northern winter and from Ls 30° up to 180° in the southern winter; the decreasing phase of the thermal inertia signal ends shortly before that of the emissivity. However, we find that thermal inertia does not project a change on the surface pressure cycle as linearly as emissivity does. For example, doubling the thermal inertia perturbation does not necessarily double the resulting pressure change. In addition, changing the thermal inertia modifies the phase of the pressure signal. Also of note, the sensitivity to thermal inertia evidently saturates: when we extend the thermal inertia above some certain amount, the pressure cycle fails to respond. At that point, the soil in the model contains the maximum possible amount of heat it can. Fortunately for the prospect of fitting the pressure cycle, with the current depth of soil, MarsWRF seems to reach that extreme for a thermal inertia value

larger than 5000 J m^{-3} K^{-1}, which is much larger than most of the possible material in the regolith including pure water ice. Nonetheless, we need to be careful when we perform the linear retrieval later, where we assume the pressure cycle always responses linearly to all the perturbations.

The average thermal inertia of dry Martian soil has an annual skin depth around 1 meter, which is usually deeper than the stable water ice depth. Our subsurface model in MarsWRF covers more than 7 meters, deeper than the annual skin depth of pure water ice (thermal inertia of 2200 J m^{-3} K^{-1}, skin depth 5 meters). The stable water ice depth was calculated assuming the soil porosity being about 70%. The pressure cycle is not very sensitive to the assumption of the underlying soil porosity. This is because the stable ice depth does not change much with soil porosity near the poles, where the low temperature allows subsurface water ice to preserve easily.

3.2.4 Mathematical representation

In order to simplify the discussion and the description of the linear fitting method, we introduce the following mathematical notation. In the initial experiments, five parameters in MarsWRF are tuned: the albedo and emissivity of the seasonal CO_2 caps for both the north and south poles, and the total mass of CO_2 in the system. The linear methodology discussed in section 3.3 relies on making relatively small corrections; hence we constructed a baseline case with parameters similar to those used in *Wood and Paige* [1992]. The northern cap albedo is set to 0.770, northern cap emissivity to 0.570, southern cap albedo to 0.500, southern cap emissivity to 0.800 and total CO_2 mass to 2.90×10^{16} kg of CO_2 (we use an

index number 1.00 hereafter to represent this reference total CO_2 amount). We denote the parameter vector as $\boldsymbol{A}$, a column vector whose rows contain the parameters used in an experiment in the order just mentioned. For the baseline case, we write:

$$\boldsymbol{A}_0 = [0.770\ 0.570\ 0.500\ 0.800\ 1.00]^{\mathrm{T}}, \tag{3.2}$$

where superscript T denotes the vector transpose. The values in this parameter vector are used in MarsWRF to yield its corresponding baseline model atmosphere. After the model reaches a steady state (taken to be a Martian year - note that the initial subsurface temperature were taken from the results of a prior decadal simulation and were thus very nearly in balance from the outset), a Mars year of surface pressure output is diagnosed for its predicted values of the Viking Lander 1 (VL1) data record. This diagnosis requires interpolating within the output to find the surface pressure at the actual latitude, longitude, and elevation of the lander (grey line in Figure 3.1). It is evident that the model's predicted pressure cycle has larger short term variations in the second half of the year, and this is consistent with observations and previous GCM studies. Details of those short term variations are beyond the scope of this study. For the purpose of tuning the uncertain parameters in our vector, we are only interested in the long term trend. Hence we apply a 9-sol running averaging to the model output's predicted surface pressure record to remove the undesired high frequency components. This smoothed pressure cycle, $\boldsymbol{X}_0$, a column vector with 669 rows (each row represents a sol) is plotted in Figure 3.1 as the dashed magenta line. We write

$$\boldsymbol{X}_0 = I(W(\mathbf{A}_0)) \equiv F(\boldsymbol{A}_0), \tag{3.3}$$

where operator I denotes all the required interpolations and smoothing, and operator W denotes the MarsWRF model when run with the parameters included in $\boldsymbol{A}_0$. We can combine these two operators into one effective operator, F, that maps a given parameter vector to a predicted smoothed VL1 pressure record.

In order to sensibly compare our smoothed model predicted pressure cycle to the observations, which also exhibit high frequency variations due to tides and baroclinic weather systems, we have used a smoothed, continuous representation of the VL1 observations in non-dust storm conditions. Instead of applying the same 9-day running average as we have to the model output, we use the polynomial fit of the non-dust storm VL1 pressure curve [*Tillman et al.*, 1993]. Using a polynomial allows us to compare the model to the data in regions where there are gaps in the VL1 data record. The smoothed VL1 observations are presented by the dashed blue line in Figure 3.1, with one value of VL1 surface pressure per sol (669 values in a Martian year). We follow the same practice with the VL2 observation, shown in Figure 3.1 as the red dashed curve, though we do not use the VL2 observations within the linear fitting method.

As is evident in Figure 3.1, the smoothed pressure cycle generated using the baseline parameter set (magenta dashed line for VL1 and green dashed line for VL2) differs from the observations (blue dashed line for VL1 and red dashed line for VL2). The largest differences are in northern summer (or southern winter), where phase errors are evident. The residual, defined as the model predictions less the VL observations, vary from 0 to 20 Pa throughout most of the year, with an average of 8.2 Pa and a standard deviation of 7.0 Pa at the VL1 site. The root mean square (RMS) of the residual at the VL1 site is 10.8 Pa, or 1.2 to 1.6% of the seasonal cycle.

To estimate the sensitivities of MarsWRF to the parameters within $\boldsymbol{A}_0$, we make five additional MarsWRF model runs, one for each element in $\boldsymbol{A}_0$. Each run adds a small perturbation to the value of one parameter in $\boldsymbol{A}_0$ while keeping the other values unchanged. Once completed, we apply the same interpolation and averaging to obtain the five predicted smooth pressure cycles at the VL1 location associated with the five perturbed parameter vectors. We denote the perturbed parameter vectors as $\boldsymbol{A}_i$ (i = 1, 2, 3, 4, 5), and analogously to Equation 3.3, their resulting pressure records are $\boldsymbol{X}_i$ (i = 1, 2, 3, 4, 5). To be clear, the order of the perturbations associated with the i index follows the order of parameters within $\boldsymbol{A}_0$: northern seasonal cap albedo, northern cap emissivity, southern cap albedo, southern cap emissivity, and the index number of the total CO_2 mass in MarsWRF, respectively. We chose the following set of perturbed parameter vectors $\boldsymbol{A}_i$:

$$\boldsymbol{A}_1 = [0.820\ 0.570\ 0.500\ 0.800\ 1.00]^{\mathrm{T}}, \tag{3.4}$$

$$\boldsymbol{A}_2 = [0.770\ 0.670\ 0.500\ 0.800\ 1.00]^{\mathrm{T}}, \tag{3.5}$$

$$\boldsymbol{A}_3 = [0.770\ 0.570\ 0.600\ 0.800\ 1.00]^{\mathrm{T}}, \tag{3.6}$$

$$\boldsymbol{A}_4 = [0.770\ 0.570\ 0.500\ 0.900\ 1.00]^{\mathrm{T}}, \tag{3.7}$$

$$\boldsymbol{A}_5 = [0.770\ 0.570\ 0.500\ 0.800\ 1.06]^{\mathrm{T}}. \tag{3.8}$$

These vectors are related to the baseline parameter vector through

$$\boldsymbol{D}_i = \boldsymbol{A}_i - \boldsymbol{A}_0, \ (\ i = 1, 2, 3, 4, 5\ ). \tag{3.9}$$

Similarly, we define the perturbation pressure vectors

$$\boldsymbol{P}_i = \boldsymbol{X}_i - \boldsymbol{X}_0 = F\,(\boldsymbol{A}_i) - F\,(\boldsymbol{A}_0), \ (\ i = 1, 2, 3, 4, 5\ ). \tag{3.10}$$

While a matrix whose columns are the $\boldsymbol{D}_i$ vectors is a 5-by-5 diagonal matrix, a matrix whose columns are the $\boldsymbol{P}_i$ vectors is 669-by-5 and potentially has non-zero entries everywhere. The $\boldsymbol{P}_i$ vectors are shown in panel (a) of Figure 3.3, and one can see that they are in general non-zero, except for the vectors associated with perturbed albedo and emissivity when they are not contributing to the surface energy balance.

This same procedure for gauging the model's sensitivity to uncertain parameters can easily incorporate other components. Later in this study, we extend the parameter vector to include the water ice table thermal inertia. This requires defining a new baseline case with parameter vector

$$\boldsymbol{A}^e{}_0 = [0.770\ 0.570\ 0.500\ 0.800\ 1.00\ 1.20\ 1.20]^{\mathrm{T}}, \tag{3.11}$$

where the definitions of the first five elements of this vector are the same as before, and the sixth and seventh elements correspond to the thermal inertia of the subsurface layer in the northern polar region and the southern polar region, in units of 1000 J m^{-3} K^{-1}. We use the same notation for the operators that map a given parameter vector to a predicted smoothed pressure curve for VL1:

$$\boldsymbol{X}^e{}_0 = I(W(\boldsymbol{A}^e{}_0)) = F(\boldsymbol{A}^e{}_0). \tag{3.12}$$

To be clear, in the experiments where only the first five parameters are varied, MarsWRF still runs with assumed values for the sixth and seventh parameters. However, their values are not available for modifying to better fit the VL1 pressure data. When the parameters for subsurface thermal inertia in the two hemispheres are available for change, we specify two new parameter vectors:

$$\boldsymbol{A}^{e}_{6} = [0.770\ 0.570\ 0.500\ 0.800\ 1.00\ 1.50\ 1.20]^{T}, \quad (3.13)$$

$$\boldsymbol{A}^{e}_{7} = [0.770\ 0.570\ 0.500\ 0.800\ 1.00\ 1.20\ 1.50]^{T}. \quad (3.14)$$

These extended perturbed parameter vectors logically extend to the definitions of $\boldsymbol{D}^{e}_{6}$, $\boldsymbol{D}^{e}_{7}$, $\boldsymbol{P}^{e}_{6}$ and $\boldsymbol{P}^{e}_{7}$ via Equation 3.9 and 3.10. The corresponding perturbation pressure vectors for $\boldsymbol{P}^{e}_{6}$ and $\boldsymbol{P}^{e}_{7}$ are shown in panel (b) of Figure 3.3. This panel also shows one additional perturbation pressure vector ($\boldsymbol{P}^{e}_{extra}$) obtained from running MarsWRF with

$$\boldsymbol{A}^{e}_{extra} = [0.770\ 0.570\ 0.500\ 0.800\ 1.00\ 1.50\ 1.50]^{T}.$$

This is included to demonstrate that $\boldsymbol{P}^{e}_{extra}$ is roughly the sum of $\boldsymbol{P}^{e}_{6}$ and $\boldsymbol{P}^{e}_{7}$, thereby demonstrating these parameters behave fairly linearly. Note that $\boldsymbol{P}^{e}_{extra}$ is not used in the fitting method described in the next section.

3.3 Linear fitting methods

We chose to fit the pressure cycle at just one of the VL sites, reserving the other as an independent resource to check the retrieved set of parameters. Since the VL1 pressure record is much less susceptible to local weather disturbances and large global dust storms, and is more complete in turns of time coverage than the VL2 record, the VL1 data is taken to be the preferable target for model fitting, as was usually used in earlier studies [*Forget et al.*, 1998; *Wood and Paige*, 1992]. It should be noted, however, that the method we employ can easily include VL2 data simultaneously.

The Viking pressure transducers were calibrated to about 2 Pa [*Tillman*, 1988]. This 2 Pa instrument error is the only meaningful number that one can ascribe to "good enough" in

regards to fitting the observations. To fit better than 2 Pa could be unwarranted and to fit worse than 2 Pa betrays shortcomings in the model. Without some reference to a meaningful numerical value, all fits are more or less qualitative.

In order to fit the smoothed VL1 pressure cycle, we use a simple linear method to first construct a best-fit pressure curve from the baseline scenario plus a linear combination of the 5 perturbation pressure vectors $\boldsymbol{P}_i$. We then assume, as a consequence of linearity, the resulting best-fit MarsWRF parameters are equal to the baseline parameters plus the same linear combination of the perturbation parameter vectors, $\boldsymbol{D}_i$. If the linearity assumption holds, then we should find that nonlinearly validating the best-fit parameters (by running MarsWRF with those values and applying the interpolation and smoothing operators) yields a pressure cycle very similar to both the best-fit pressure curve found from the linear combination of $\boldsymbol{P}_i$, and the smoothed VL1 measurements.

To illustrate the assumptions and consequences of our linearity assumption, consider a vector of perturbations, $\delta\boldsymbol{A}$, to the baseline parameter vector. If the nonlinear operator F is applied to this perturbed parameter vector, then

$$\boldsymbol{X}_0 + \delta\boldsymbol{X} = F(\boldsymbol{A}_0 + \delta\boldsymbol{A}). \tag{3.15}$$

Performing a Taylor series expansion of the right hand side of Equation 3.15 about the baseline vector:

$$\boldsymbol{X}_0 + \delta\boldsymbol{X} = F(\boldsymbol{A}_0) + \mathbf{F}\delta\boldsymbol{A} + \mathrm{O}(\|\delta\boldsymbol{A}\|^2), \tag{3.16}$$

where $\mathbf{F}$ is the Jacobian matrix of partial derivatives of $F(\boldsymbol{A}_0)$ with respect to the elements in $\boldsymbol{A}$, evaluated about $\boldsymbol{A}_0$. Note that in our case $\mathbf{F}$ is a 669-by-5 matrix. If the vector of parameter

perturbations is small, where "small" is defined by the ratio of the vector norms of $\delta\boldsymbol{A}$ and $\boldsymbol{A}_0$ being less than 1, then one can safely neglect the higher order terms in Equation 3.16, represented by $O(||\delta\boldsymbol{A}||^2)$. Neglecting these terms and subtracting the relation in Equation 3.3 yields:

$$\delta\boldsymbol{X} = \mathbf{F}\delta\boldsymbol{A}, \tag{3.17}$$

which is a linear relationship between perturbations in parameters and their resulting perturbations in the pressure curve. An immediate consequence of this linear relationship is that a constant factor change in $\delta\boldsymbol{A}$ gives the same factor change in $\delta\boldsymbol{X}$.

The potential complexity of Equation 3.17 is contained within the matrix **F** (which itself is defined in Equation 3.3 and 3.16). While it is theoretically possible to evaluate the Jacobian matrices of MarsWRF (W) with respect to specific parameters (i.e., the derivative of the model variables with respect to the parameters) and also for the interpolation and smoothing operators (I) for MarsWRF output, it is a difficult feat requiring lots of code development. Instead of attempting to explicitly calculate **F**, we approximate it by way of our explicit introduction of small perturbations to the parameters within $\boldsymbol{A}_0$ (as described in the previous section). Hence, the columns of **F** are related to the perturbation pressure vectors and the magnitudes of parameter perturbations:

$$\boldsymbol{F}_i = \boldsymbol{P}_i / ||\boldsymbol{D}_i||, \ (\ i = 1, 2, 3, 4, 5\ ), \tag{3.18}$$

where $\boldsymbol{F}_i$ are the columns of the **F** matrix. Alternatively, since the matrix with $\boldsymbol{D}_i$ as its columns, which we denote **D**, is diagonal, then $\mathbf{F} = \mathbf{P}\mathbf{D}^{-1}$, where **P** is the perturbation matrix with $\boldsymbol{P}_i$ as its columns and the superscript "-1" denotes the matrix inverse.

To fit the smoothed VL1 data, we assume:

$$\boldsymbol{Y} = \boldsymbol{X}_0 + \mathbf{P}\boldsymbol{\alpha} + \boldsymbol{\varepsilon}, \tag{3.19}$$

where $\boldsymbol{Y}$ denotes the smoothed VL1 data, $\boldsymbol{\alpha}$ is a column vector (5-by-1) of linear combination coefficients, and $\boldsymbol{\varepsilon}$ is a column vector (669-by-1) of residuals. We find the best-fit linear combination coefficient via an iterative method that minimizes the L2 norm (the root mean square) of $\boldsymbol{\varepsilon}$. Hence, we define a quadratic cost function that gauges the (possibly weighted) magnitude of the residual vector:

$$C(\boldsymbol{\alpha}) = 0.5 \times \boldsymbol{\varepsilon}^{\mathrm{T}}\mathbf{W}\boldsymbol{\varepsilon} = 0.5 \times (\boldsymbol{Y} - \boldsymbol{X}_0 - \mathbf{P}\boldsymbol{\alpha})^{\mathrm{T}}\mathbf{W}(\boldsymbol{Y} - \boldsymbol{X}_0 - \mathbf{P}\boldsymbol{\alpha}), \tag{3.20}$$

where $\mathbf{W}$ is a diagonal matrix that can be used to assign uneven weights to elements of the noise vector at different times of the year (if desired). The cost function in Equation 3.20 is of a standard form and can be easily minimized by many different algorithms; because $\boldsymbol{\alpha}$ has only 5 or 7 elements here, we employ a straightforward downhill simplex method. When the minimizing algorithm reaches a (possibly local) minimum for the cost function C, the corresponding $\boldsymbol{\alpha} = \boldsymbol{\alpha}_f$ minimizes $\boldsymbol{\varepsilon}$. The obtained best-fit for $\boldsymbol{Y}$ based on the linear combination is then

$$\boldsymbol{X}_f = \boldsymbol{X}_0 + \mathbf{P}\boldsymbol{\alpha}_f. \tag{3.21}$$

As the ultimate goal of this method is to find the MarsWRF parameter set that best-fits the smoothed VL1 record, we need to relate $\boldsymbol{X}_f$ in Equation 3.21 to $\boldsymbol{A}_f$, the best-fit parameter set. If the linear truncation of the Taylor series in Equation 3.16 holds, then changes in $\boldsymbol{X}$ can be linearly related to changes in $\boldsymbol{A}$, as in Equation 3.17. Hence, we assume that the best-fit parameter vector is related to the baseline parameter vector by the same

linear combination coefficients that relate the best-fit pressure cycle to the baseline pressure cycle prediction:

$$\boldsymbol{A}_f = \boldsymbol{A}_0 + \mathbf{D}\boldsymbol{\alpha}_f. \tag{3.22}$$

In order to gauge the success of the fitting method, and thus the validity of the linearity assumption, one must run MarsWRF with parameters $\boldsymbol{A}_f$ and apply the interpolation and smoothing operator to the output:

$$\boldsymbol{X}'_f = \mathrm{F}(\boldsymbol{A}_0). \tag{3.23}$$

If $\boldsymbol{X}'_f$ is very similar to the linear method prediction, $\boldsymbol{X}_f$ (and eventually $\boldsymbol{Y}$), then we can be assured the linearity assumption was valid. If $\boldsymbol{X}'_f$ and $\boldsymbol{X}_f$ ($\boldsymbol{Y}$) differ substantially, then one must re-evaluate use of this method, though we have found that for poorly chosen baseline parameters, successive applications of the method can eventually yield an acceptable solution for $\boldsymbol{A}_f$.

When we write $\boldsymbol{X} = \mathrm{F}(\boldsymbol{A})$, we consider the surface pressure to be a function of the albedo and the emissivity of the polar caps, and the total mass of CO_2 in the system (the extended vector also considers the thermal inertia of the subsurface ice table). By virtue of the linearity assumption, this method effectively "retrieves" these parameters $\boldsymbol{A}_f$, from observations of surface pressure, even though the involved operators (I and W) are non-linear. In this respect, this linear fitting method is not new. The method is essentially a standard practice in atmospheric spectroscopy data retrieval (e.g., [*Guo et al.*, 2007]) and data assimilation (e.g., [*Menemenlis et al.*, 2005]).

3.4 Results

3.4.1 Standard fitting with emissivity, albedo, and total CO_2 mass

We obtain a positive perturbation matrix, $\mathbf{P}^+$, to replace $\mathbf{P}$ in Equation 3.19:

$$\mathbf{P}^+ = [\boldsymbol{P}_1\ \boldsymbol{P}_2\ \boldsymbol{P}_3\ \boldsymbol{P}_4\ \boldsymbol{P}_5]. \tag{3.24}$$

We describe it as "positive" because all the columns in $\mathbf{P}^+$ were obtained by setting one of the five parameters larger than that in the baseline case and differencing the resulting pressure cycles. Similarly, we can construct a negative perturbation matrix $\mathbf{P}^-$ based on negative perturbations. We fit the VL1 pressure record with these two perturbation matrices and obtain two best-fit parameter vectors (also listed in Table 3.1):

$$\boldsymbol{A}^+_{f4.1} = [0.796\ 0.484\ 0.467\ 0.787\ 0.978]^T, \text{ and} \tag{3.25}$$

$$\boldsymbol{A}^-_{f4.1} = [0.793\ 0.485\ 0.454\ 0.784\ 0.978]^T. \tag{3.26}$$

The values in these two parameter vectors are very close. We average the two best-fit parameter sets to get the average best-fit parameter vector:

$$\boldsymbol{A}_{f4.1} = [0.795\ 0.485\ 0.461\ 0.785\ 0.978]^T. \tag{3.27}$$

The two linear fits corresponding to $\boldsymbol{A}^+_{f4.1}$ and $\boldsymbol{A}^-_{f4.1}$, and their average are shown in the upper panel of Figure 3.4; their residuals are shown in the lower panel. All fitted curves match very closely with the smoothed VL1 data. The largest mis-fits are found in the northern winter, when baroclinic waves are the most active [*Hess et al.*, 1977]. The largest error is less than 10 Pa, or about 1% of the annual maxima.

We use the average parameter vector $\boldsymbol{A}_{f4.1}$ to drive MarsWRF. Figure 3.5 shows the resulting model output. The pressure cycles corrected for VL positions are indicated by the black and the grey curves in the upper panel. The smoothed model surface pressure cycles (green and magenta dashed curves) show great agreements with the smoothed VL data (red and blue dashed curves) at both landing sites (note that only the VL1 data was used for the fit). The lower panel of Figure 3.5 shows the difference between the smoothed simulation and the smoothed data. For the VL1 site, the error is always less than several Pascal. The residual mean is 0.3 Pa and the standard deviation is 3.2 Pa. The RMS of the residual is 3.2 Pa, or 0.35 to 0.48% of the seasonal cycle. MarsWRF predicts slightly higher surface pressure near Ls 20° and 240°, lower surface pressure near Ls 150° and 270°. Similar, if not identical, residual patterns can be found in the linear fit (blue dashed line in the lower panel of Figure 3.4). It suggests that our final perturbation to $\boldsymbol{A}_0$ is small enough for linearity to hold (Equation 3.19). In this regime, the operator F can be considered close to linear. The translation back to the parameter space is therefore valid and reflected directly in the forward model (i.e., MarsWRF) output.

We notice that the smoothed surface pressure cycle at the VL2 site follows the observation closely in most of the year, but does not line up perfectly with the observations in the northern winter and around Ls 50°. Because we do not perform the pressure fitting for the VL2 data, such discrepancy is not surprising. Nonetheless, the fact that the model agrees with data even at the VL2 site for the majority of the year is impressive. It suggests that the hydrostatic assumption and the dynamics in MarsWRF are consistent with what actually happens on Mars. If pressure records at both VL sites are to be fit simultaneously, we would need to include the VL2 pressure responses in the perturbation matrix and in the definition of

the cost function. A trade-off of accuracy between the two landing locations is therefore expectable. For the reasons discussed at the beginning of section 3.3, we decided to perform the fitting only for the VL1 pressure cycle.

If achieving a better fit for a desired time frame is the goal, we can adjust the weighting assigned to different periods of time by modifying matrix **W** in the definition of the cost function (Equation 3.20). In Figure 3.4 and Figure 3.5, one can find a subtle phase error at the pressure minima near Ls 150°. In order to improve the fitting quality at this season, we weight this period relatively more in the calculation of the cost function. We chose to assign 50 times the normal weighting to southern winter (Ls 125° to 175°), 10 times to southern summer (Ls 225° to 275°) and normal weighting at all other times. With the updated weight matrix, the following best-fit parameter vectors are given by the linear fitting method (also shown in Table 3.1):

$$\boldsymbol{A}^{+}_{f4.2} = [0.814\ 0.424\ 0.461\ 0.744\ 0.966]^{T}, \text{ and} \tag{3.28}$$

$$\boldsymbol{A}^{-}_{f4.2} = [0.820\ 0.434\ 0.433\ 0.764\ 0.971]^{T}. \tag{3.29}$$

We average the two to obtain:

$$\boldsymbol{A}_{f4.2} = [0.817\ 0.429\ 0.447\ 0.754\ 0.968]^{T}. \tag{3.30}$$

This parameter vector provides an excellent linear fit as well, with residual mean of 0.5 Pa and standard deviation of 4.6 Pa. When validated using MarsWRF, the RMS of the residual is 4.8 Pa, or 0.53 to 0.70% of the pressure level. In both linear fit and model output, the residual in the southern winter (Ls 125° to 175°) is smaller and the phase shift is less

evident. The trade off, however, is that the errors at other seasons become larger, which leads to a larger total RMS error.

The experiments above suggest that the southern seasonal cap has low albedo and high emissivity, while the northern seasonal cap has high albedo and low emissivity. There is no intuitive explanation for why the two seasonal CO_2 caps would have opposite radiative properties. Observation from TES and Viking IRTM do not support such a dichotomy in general [*Kieffer et al.*, 1977; *Kieffer and Titus*, 2001; *Paige et al.*, 1994; *Paige and Keegan*, 1994]. With just the fitting parameters used in this section, the southern parameters seem to match the observation from spacecrafts much better than those retrieved for the north.

3.4.2 Fitting with extended parameterization of subsurface water ice

Since the conventional five parameter fit does not provide physically sound seasonal cap albedos and emissivities, especially in the north, we try to improve the picture by including the subsurface layer thermal property as fitting parameters. As demonstrated in section 2.3, sensitivity studies show that the water ice table thermal inertia has a similar footprint to that of the emissivity. On the other hand, it does not project a change in the surface pressure cycle that is as "linear" as that of emissivity. However, as long as the perturbation is not too large, we can tentatively assume that the linear relationship holds.

First, we try to extend the parameter vector to seven dimensions by adding the thermal inertia of the water ice table in the two hemispheres to the parameter vector. We extend the baseline parameter by two more dimensions as well and re-write the baseline parameter vector as

$\boldsymbol{A}_0 = [0.770\ 0.570\ 0.500\ 0.800\ 1.00\ 0.275\ 0.275]^{\mathrm{T}}$.

The first five dimensions are defined as before. The sixth and seventh dimensions correspond to the thermal inertia of the water ice table in the north and south. In the baseline case, the subsurface is completely filled with dry soil. Therefore, the thermal inertia of the water ice table is assumed to be 275 J m^{-3} K^{-1}, which is a value for average dry Martian soil. The perturbation vector **P** is also extended to

$$\mathbf{P} = [\boldsymbol{P}_1\ \boldsymbol{P}_2\ \boldsymbol{P}_3\ \boldsymbol{P}_4\ \boldsymbol{P}_5\ \boldsymbol{P}^e_6\ \boldsymbol{P}^e_7]. \tag{3.31}$$

Note that $\boldsymbol{P}^e_6$ and $\boldsymbol{P}^e_7$ were calculated with a different baseline value of the water ice table thermal inertia. In order to perform the linear fitting, we need to assume that these two pressure perturbation vectors do not change regardless of the baseline value. Undertaking a sensitivity study, we find that this is a reasonable assumption for the baseline values of 275 and 1200 J m^{-3} K^{-1} (later in this section, we will see a case in which this assumption needs to be re-evaluated). Therefore, we use the same linear fitting method and obtain a new best-fit parameter vector

$$\boldsymbol{A}_{f4.3} = [0.790\ 0.505\ 0.474\ 0.788\ 0.977\ 0.523\ 0.300]^{\mathrm{T}}. \tag{3.32}$$

This parameter vector has no essential difference to what we obtain from the conventional five-dimensional fit ($\boldsymbol{A}_{f4.1}$). The corrections to the parameters are just a few thousandths. When validated with MarsWRF, the residual pattern is very similar to before with slightly higher RMS error (about 3.97 Pa). It suggests that including a water ice table thermal inertia as fitting parameters will not produce a great improvement in the fitting. Thus, the conventional five-dimension fit is sufficient for most atmospheric studies, in which the important thing is to obtain a surface pressure cycle that is within instrument error, while the

accuracy of the retrieved frost radiative properties are considered less relevant (and indeed, obviously incorrect values can be tolerated, on the assumption that non-modeled physics are aliased in these values).

As discussed by *Haberle et al.* [2008], the significance of including subsurface ice is in a desire to gain physical consistency, i.e., being able to fit the VL pressure cycles with reasonable frost properties. An experiment with subsurface water ice is initiated using unity frost emissivity, relatively small frost albedos, and fixed and uniform depths to the water ice table (Figure 3.2) as suggested by *Haberle et al.* [2008]. We find that MarsWRF is able to produce a pressure cycle reasonably close to that measured by VL1 (Figure 3.6, consistent with prior "by-eye" fitting but not as close as our five-parameter retrieval). While the amplitude of the cycle agrees well with the observation, the major discrepancy between the simulation and data is in the first half of the year, where the phases of the two curves do not perfectly agree. The same mismatch in phase can be identified in the NASA Ames Research Center (ARC) Mars GCM simulations.

The depth to the ice table will not be uniform in latitude or longitude, yet the depth to the ice table would seem relatively readily predicted by simple 1D water exchange models. Following the philosophy of trying to find the most physically reasonable fit parameters, we decided to employ latitudinally-varying depths to the water ice table derived by *Schorghofer and Aharonson* [2005]. When we used these depths values and reduce the thermal inertia for the water ice tables from 2200 J m^{-3} K^{-1}, MarsWRF is able to reproduce a reasonable fit to the VL pressure cycles (Figure 3.7). The quality of the fit is similar to that using the ARC GCM setup, with the same phase mismatch during the northern summer. In this simulation, the water ice table top depends on latitude, and the thermal inertia assumed for the water ice

table is not as high as pure water ice, with larger values in the north. If the same mixing ratio of water to dry soil in the water ice table is also assumed, we found that the thermal inertia of the dry soil in the north is higher than the south, which agrees with IRTM and TES surface thermal inertia maps.

Our sensitivity study has already shown that the seasonal cap emissivity and the water ice table thermal inertia have very similar footprints in the VL pressure cycle. In other words, the role of emissivity in the linear fitting may be replaced by the water ice table thermal inertia (and by extension, the emissivity from the conventional five-parameter fit may include aliased effects of thermal inertia variations). Therefore, we proceed to do the numerical fitting with unity emissivity for the seasonal caps and instead vary the water ice table thermal inertia. In this case, the parameter vector still has five dimensions but the two dimensions corresponding to the seasonal cap emissivity are replaced by the thermal inertia of the water ice table in the north and south (their depth derived by *Schorghofer and Aharonson* [2005]). We construct a new perturbation matrix:

$$\mathbf{P} = [\boldsymbol{P}_1\ \boldsymbol{P}_3\ \boldsymbol{P}_5\ \boldsymbol{P}^e{}_6\ \boldsymbol{P}^e{}_7]. \tag{3.33}$$

We perform the same linear fitting and obtain a parameter vector

$$\boldsymbol{A}_{f4.4} = [0.696\ 0.528\ 0.994\ 2.90\ 1.60]^{\mathrm{T}}. \tag{3.34}$$

The five parameters now correspond to the northern cap albedo, the southern cap albedo, the total CO_2 mass, the thermal inertia for the northern water ice table, and the thermal inertia for the southern water ice table, respectively. The quality of this fit is lower than the former five-dimensional experiments. The annual RMS error is 11.4 Pa, larger than the fits before. When validated using MarsWRF, this parameter vector does not generate a

pressure cycle close to that of VL1 measurement as the linear fitting method predicts. We notice that in the new best-fit parameter, the projected thermal inertia for the subsurface layer reaches 2900 and 1600 J m^{-3} K^{-1}. In the northern hemisphere, the projected value is so far away from the baseline of 1200 J m^{-3} K^{-1} that it is likely that the linear approximation is no longer valid.

In order to fix the breakdown of the linearity assumption, we introduce two new parameter vectors:

$$\boldsymbol{A}_{4.5} = [0.696\ 0.528\ 0.994\ 3.50\ 1.60]^{T}, \text{ and} \tag{3.35}$$

$$\boldsymbol{A}_{4.6} = [0.696\ 0.528\ 0.994\ 2.90\ 2.20]^{T}. \tag{3.36}$$

We use the parameter vector $\boldsymbol{A}_{f4.4}$ specified in Equation 3.34 as the new baseline parameter vector and calculate two new pressure perturbation vectors ($\boldsymbol{P}^{e''}_{6}$ and $\boldsymbol{P}^{e''}_{7}$) associated with perturbation parameter vector $\boldsymbol{A}_{4.5}$ and $\boldsymbol{A}_{4.6}$. $\boldsymbol{P}^{e''}_{6}$ and $\boldsymbol{P}^{e''}_{7}$ are the surface pressure response to water ice table thermal inertia with respect to a new baseline pressure. We find that $\boldsymbol{P}^{e''}_{6}$ and $\boldsymbol{P}^{e''}_{7}$ do differ from $\boldsymbol{P}^{e}_{6}$ and $\boldsymbol{P}^{e}_{7}$, and therefore we updated the fourth and fifth columns in the perturbation matrix (Equation 3.33) accordingly. By updating the perturbation matrix, we hope to limit the final perturbation in thermal inertia to a relatively small amount. With the new perturbation matrix **P** and the new baseline pressure cycle, we perform the linear fitting again. The best-fit parameter vector thus retrieved is:

$$\boldsymbol{A}_{f4.7} = [0.731\ 0.546\ 0.948\ 3.90\ 1.80]^{T}. \tag{3.37}$$

Notice that the project thermal inertia values are close to the new baseline values. This helps maintaining the linearity of this problem. The new fitting result is shown in Figure

3.8. The RMS error of the residual is roughly 6.9 Pa. When these parameters are used in MarsWRF, we are able to replicate the VL1 record very well (shown in Figure 3.9). The RMS of the error is 8.7 Pa, slightly larger than that of the linear combination residual or the retrieval or prior five-parameter fit, but satisfactory. No obvious phase disagreement between the two smoothed curves can be found.

In summary, we succeed in fitting the VL data with the values of the albedos of the seasonal caps, the total CO_2 inventory and the subsurface layer thermal inertia, along with an assumption of unity seasonal cap emissivity. Although the retrieved albedo of the northern seasonal cap is still higher than the south, the albedo values are closer to the observation. The linear fitting results suggest that polar regolith with a higher thermal conductivity (due to subsurface water ice) is able to represent (at least a significant proportion of) the extra heat source in autumn and winter that used to be provided by excessively low cap emissivity in studies prior to *Haberle et al.* [2008]. The best-fit thermal inertia values are very different in the two hemispheres, mainly to explain the different pressure levels during northern and southern winters. The predicted thermal inertia of the northern water ice table is much larger than that of the south, suggesting some sort of dichotomy in the thermal property between the two hemispheres. We will discuss this issue in the following section.

3.5 Discussions of parameterization

3.5.1 Albedo and emissivity

Although albedo and emissivity may be model dependent parameters, their physical interpretations are universal. By definition, albedo describes the fraction of solar energy reflected back to space while emissivity measures the fraction of energy in the black body curve for a surface of given kinetic temperature that is released from that emitter. If we first look at the retrievals without consideration of subsurface water ice, the five parameter linear fit suggests that the southern seasonal cap has lower albedo (0.461) and higher emissivity (0.785) than the north (0.795 and 0.485 respectively). For these experiments, MarsWRF was not run in a mode to account for activities that change the effective albedo and emissivity (such as clouds, dust storms, etc.). Therefore, the best-fit parameters not only characterize the seasonal caps but also provide hints as to other physical processes implicitly important to MarsWRF in the polar regions.

3.5.1.1 Southern seasonal cap

When surface CO_2 ice is mixed with dust, its albedo and emissivity change significantly. Assuming the same grain size of ice, a dustier deposit can produce a much less reflective and much more emissive surface material [*Kieffer et al.*, 2000]. Hence, we expect that we can attribute many of the albedo and emissivity characteristics to the dust activity, which is usually stronger in the southern hemisphere [*Basu et al.*, 2004; *Martin*, 1986; *Smith*, 2004]. However, it is less clear that increases in dust result in a generally darker and more emissive cap [*James et al.*, 2000].

Isotropic albedo (usually slightly higher than Lambert albedo) was mapped by TES [*Kieffer et al.*, 2000]. The southern seasonal cap in general had albedos of 0.45 to 0.5, with lower values (about 0.3) in the so-called "Cryptic regions" and higher values (0.6 to 0.7) in the bright cap. On average, TES observations agree very well with the albedo predicted by the linear fit model for the south pole. Lambert albedo was also mapped by IRTM aboard the Viking orbiters. It ranged from 0.2 to 0.5 in the south [*Paige and Keegan*, 1994]. The region with an albedo 0.5 corresponded to the residual cap rather than the seasonal cap. Since the southern residual cap is believed to consist of mostly CO_2 ice [*Paige and Ingersoll*, 1985], the IRTM observations for the CO_2 cap are also consistent with our linear fit prediction. The Hubble Space Telescope has reported higher southern seasonal cap albedos for the bright cap region [*James et al.*, 2005].

We did not account for atmospheric CO_2 cloud formation and precipitation with microphysical calculations in this version of MarsWRF (when the atmospheric temperature falls below the saturation point temperature for CO_2 condensation, the model instantaneously deposits the corresponding condensed CO_2 ice on the ground). It is believed that atmospheric CO_2 condensation may affect the atmospheric state [*Colaprete et al.*, 2008] and CO_2 snowfall could contribute to the low brightness temperature or equivalently the low emissivity observed by various missions [*Colaprete et al.*, 2005; *Forget et al.*, 1999]. Some models have made efforts to relate the change in surface (seasonal cap) emissivity to the amount of condensed CO_2. *Forget et al.* [1998] used an empirical function to adjust the seasonal cap emissivity based on the atmospheric CO_2 condensation and precipitation rate. Using Equation 3.5 of that paper, we calculate an average adjustment to the seasonal cap emissivity due to CO_2 snow. For the southern cap, this correction is about 0.15. When subtracted from the

reference value of 0.95, the effective emissivity is about 0.8, which is very close to our best-fit value. In other words, if CO_2 snow is important, our time-constant parameterization may be effectively capturing this physical phenomenon while avoiding complexity in computation.

3.5.1.2 Northern seasonal cap

Measurements of the northern seasonal cap albedo made by TES [*Kieffer and Titus*, 2001] are lower than our best-fit value, and so are the IRTM observations [*Paige et al.*, 1994; *Paige and Keegan*, 1994]. The polar hood cloud, which is usually seen in the winter time [*James et al.*, 1992; *James et al.*, 1994; *Wang and Ingersoll*, 2002], could contribute to the excessively high retrieved albedo of the northern cap. Furthermore, polar hood clouds are seen much less often in the southern hemisphere, and the retrieval results show that little correction is needed for the albedo of the southern cap, which stays relatively close to the observations. Although the radiative effects of hood clouds are not modeled by MarsWRF, the five-parameter set predicts the atmospheric mass budget for Mars very well. If hood cloud effects are significant, the retrieval scheme is effectively capturing (and aliasing) these effects into the northern seasonal cap retrieved albedo by increasing the best-fit albedo by 0.3 to 0.4 relative to the observations.

When the effect of dust on the surface CO_2 ice cap is ignored, emissivity can be considered as a function of the porosity of the CO_2 frost: more porous ice tends to have lower emissivity [*Eluszkiewicz et al.*, 2005]. Our best-fit emissivity in the north is much lower than that in the south, suggesting a potentially much more porous CO_2 ice slab in the north. Porosity data of the two seasonal caps, which would provide a direct evaluation of our

argument, are not yet available. However, the implication is at least consistent with the extremely low density of the northern seasonal cap [*Aharonson et al.*, 2004].

Finally, it should be noted that a good fit to the VL pressure data can still be obtained when the northern cap emissivity is assumed to be unity as long as subsurface water ice effects are included. Thus the degree to which the low northern emissivities must be explained is itself questionable.

3.5.2 CO_2 inventory

3.5.2.1 Annual variation

The global CO_2 inventory cycle divided into different reservoirs is plotted in Figure 3.10. Our best-fit cases suggest that the total CO_2 in the surface-atmosphere system is about 2.83×10^{16} kg, which agrees to within 5% of the NASA ARC GCM [*Kelly et al.*, 2006]. Up to 26% of the total CO_2 (7.45×10^{15} kg) participates in the seasonal exchange between the atmosphere and the caps, slightly larger than the ARC GCM predictions, but consistent with earlier estimation [*James et al.*, 1992; *Kelly et al.*, 2006].

As discussed in the sensitivity study, the amount of surface CO_2 ice in MarsWRF is mainly determined by the albedo and emissivity of the corresponding seasonal caps. The prediction of surface CO_2 in the southern hemisphere by MarsWRF matches closely with the GRS observations. In the north, our prediction is slightly higher than GRS observations [*Kelly et al.*, 2006]. Ideally, GCMs should be able to simulate both surface CO_2 deposition and VL site pressure cycles that agree well with the available observations, thus yielding an

estimate of the total "active" CO_2 budget in the system. Slight disagreements in simultaneously fitting the seasonal cap masses and lander pressure curves could result from interpolation errors given the relatively poor model resolution (5° × 5.625°), missing sources and sinks of CO_2 (regolith), or instrument error.

3.5.2.2 Permanent Polar Caps

A permanent CO_2 cap exists at the Martian southern pole [*Kieffer et al.*, 1977]. No published GCM predicts the existence of such a residual cap, and instead a residual cap must be prescribed in the model boundary conditions (often simply as a fixed surface temperature at the CO_2 frost point). We have found that permanent CO_2 caps will appear in MarsWRF only if extreme parameters (e.g., very high albedo values) are used, which agree with *Wood and Paige* [1992].

The best-fit parameter sets, which lead to good replications of the VL pressure cycle, do not produce permanent CO_2 caps. This is not unexpected. Other GCMs do not produce permanent caps while trying to fit the VL pressure cycles [*Haberle et al.*, 2008]. As stated in the introduction, *Wood and Paige* [1992] used a simple one dimension model for the thermal calculation to find the best parameter set to fit the VL pressure cycle. They pointed out that with their best-fit values, the permanent cap is absent in both poles. We verified their conclusion once again using a much more sophisticated model (a GCM) that something "special" is happening in the heat balance at the south residual cap to somehow allow its existence. This is possibly due to an insolation-dependent albedo [*Guo et al.*, submitted-b; *James et al.*, 1992].

3.5.3 Subsurface water ice

As discussed in the sensitivity study, most of the subsurface water ice layer's footprint on the VL pressure cycle can be represented by a linear combination of the seasonal cap albedo and emissivity. Fitting using subsurface water ice (via the effects on subsurface conductivity) does not give particularly better fits. Rather, the advantage of fitting using surface ice is in retrieving cap properties that are more physically plausible. Subsurface water ice contributes directly to the seasonal energy balance, which is the driver of the CO_2 annual cycle. Larger thermal conductivity provides the missing heat source in the energy balance in local winter, which before was represented by unrealistic frost albedo and emissivity. Its potential was already demonstrated in the GCM study by *Haberle et al.* [2008].

The biggest difficulty in completing the picture is that we do not know precisely how deep the water ice is buried, what the water content is in the ice table, and how things change over time. The current assumptions in MarsWRF and ARC GCMs are more or less arbitrary. They are not backed up by many systematic observations, although the Phoenix Lander observations do support the kind of ice table depth modeling undertaken by *Mellon and Jacosky* [1993] and *Schorghofer and Aharonson* [2005]. On the other hand, given very accurate measurements of the albedo and emissivity of the seasonal caps, we would likely be able to use the technique we have described to retrieve the (bulk) properties of subsurface water ice.

The fit with CO_2 albedo, total CO_2 mass, and water ice table thermal inertia suggests much higher thermal conductivity for the subsurface layer in the north, to at least several meters below the surface. Since the spatial coverage of the water ice table is very different in the two hemispheres according to the GRS measurements (Figure 3.2), the difference in the

conductive properties per unit mass of the regolith must be even larger. This is potentially a constraint on the nature of the Martian near-surface regolith. The crusts of the two hemispheres have long been known to differ [*Neumann et al.*, 2004; *Watters et al.*, 2007], it therefore may not be surprising to find they have different thermal conductive properties (or different abilities to accommodate highly conductive water ice).

GRS reported hydrogen content and equivalent water content distributions (Figure 3.2) near the Martian surface [*Feldman et al.*, 2004]. Assuming water ice occupies all the pores in the soil, and knowing the densities of water ice (900 kg/m^3) and Martian crust (2900 kg/m^3 [*Zuber et al.*, 2000]), we can back out the porosity of the soil. If we make two more assumptions: first, the subsurface maintains the same porosity through the vertical column considered and that the pores are completely filled with water ice; second, the dry soil thermal conductivity in the subsurface is the same as the surface, whose equivalent thermal inertia is provided by TES [*Putzig et al.*, 2005], we can derive the thermal inertia of the subsurface mixture of soil and water ice (shown in Figure 3.11). An obvious north-south dichotomy in thermal inertia map can be seen. Zonal average subsurface thermal inertia ranges from 300 to 1400 J m^{-3} K^{-1} in the north, with a maximum of 1730 J m^{-3} K^{-1}. In the south, the zonal average varies between 220 and 540 J m^{-3} K^{-1}; this is on average about two to three times smaller than in the north. This dichotomy is due to the combined effects of high water ice content and high soil thermal inertia in the northern polar region. We notice that the values of thermal inertia obtained from this calculation are smaller than suggested by the retrieval scheme. There are ways to reduce this gap since the best-fitted thermal inertia values could be misleading: MarsWRF assumes constant density and thermal capacity for the subsurface material. A decrease in dry soil density and/or heat capacity will decrease the

thermal inertia while keeping the thermal conductivity the same. One may also argue that the GRS may under-predict the water ice content and therefore the soil porosity. Setting those possibilities aside, there is an important common message from these two independent studies, i.e., there exists a significant north-south dichotomy in the subsurface thermal conductivity in the polar regions.

When we fix the seasonal cap emissivity to unity, we still need to adjust the seasonal cap albedos in order to make the seasonal pressure cycle phase match observations. This suggests that the inclusion of the water ice table, while improving physicality, is not the panacea — we do not yet have a complete and satisfactory understanding of the processes controlling the CO_2 cycle. In order to build a better Mars GCM, we need to build more physically-based prognostic models for the frost albedo and emissivity, capturing processes now implicitly aliased into our retrieved cap properties.

3.5.4 Limitation of the linear fitting method

As we discussed in section 3.3, the linear fitting algorithm assumes the response in surface pressure scales linearly with the perturbation of the fitting parameters. In MarsWRF, this assumption becomes less valid when the perturbation is large, especially for perturbations to the water ice table thermal inertia. For example, in panel (b) of Figure 3.3, when we perturb the thermal inertia baseline by 1000, 2000 and 3000 J m^{-3} K^{-1}, the responses of the latter two are not simple multiples of the first. The perturbation matrix may change greatly when the baseline parameter vector moves to a different state. It may influence the calculation of the cost function and the iterative method — the last case from

section 3.4.2 provides a good demonstration of these effects. If this is the case, we need to recalculate the pressure perturbation vectors to maintain linearity.

The pattern of the perturbation matrix changes drastically in extreme situations. More specifically, MarsWRF does not respond to further change of parameters after critical values are reached. For instance, in Figure 3.3, raising the water ice table thermal inertia by 3000 J m^{-3} K^{-1} does not increase the surface pressure much more than raising it by 2000 J m^{-3} K^{-1}. In another situation where the frost albedo is too high, a permanent cap will form in the corresponding pole. One can easily imagine that the pressure response would have a very different pattern.

Another related limitation of the iterative algorithm is that it is sensitive to the choice of the starting parameter vector. Starting the fitting with $\boldsymbol{Y}_1 = F(\boldsymbol{A}_1)$ may produce a different best-fit parameter vector than starting with $\boldsymbol{Y}_2 = F(\boldsymbol{A}_2)$, but both may yield comparable RMS errors. When used in MarsWRF, however, they may correspond to very different VL pressure cycles and RMS errors. Some are closer to the observations than the others. We have to choose the desired sets based on their performances in the GCM and their physical soundness.

Ideally, we should force the perturbations to be very small and re-calculate the perturbation matrix for each iterative step. However, this would make the fitting extremely slow due to the greater number of required iterations and, more importantly, more GCM runs to calculate the perturbation matrices. Fortunately, we can assume the perturbation matrix does not change for most of our retrievals. We also carefully selected the starting point of the iteration to make the process stable.

3.6 Conclusions

We provide a method to obtain close fits to the VL surface pressure data using a chosen subset of "tunable" parameters within Mars General Circulation Models. We construct a set of basis vectors by perturbing five parameters in the GCM, including albedo and emissivity for the seasonal CO_2 caps in both poles and the total amount of CO_2 in the system. We utilize an iterative method to find the best linear combination of the basis vectors that minimizes the least squares error between the fit and the VL data. The coefficients for the linear fit are then projected back to parameter space and a best-fit parameter set is obtained. When used in MarsWRF, this parameter set yields a pressure cycle very close to the VL observations as predicted by the linear method. (In this sense, our method is related to ensemble data assimilation)

The method described in this chapter provides a first rigorous and quantitative means for fitting the seasonal pressure cycle with a GCM. As designed, we expect that this method would be useful for calibrating the CO_2 cycle in any model and thus could provide a benchmark method for tuning GCMs. The study confirms the idea that a simple parameterization has the potential to capture most of the underlying physics of the CO_2 cycle [*Wood and Paige*, 1992]. In the linear fit, the best-fit parameters qualitatively show footprints of the physical processes that are not explicitly represented in MarsWRF but effectively captured by the parameterization, such as the presence of cloud, precipitation of atmospheric CO_2 ice, surface frost with different porosity, etc.

While the mathematics of the approach is elegant, the retrieved parameters are not guaranteed to be in agreement with direct observations. For instance, the cause of the big

difference in the retrieved radiative properties of the two seasonal caps is not thoroughly understood. Attributing the differences to specific un-modeled physical process will require further work, along the philosophical lines laid out in the Introduction. However, our method provides a road map for the procedure of unveiling all relevant physics. We start with the simplest parameter set that fits the data well. Wherever the retrieved parameters differ from observed or physically sound values, we must look for further unresolved (un-modeled) physical processes. For example, parameterizations of clouds, dirty frost, etc., are likely still required. The soil thermal property change due to the presence of subsurface water ice is one such piece of physics we added in this study. Both MarsWRF and the NASA ARC Mars GCM have verified that including the subsurface ice improves the physical soundness of retrieved cap properties.

Our simulations suggest that the northern subsurface layer has higher thermal conductivity than the south. This argument is also supported by GRS and TES observations. This bias in the inferred thermal conductivity may be related to differences in the water cycle, in the ability of the regolith materials in the two hemispheres to accommodate water, and/or in the regolith conductivity itself.

Finally, none of the retrievals reproducing reasonable pressure curves are able to simultaneously yield a residual CO_2 ice cap at the south. This may suggest that assumptions such as the temporally constant values of the retrieved cap properties may not be completely valid.

Tables

Table 3.1

Methods	Parameters				
	Northern cap albedo	Northern cap emissivity	Southern cap albedo	Southern cap emissivity	Total mass of CO_2 in system*
Positive perturbation,	0.796	0.484	0.467	0.787	0.978
Negative perturbation,	0.793	0.485	0.454	0.784	0.978
Average, constant weighting ($\boldsymbol{A}_{f4,1}$)	0.795	0.485	0.461	0.785	0.978
Positive perturbation, non-	0.814	0.424	0.461	0.744	0.966
Negative perturbation, non-	0.820	0.434	0.433	0.764	0.971
Average, non-constant weighting ° ($\boldsymbol{A}_{f4,2}$)	0.817	0.429	0.447	0.754	0.968

* Mass index number, 1.0 corresponds to total mass 2.90×10^{16} kg of the baseline case.

Figures

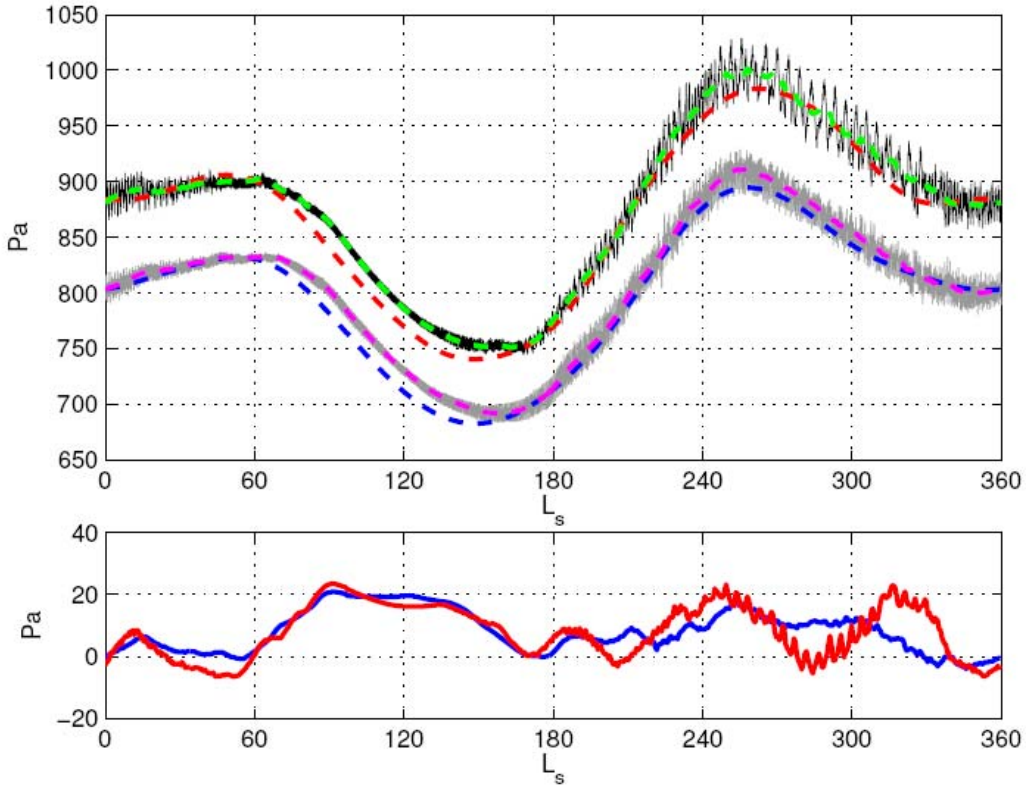

Figure 3.1: Upper panel, annual cycles of the surface pressure at the VL sites for the control case (northern seasonal cap albedo: 0.77; northern seasonal cap emissivity: 0.57; south albedo: 0.5; south emissivity: 0.8; total CO_2 mass index: 1.0). Grey line: MarsWRF outputs (separate by 6 hours, or 4 output per sol) at VL1 location; magenta dashed line: smoothed (9 sol running average) MarsWRF outputs at VL1 location; black line: MarsWRF output at VL2 location; green dashed line: smoothed MarsWRF outputs at VL2 location; blue dashed line: polynomial fit to the VL1 observations; red dashed line: polynomial fit to the VL2 observations [*Tillman et al.*, 1993]. Lower panel, difference between the polynomial fits of VL measurements and MarsWRF simulation: Blue line: VL1 site; red line: VL2 site.

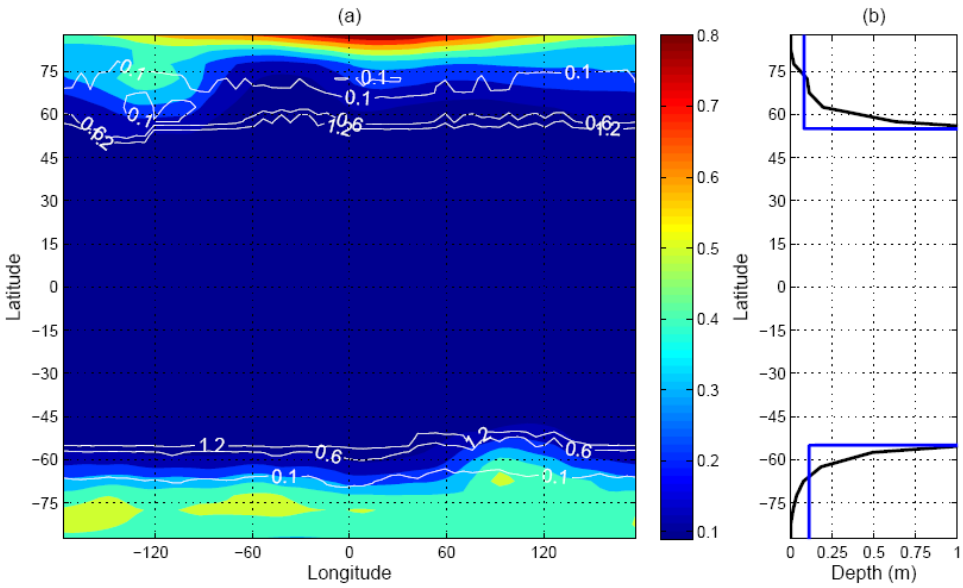

Figure 3.2: (a) Color: subsurface ice content from GRS; white contour: depth of permanently stable water ice in meters suggested by *Schorghofer and Aharonson* [2005]. (b) Black curve: zonal average of the depth of permanently stable water ice table; blue curve: ice table depth suggested by *Haberle et al.* [2008].

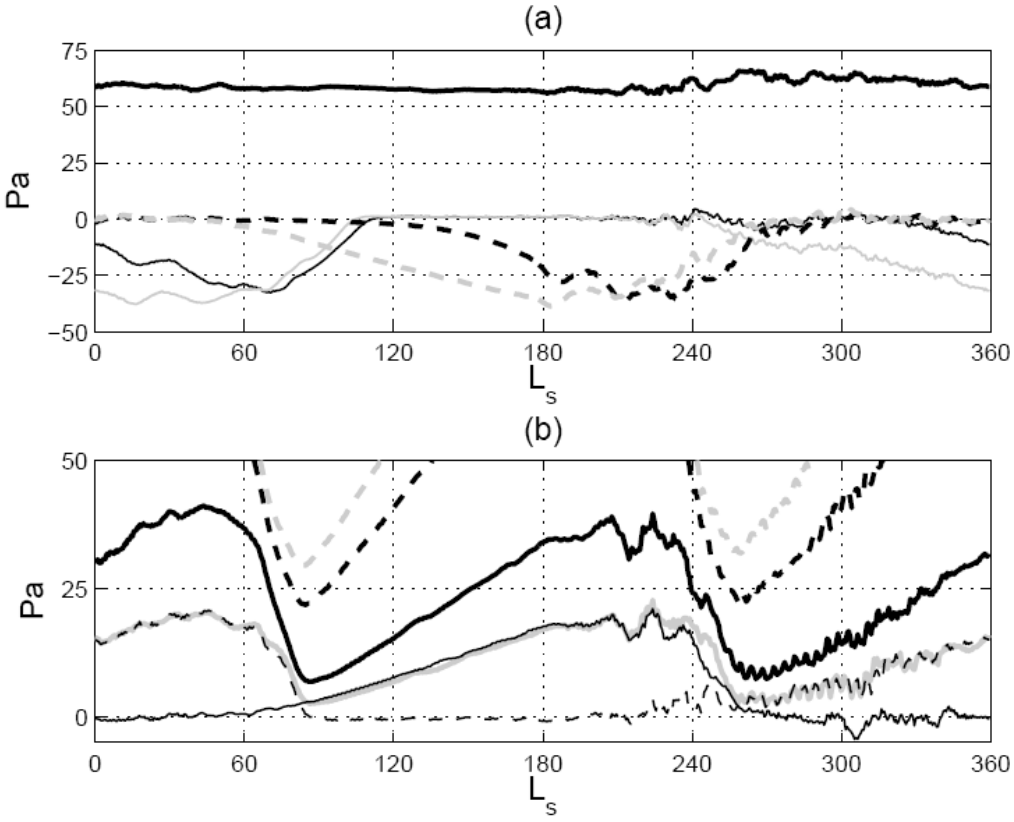

Figure 3.3: Response of MarsWRF surface pressure at VL1 location to positive perturbations. Panel (a): response to perturbation at north seasonal cap albedo (thin black line, $\boldsymbol{P}_1$), north emissivity (thin grey line, $\boldsymbol{P}_2$), south albedo (thick black dash line, $\boldsymbol{P}_3$), south emissivity (thick grey dash line, $\boldsymbol{P}_4$), and total CO_2 mass (thick black line, $\boldsymbol{P}_5$). Panel (b): perturbation to the thermal inertia of the water ice table at the north polar region by 600 J m^{-3} K^{-1} (thin black dash line, $\boldsymbol{P}^e_6$), south by 600 J m^{-3} K^{-1} (black line, $\boldsymbol{P}^e_7$), both by 600 J m^{-3} K^{-1} (thick grey line, $\boldsymbol{P}^e_{\text{extra}}$), both by 1000 J m^{-3} K^{-1} (thick black line), both by 2000 J m^{-3} K^{-1} (thick black dash line), and both by 3000 J m^{-3} K^{-1} (thick grey dash line). The last tow curves only appear partially because of the scale limit.

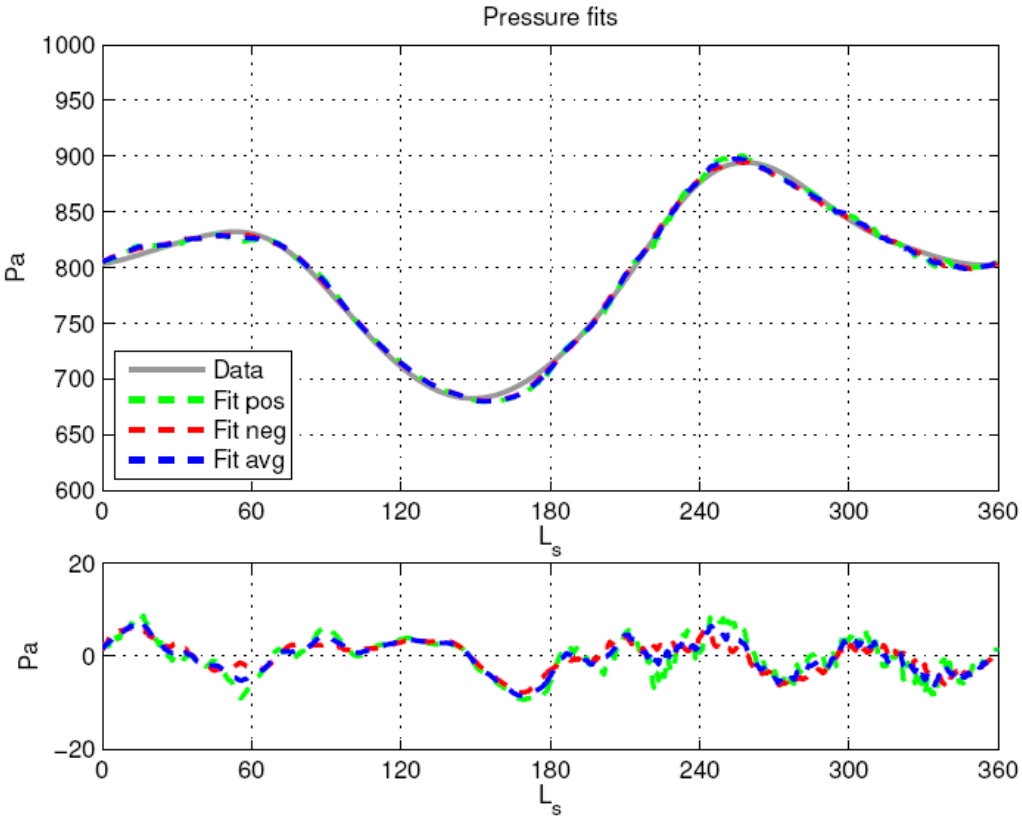

Figure 3.4: Upper panel: the linear fit of surface pressure cycle at VL1 site. Grey line: smoothed VL1 data; green dashed line: linear fit result using positive perturbation matrix $\mathbf{P}^{+}$; red dashed line: linear fit result using negative perturbation matrix $\mathbf{P}^{-}$; blue dashed line: the average of the previous two linear fits. Lower panel: residuals. Green dashed line: residual in the fit using $\mathbf{P}^{+}$; red dashed line: residual in the fit using $\mathbf{P}^{-}$; blue dashed line: the average residual.

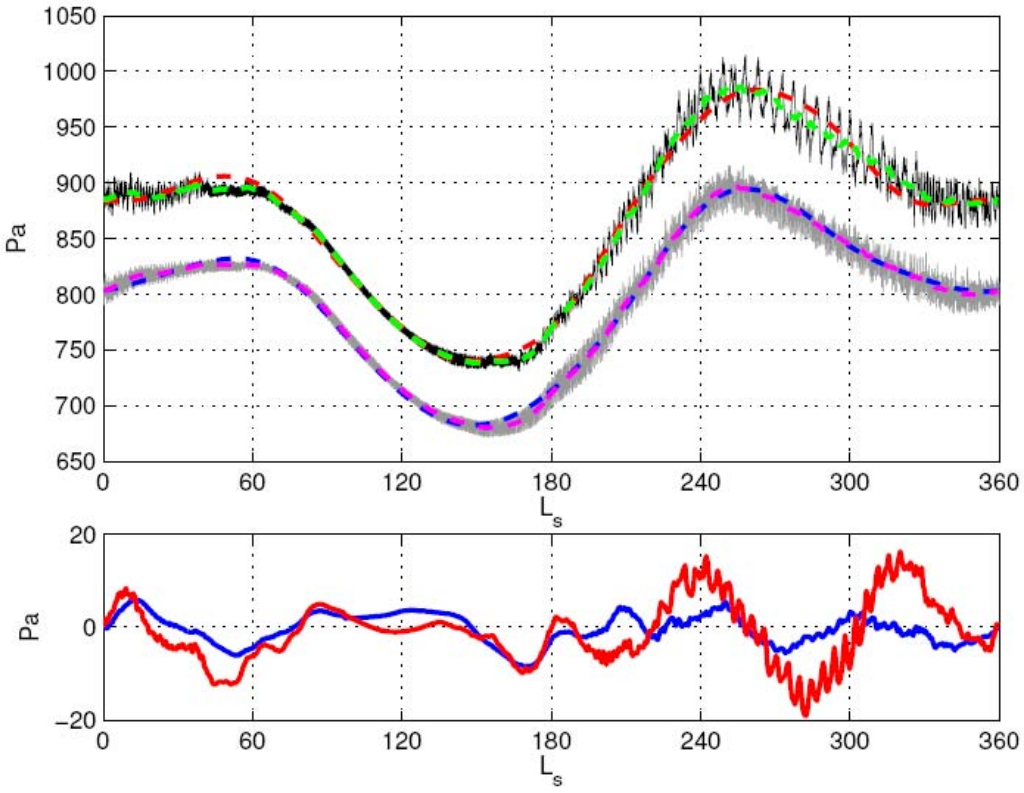

Figure 3.5: Same as Figure 3.1, except MarsWRF outputs are generated using the best-fit parameters (northern seasonal cap albedo: 0.795; northern seasonal cap emissivity: 0.485; south albedo: 0.461; south emissivity: 0.785; total CO_2 mass index: 0.978).

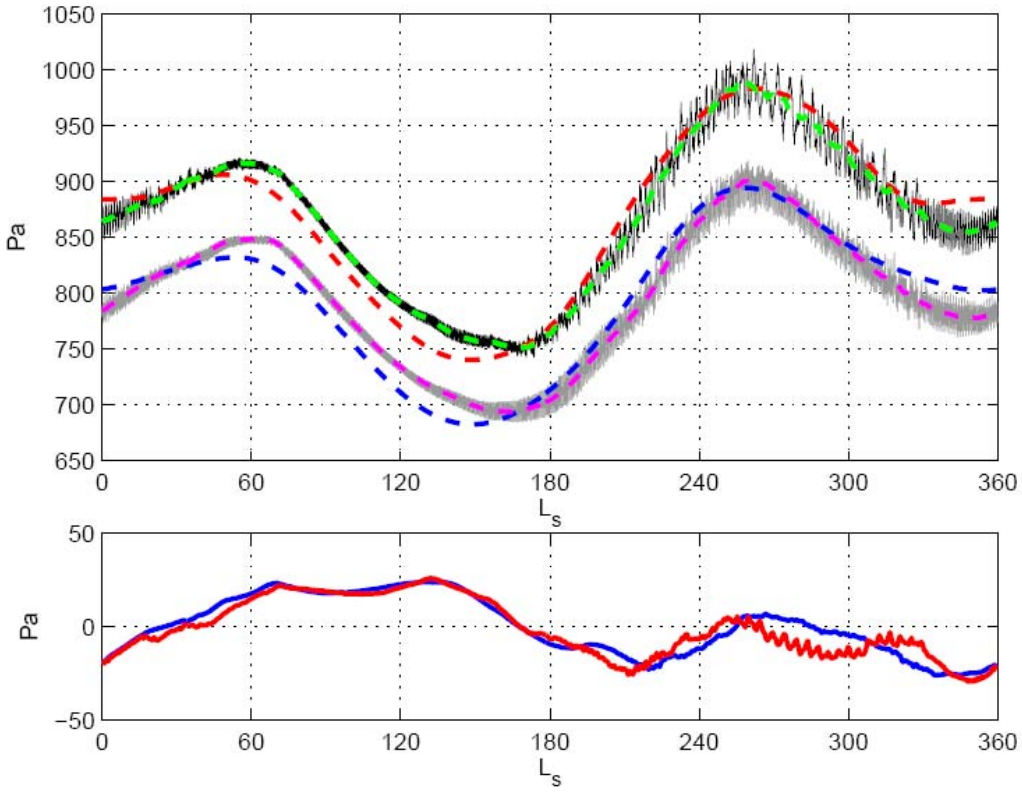

Figure 3.6: Same as Figure 3.1, except fitting parameter are the same as *Haberle et al.* [2008]. Northern seasonal cap albedo: 0.6; northern seasonal cap emissivity: 1.0; south albedo: 0.5; south emissivity: 1.0; total CO_2 mass index: 1.003. Water ice table starts at 8.05 centimeter in the northern hemisphere and 11.16 centimeter in the southern hemisphere. Thermal inertia of ice table is 2200 J m^{-3} K^{-1}.

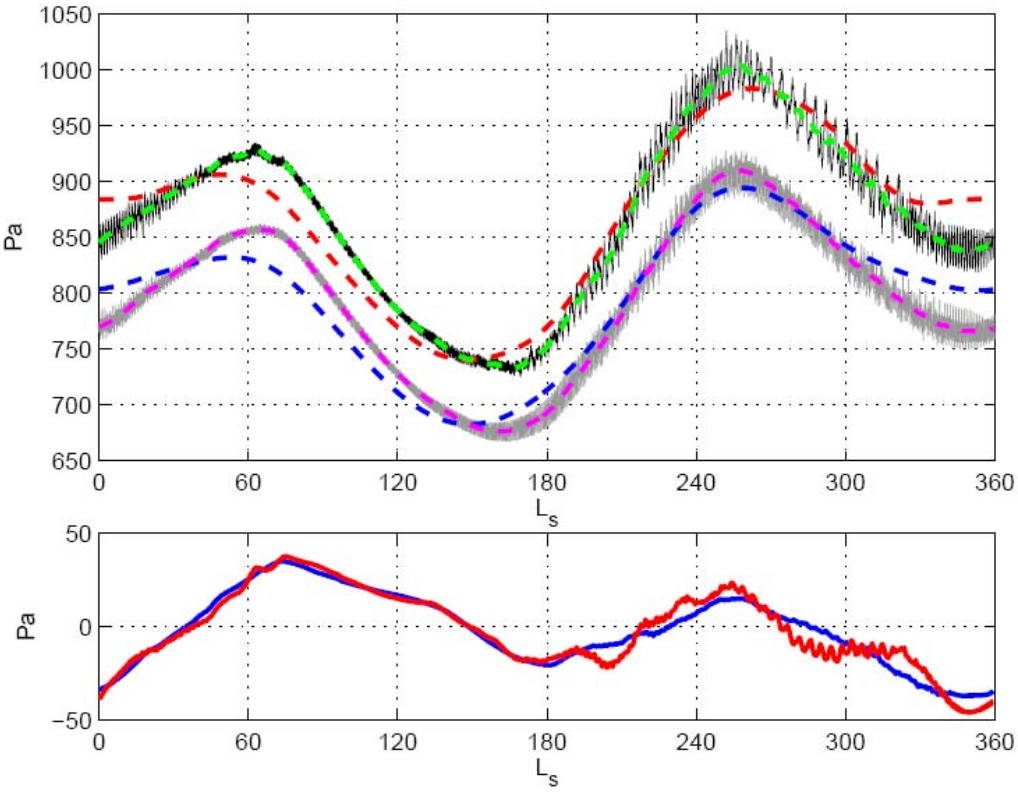

Figure 3.7: Same as Figure 3.1. Except the driving parameters are northern seasonal cap albedo: 0.6; northern seasonal cap emissivity: 1.0; south albedo: 0.5; south emissivity: 1.0; total CO_2 mass index: 1.003; thermal inertia of the ice table is 1800 J m^{-3} K^{-1} in the northern hemisphere and 900 J m^{-3} K^{-1} in the south. Boundary between the dry soil and the water ice table is set to the boundary of permanently stable water ice suggested by *Schorghofer and Aharonson* [2005].

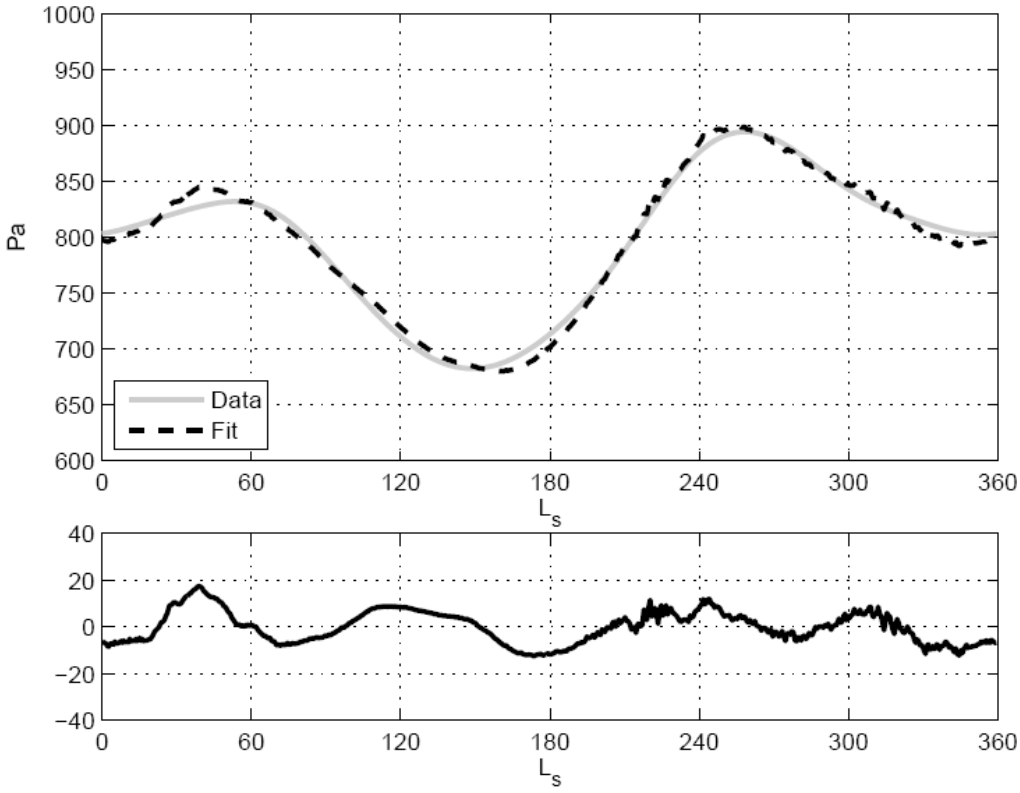

Figure 3.8: Upper panel: polynomial fit to the VL1 pressure cycle (grey line) and the fitted pressure curve (dash line) using albedo of the two seasonal caps, total CO_2 inventory, and the thermal inertia of the water ice table at two different hemispheres. Lower panel: residual (fitted curve minus VL data).

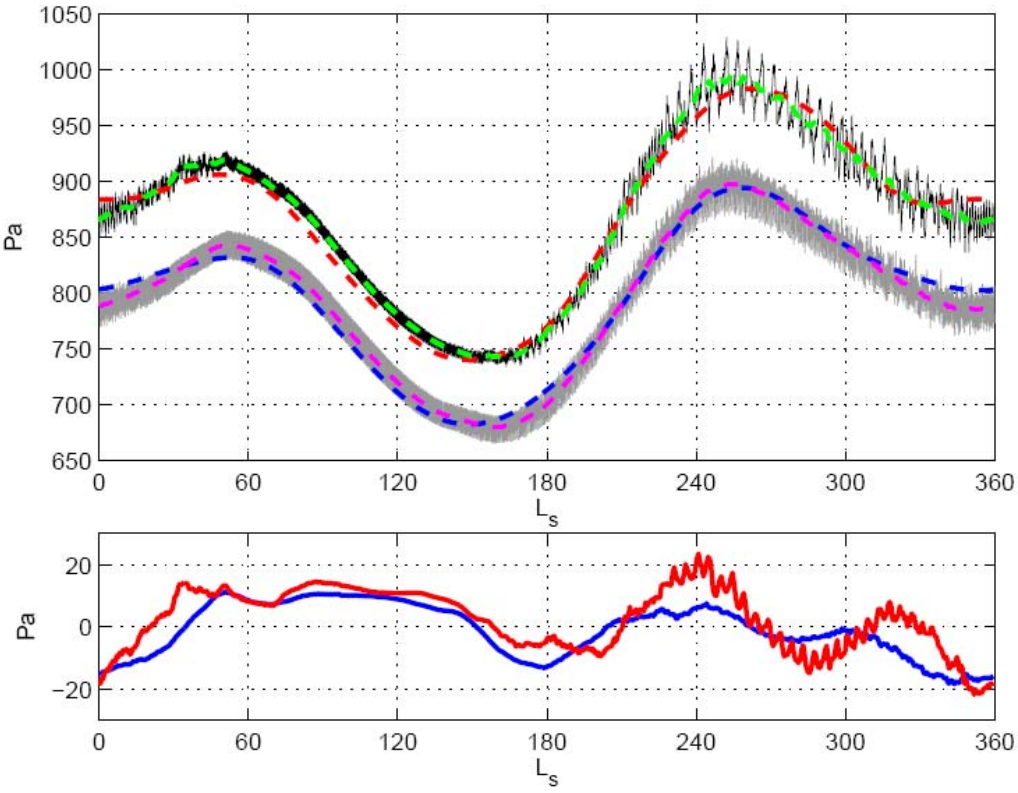

Figure 3.9: Same as Figure 3.7. Except the driving parameters are northern seasonal cap albedo: 0.731; northern seasonal cap emissivity: 1.0; south albedo: 0.546; south emissivity: 1.0; total CO_2 mass index: 1.077; thermal inertia of the ice table is 3900 J m^{-3} K^{-1} in the northern hemisphere and 1800 J m^{-3} K^{-1} in the south.

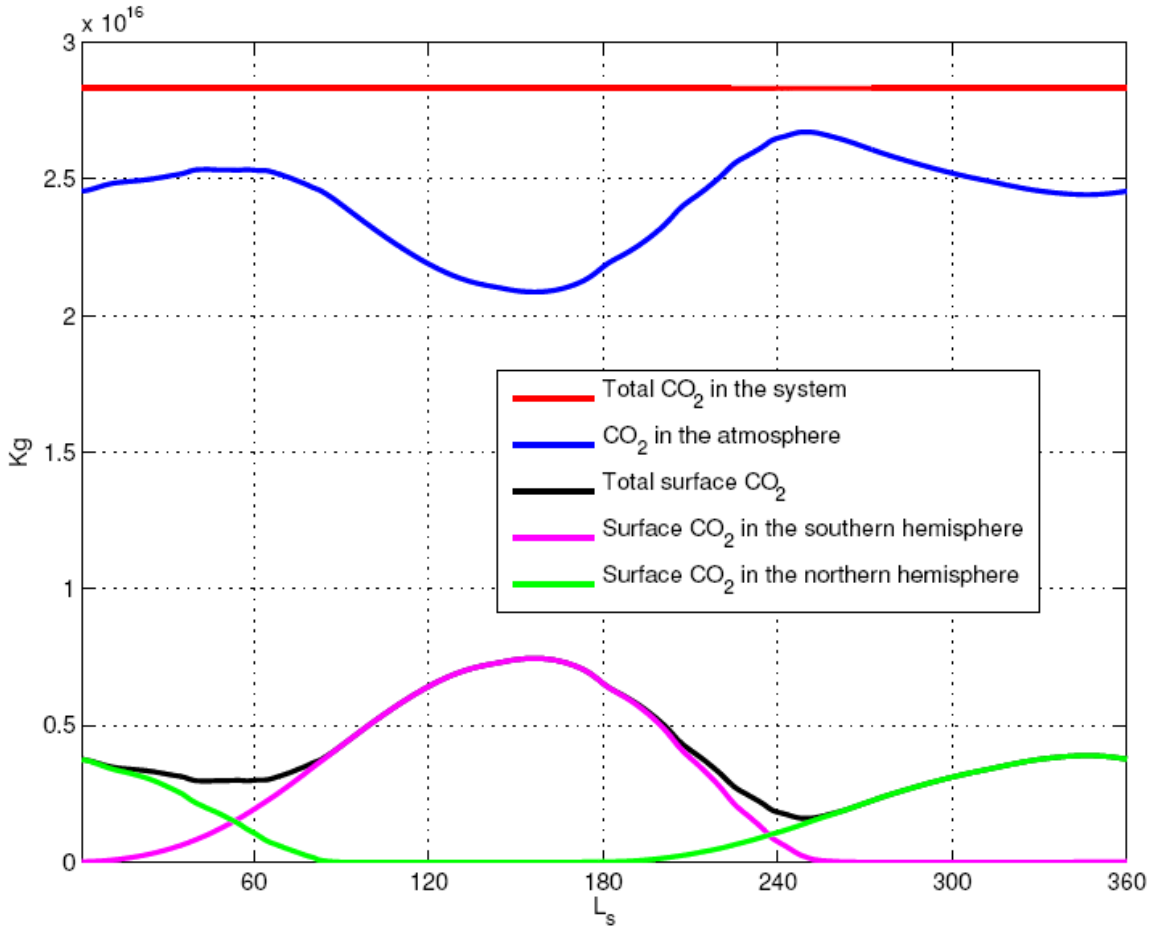

Figure 3.10: CO_2 budget in MarsWRF using the best-fit parameters (northern seasonal cap albedo: 0.795; northern seasonal cap emissivity: 0.485; south albedo: 0.461; south emissivity: 0.785; total CO_2 mass index: 0.978). Red line: total CO_2 in the system, blue line: mass of CO_2 in the atmosphere, black line: mass of CO_2 on the surface, magenta line: surface CO_2 in the southern hemisphere, green line: surface CO_2 in the northern hemisphere.

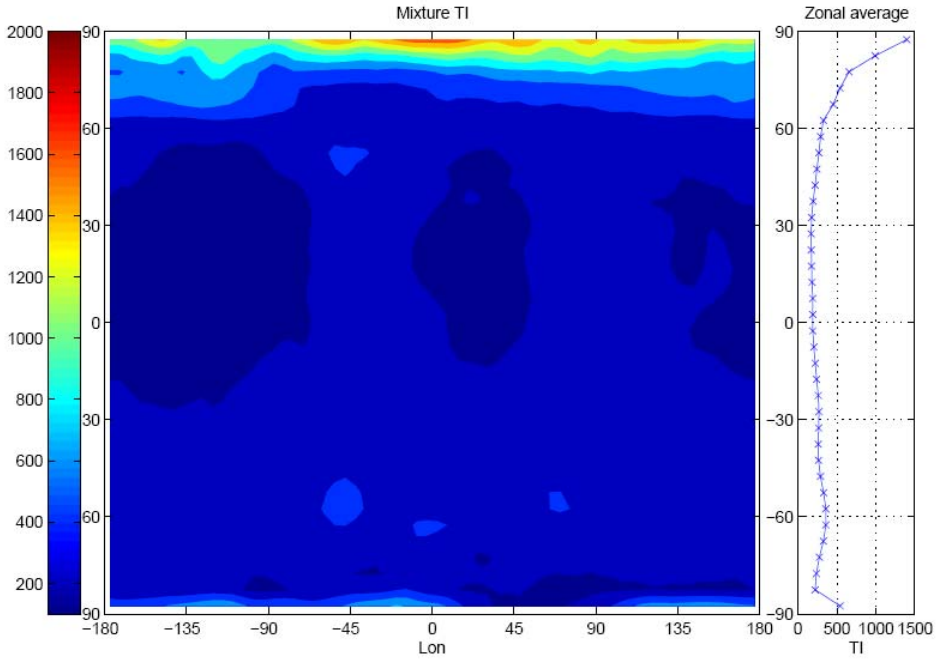

Figure 3.11: Hypothesized subsurface thermal inertia (in J m^{-3} K^{-1}) map and zonal average.

Chapter 4: Modeling the perennial CO_2 ice caps

Abstract

A perennial ice cap has long been observed near the south pole of Mars. The surface of this cap is predominantly composed of carbon dioxide ice. The retention of a CO_2 ice cap results from the surface energy balance of the latent heat, solar radiation, surface emission, and subsurface conduction. While models conventionally treat surface CO_2 ice using time constant ice albedos and emissivities, such an approach fails to predict the existence of a perennial cap. Here we explore the role of insolation-dependent ice albedo, which agrees well with Viking, Mars Global Surveyor, and Mars Express albedo observations. Using a simple parameterization within a General Circulation Model, in which the albedo of CO_2 ice responds linearly to the incident solar insolation, MarsWRF is able to predict the existence of a perennial CO_2 cap at the observed latitude and only in the southern hemisphere. Further experiments with different total CO_2 inventories, planetary obliquities and surface boundary conditions suggests that the location of the residual cap may exchange hemispheres favoring the pole with the highest peak insolation.

4.1 Introduction

Carbon dioxide (CO_2) is the leading gaseous species on Mars, comprising 95% of the atmosphere [*Owen et al.*, 1977]. Throughout a Martian year, up to 30% of the total CO_2 condenses on the surface in winter polar region and forms frost caps [*Kelly et al.*, 2006]. While the discovery of seasonal ice caps at the poles of Mars dates back to the eighteenth century, the existence of a perennial CO_2 ice cap[6] at the south pole of Mars was first discovered by the Viking spacecraft [*Kieffer et al.*, 1977; *Kieffer*, 1979; *Paige et al.*, 1990]. The southern residual cap also contains small amounts of water ice [*Bibring et al.*, 2004].

The annual CO_2 cycle on Mars can be explained by the varying components in the surface energy balance of the caps, including the latent heat exchange, solar radiation, surface emission, atmospheric sensible heat, and subsurface conduction [*Guo et al.*, submitted-a; *Paige*, 1992]. Ideally, General Circulation Models (GCMs) should be able to simultaneously predict the atmospheric budget and the surface budget of CO_2 correctly, e.g. fitting the Viking Lander (VL) pressure cycle while reasonably predicting the CO_2 caps (including seasonal and perennial caps). Indeed, most GCMs are able to fit the atmospheric budget and the seasonal caps reasonably well [*Forget et al.*, 1999; *Guo et al.*, submitted-a; *Haberle et al.*, 2008; *Kelly et al.*, 2006]. However, simulating the residual CO_2 cap remains more challenging because simple energy balance models (and all published GCM results) do not predict its existence; more accurately, the time-invariant albedo and emissivity values preferentially chosen to fit the VL pressure cycles are not able to support a residual CO_2 cap in the southern summer. GCMs understandably give priority to fitting the atmospheric budget

[6] It is also referred as residual cap or permanent cap in the community. In this dissertation, "perennial" and "residual" will be used interchangeably to describe this permanently frozen region.

because of the induced seasonal pole-to-pole flow and because of the influence of total mass variations on other components of the circulation and climate. *Paige and Ingersoll* [1985] suggests that the only reason that the southern residual cap can endure the southern summer is the very high albedo it attains near solstice. These late season southern cap albedos are much higher than those used in GCMs to obtain good fits to the CO_2 cycle, especially for the southern cap.

Wood and Paige [1992] suggested that in order to maintain the southern residual cap a higher albedo or a lower emissivity or both is required. While one finds little evidence supporting the idea that CO_2 ice emissivity is very different from unity, there is abundant evidence that the albedo of the CO_2 ice changes: Viking Orbiter observations suggest that the albedo of the southern residual cap changes with time [*James et al.*, 1992; *Paige and Ingersoll*, 1985]; while the Thermal Emission Spectrometer (TES), Mars Orbiter Laser Altimeter (MOLA), and the Observatoire pour la Minéralogie, l'Eau, les Glaces et l'Activité (OMEGA) also found evidence that the albedo of the seasonal caps evolves [*Byrne et al.*, 2008; *Kieffer et al.*, 2000; *Kieffer and Titus*, 2001; *Schmidt et al.*, 2009]. These changes are of unknown origin, but are possibly related to microphysical processes, such as dust-ice interaction and/or frost grain size evolution with insolation. *Schmidt et al.* [2009] suggest that the CO_2 sublimation in the southern polar cap is mainly controlled by albedo at both global and local scales. More interestingly, the Viking observations suggest that the residual CO_2 cap albedo responds to the incident solar flux in a very linear way. This relationship is likely key to explaining the existence of the perennial cap [*Paige*, 1985].

Given the complete failure of constant albedo models to predict a residual CO_2 ice cap at the south, this study is focused on asking whether the introduction of an insolation-

dependent albedo of CO_2 ice can predict such a cap. The residual cap is largely irrelevant to the current climate insofar as it lacks sufficient mass to consequentially buffer the atmosphere [*Byrne and Ingersoll*, 2003], but this would not have been true at various earlier stages of Martian climate history. Questions relating to the timing of atmospheric collapse for thicker atmospheric states, and the triggering of cap formation at different values of obliquity, orbital parameters, and total CO_2 reservoir will be of consequence for understanding plausible paleo-climatic states. For situations in which the occurrence of residual ice caps is of interest, it would seem that being able to predict a residual CO_2 ice cap for the current climate would be a prerequisite test for any model. We thus undertake an initial exploration of how insolation-dependent albedo influences residual cap development for these parameters.

We perform a systematic study using a Mars GCM, the Mars Weather Research and Forecasting (MarsWRF) model, to explore the possible environments conducive to perennial CO_2 cap formation. We perform simulations with and without incident solar insolation-dependent albedo in order to isolate the effect of varying albedo as observed. We also explore the effects of different total CO_2 inventory, different planetary obliquity and different topographic setups. Section 4.2 provides an introduction to the MarsWRF model and then we present the model results in section 4.3 followed by discussions and conclusions in section 4.4.

4.2 Model description and experiment setup description

In this dissertation, we use the MarsWRF model, the Martian implementation of the planetWRF model [*Richardson et al.*, 2007]. We calibrate the GCM by tuning the albedos and the emissivities of the seasonal dry ice caps and the total CO_2 inventory in the system to reproduce the VL1 surface pressure cycles. At the steady state, the model predicts a pressure cycle that matches the VL records very closely [*Guo et al.*, submitted-a]. The predicted mass of the seasonal caps is consistent with other GCMs and observations [*Kelly et al.*, 2006]. However, like all the other models trying to fit the VL pressure records, a residual CO_2 cap in the south pole is not predicted by MarsWRF with this setup (as a side note, most models include the thermal effects of a residual ice cap by "hard wiring" surface temperature at the south pole to the CO_2 frost point).

The Viking orbiter observations suggests that the albedo of the southern residual CO_2 cap changes with time [*James et al.*, 1992; *Paige and Ingersoll*, 1985]. More usefully, the relationship between the residual CO_2 cap's albedo and the incident solar flux is very linear (Figure 4.1). When a least square linear regression method is applied to this dataset, we obtain an empirical equation that predicts the surface CO_2 frost albedo based on the insolation:

$$A = 0.532 + 8.72\times10^{-4} \times F_s, \qquad (4.1)$$

where A is the albedo of the CO_2 ice cap and F_s is the incident solar flux in W/m^2. This linear model fits the Viking albedo observations for the southern residual cap extremely well, with only several percent of fitting error. In the absence of a proven physical model for the dependence of albedo on insolation or other environmental factors, this empirical relationship

is potentially very important for reproducing a perennial cap in a GCM. Larger albedo creates a larger energy deficit that has to be compensated by more surface CO_2 ice condensation (or less sublimation). Equation 4.1 implies that the albedo is the largest in the summer when the incident solar flux is the most intense, which is ideal for the CO_2 ice to endure the summer.

We incorporate this relationship into MarsWRF. For each time step, if the surface is covered by enough CO_2 ice (for all simulations, a threshold mass coating of CO_2 ice is required in the GCM for modification of the albedo – the value is chosen such that the albedo is changed only when the abundance of CO_2 ice can reasonably be expected to dominate the reflection of sunlight over the scale of a grid cell), we calculate the instantaneous incident solar flux and use Equation 4.1 to determine the surface albedo for the subsequent radiative calculations. We also experimented with different total CO_2 inventories and different obliquities, and also undertook sensitivity studies to determine the influence of topography, thermal inertia distribution, and other factors on the existence and location of the residual cap. Results of model runs are shown in the next session. In all cases, output from the second year of model simulations is shown.

4.3 Model results

4.3.1 "Control case" – constant albedo, current CO_2 inventory and orbital parameters

We first present the control or baseline scenario with time constant albedo. Time constant albedos and emissivities are assigned to the northern and southern CO_2 ice caps. The total CO_2 mass in the system was set to 2.83×10^{16} kg [*Guo et al.*, submitted-a]. As mentioned before, this setup generates a pressure cycle at the VL1 location agreeing with the VL1 records very well (Figure 3.5), but without a residual cap at either pole. The annual variation of the zonally averaged surface CO_2 frost is shown in the panel (a) of Figure 4.2.

4.3.2 Albedo responses to solar insolation

Next we show an experiment in which the surface CO_2 ice albedo is determined from the local incident solar flux according to Equation 4.1 while keeping the rest of the model unchanged (note that albedo of CO_2 ice present at any location on the surface is locally determined via this formula). We show the corresponding CO_2 ice surface deposition annual cycle in the panel (b) of Figure 4.2.

Following the seasonal cap evolution, starting with the onset of polar night in each hemisphere, CO_2 begins to deposit at the winter poles. At this time of the year, the season cap areal coverage in both hemispheres does not differ greatly in the time-varying albedo experiment compared to the control case. This is expected because during the polar nights the surface albedo is not relevant to the surface energy balance. When the surface frost is

exposed to the sun, the abundance and the longevity of the surface CO_2 ice starts to differ from the control case. In the northern hemisphere, the albedo determined by Equation 4.1 is usually comparable or slightly smaller than the value used in the control case. As a result, the CO_2 ice in the north in the varying albedo case sublimates at the same rate or slightly faster than in the control case. More dramatic change can be found in the southern hemisphere. As the southern seasonal ice cap is exposed to sunlight as the spring wears on, the albedo is driven to higher values than in the north, and to higher values than those used in the south in the control simulation. This brightening of the southern cap leads to less solar energy absorption and thus reduces the cap sublimation rate. Indeed, thanks to the high albedos generated by Equation 4.1, the CO_2 ice at the southern pole is able to endure the summer and forms a perennial reservoir.

The reason for the existence of perennial CO_2 ice in the GCM is consistent with the *Paige and Ingersoll* [1985] study of the heat balance of the residual cap. The perennial ice reservoir produced by the GCM is slightly displaced from the geographical south pole, and is longitudinally asymmetric, agreeing with observations [*Colaprete et al.*, 2005; *Kieffer et al.*, 1977]. However, while the observed southern residual cap is confined in the area between 84° S and 90° S, tilted towards 300° E longitude, our simulation has only one gird point representing the residual cap centered at 81.2° S and 73° E (Figure 4.3). Although the latitude and the area of the perennial caps in the simulation are similar to the observation, the longitudinal distribution is not. We will further discuss this asymmetry in later sections.

It should be noted that the use of Equation 4.1 to determine albedo for any and all CO_2 surface ice deposits introduces an error into the fitting of the VL pressure curves. Equation 4.1 was defined only for the area of the residual cap, and its applicability to the

whole planet is questionable [*Kieffer and Titus*, 2001]. Indeed it seems that geology and the history of the nature of the ice deposition (whether direct surface deposition or snowfall) influence the geographical distribution of the albedo-insolation relationship. For example, we could limit the application of Equation 4.1 between 85° S and 90° S and fix the rest of the values to those used in the controlled case. Because the mass in the residual cap is relatively small, it has little or no impact in the surface pressure, which is a measure of the total atmospheric mass. However, given the initial nature of this study, and the lack of a physical model for the geographical distribution of the albedo-insolation relationship, we think it is clearer here to explore the consequences of a simple, consistent relationship and to focus primarily on the ability of such a relationship to predict residual cap formation.

4.3.3 Varying CO_2 inventories with insolation-independent albedo

Using the time-constant (insolation independent) albedo and emissivity values of the frost caps from the control simulation, we experiment with different total CO_2 inventories. We vary the total mass from a third to 100 times of the current amount. Associated surface CO_2 ice annual cycles are shown in Figure 4.4.

The frost coverage patterns wax and wane from one experiment to another: while the latitudinal coverage does not change much, the surface ice densities increase then decrease as the total CO_2 inventory increases, as do the durations of the frost covering period in both hemispheres. These variations are caused by two competing processes. First, increasing the totally CO_2 inventory increases the (partial) pressure of CO_2 gas in the atmosphere. In response, the critical temperature for CO_2 condensation goes up (black solid line in Figure

4.6), which makes it easier for CO_2 to condense and persist as ice. Second, the enhanced greenhouse effect due to a denser atmosphere makes the planet warmer (grey line with diamonds in Figure 4.6), which tends to reduce CO_2 condensation (and speed sublimation). Therefore, when the first mechanism is dominating, adding to the total CO_2 inventory helps the formation of CO_2 frost in the winter (notice the increasing trend in the frost deposition from panel (1) to (5) of Figure 4.4). On the other hand, when the second mechanism is dominating, increasing the total CO_2 inventory reduces the formation of frost. The CO_2 surface frost amount decreases from panel (5) to (8) of Figure 4.4 and completely disappears in both hemispheres when 100 times the current mass is used in the system (not shown in Figure 4.4). The transition CO_2 amount separating these two regimes seems to be around 10 times the current inventory. Finally, we notice that none of these experiments predicts a perennial CO_2 ice cap.

4.3.4 Varying CO_2 inventories with insolation-dependent albedo

We perform another set of experiments by combining the two modifications to MarsWRF described above. We change the CO_2 inventory while letting the CO_2 cap albedos response to the incident solar flux following Equation 4.1. The corresponding surface CO_2 ice annual variations are shown in Figure 4.5.

Akin with the results found in Section 3.3, the latitudinal coverage of the CO_2 frost does not change much. In general, for the same reasons, the frost deposition responds to the total CO_2 inventory similarly to what was described above. More interesting differences are notable in the southern high latitudes. In the middle of the sequence of experiments, the CO_2

ice coverage is much greater and longevity extended during southern summer. One can find a series of experiments that predict CO_2 ice persisting throughout years (panels (2), (3), (4), and (5) of Figure 4.5). Some experiments with higher inventory predict perennial caps in even lower latitudes (panels (3), (4), and (5) of Figure 4.5). Again, the perennial CO_2 ice caps turn seasonal, and even completely absent, if enough CO_2 gas is added to the system, due to the greenhouse effect of the CO_2.

These simulations suggest that the time varying albedo is the decisive factor in predicting the perennial cap. Although the increase of CO_2 critical temperature due to higher (partial) pressure helps the frost last longer in the spring and early summer, the environment is just not in sufficient energy deficit for the CO_2 ice to endure the entire summer with the kind of insolation or time invariant albedo values typically used in models (see Figure 4.4). The enhanced albedos in the southern hemisphere create the energy deficits required by the perennial CO_2 frost, which is clearly demonstrated in Figure 4.6. Compared to the time-constant frost albedo (grey line with diamonds in Figure 4.6), the insolation-dependent albedo system has the effect of reducing near surface temperature significantly as runs with successively more CO_2 are examined (black line with crosses in Figure 4.6). Eventually, the enhanced greenhouse effect overwhelms all other effects in the system and reduces and then prevents CO_2 ice cap formation (terminating them when roughly 100 times current inventory is used). It is very interesting to notice that the current Martian atmospheric mass is just large enough to maintain one southern residual cap at its current latitude.

4.3.5 Influence of obliquity on residual cap formation and location

The secular perturbations due to all other planets in the Solar System causes the orbit of Mars to change chaotically [*Laskar*, 1990]. Different orbital parameters, including spin axis obliquity and eccentricity result in different patterns of surface insolation [*Laskar et al.*, 2002], which modifies the CO_2 cycle by its direct impact on the surface energy balance. We experiment with different obliquity values assuming this change would not cause any other surface properties to vary. We hold the eccentricity of the Martian orbit constant in these experiments. Corresponding surface CO_2 ice annual variations are shown in Figure 4.7.

The column of panels on the left hand side of Figure 4.7 shows the CO_2 ice cycles from simulations assuming the control case time-constant (insolation-independent) albedo. For low obliquity simulations, the lack of incoming solar energy in the summer makes the polar region ideal for the CO_2 ice to persist through the local summer. For example, in the simulation with 10° obliquity (panel (1) of Figure 4.7), permanent caps form at both poles. As the obliquity increases, seasonal CO_2 frost advances to lower latitudes as the location of the maximum reach of polar night extends equator-ward. On the other hand, summer insolation becomes larger. Stronger sublimation reduces the amount and longevity of CO_2 frost, and eventually eliminates the perennial cap (panels (3), (5), and (7) of Figure 4.7). Again, the prediction from this class of models is that current Mars does not correspond to a state with a perennial CO_2 cap at either pole.

If we assume the frost albedo responses to the solar insolation according to Equation 4.1, the surface CO_2 ice cycles behaves differently, as shown by the column on the right hand side in Figure 4.7. At low obliquity, we also find perennial CO_2 ice caps in both hemispheres for the same reasons described above. As the obliquity increases, the effects of higher

insolation and higher albedo start to compete in the summer. Although slowly, summer CO_2 ice retreats in the southern polar region with increasing obliquity and reaches a minimum at an obliquity of 30° (panel (6) of Figure 4.7). However, further increase of obliquity helps the albedo effect to gain dominance. At an obliquity of 45°, the summertime CO_2 ice is more extensive and thicker than at 35° (panel (8) of Figure 4.7). The comparison between these two sets of experiments supports our argument that the response of the frost albedo to the solar insolation is crucial to predicting the permanent CO_2 ice cap. Further, the insolation dependence may guarantee that the south would possess a residual CO_2 cap regardless of the obliquity if all other factors remained fixed (inventory, eccentricity, etc.)

4.3.6 The asymmetric location of the residual cap

Paige and Ingersoll [1985] and *James et el.* [1992] hypothesized that the time-varying and relatively high albedo of the southern residual cap must be related to an ice-microphysical processes. However, geographical variations in the behavior were hard to explain without an understanding of what might cause geographical variations in the microphysical processes (or initial conditions). *Colaprete et al.* [2005] suggested that the skewed location of the perennial cap is due to the asymmetry in air temperatures during the formation of the ice cap, which is a consequence of the asymmetric atmospheric dynamics driven by the topography. They showed that the longitudinal climate asymmetry vanishes as Tharsis, Hellas and Agyre are removed from the model. The longitudinal variations in air temperature map to differences in the fraction of surface CO_2 ice formed by direct deposition versus snowfall. While the model simulations shown by *Colaprete et al.* [2005] did not

include any surface ice microphysics related to the deposition, the idea provides a solid concept of how microphysical evolution may vary geographically (in this case because small particles deposited as snow may evolve very differently from sheet ice deposited directly at the surface). *Schmidt et al.* [2009] also suggested that the asymmetry of the southern seasonal polar cap recession around the geographic south pole is only due to the albedo asymmetry.

Assuming the CO_2 frost albedo responds to the solar insolation according to Equation 4.1, our model predicts a residual cap that is not symmetric in the longitudinal direction. Further simulations with MarsWRF show that surface boundary conditions, such as thermal inertia, surface slopes and soil temperature, have very limited, if any, effects on the location of the perennial cap. On the other hand, changing the total CO_2 inventory, or the obliquity of the planet results in migration of the location of the southern perennial cap (Figure 4.8 and 4.9). It is not clear why the location is sensitive to the inventory and obliquity, but changes in the spatial distribution of the surface energy balance resulting directly from these changes or indirectly via changes in the atmospheric circulation and its influence on the surface energy balance may be responsible. When we use the zonal averaged topography in MarsWRF, a zonally symmetric residual cap can be found at the south pole (see Figure 4.10). This is consistent with previous works, which suggest the most important boundary condition that forces the circulation structure is the topography [*Colaprete et al.*, 2005; *Richardson and Wilson*, 2002a]. Mild asymmetry can still be found in the CO_2 ice distribution. It suggests that wave activity is also contributing, but those issues are beyond the scope of this dissertation. Nevertheless, the experiments above assert that the relationship between the perennial cap and the dynamic structure is very intimate, probably more so than with the surface properties.

4.3.7 The influence of other surface properties

An important aspect of the current Martian climate system is that the CO_2 perennial cap dwells at the south pole. While the control case predicts no residual cap at all, a perennial cap is generated only for the south (panel (b) of Figure 4.2) if we include the insolation-dependent albedo. However, there are issues with the control case that require some further investigation.

There is a concern that the control case may bias against a northern cap because we used a relatively low emissivity (0.485) for this cap (although in reality, this low emissivity is merely aliasing the effects of subsurface heat transport associated with neglected subsurface water ice, and that the resulting modeled surface energy balance – which is all that really matters here – is in fact rather close to that which obtains on Mars [*Guo et al.*, submitted-a]). In any case, low emissivity reduces the energy that the cap gives away, therefore reduces the CO_2 condensation in winter and increases its sublimation in summer. We consequently performed a simulation in which we matched the northern CO_2 ice emissivity with that of the south (0.785). The resulting surface CO_2 ice cycle is shown in the panel (a) of Figure 4.11. As expected, the northern cap now contains more CO_2 ice with longer life time. However, the increase of northern cap emissivity does not have sufficient impact as to turn the northern seasonal cap into a perennial cap. Combined with the fact that we believe the low northern cap emissivity actually better represents the northern cap energy budget, these results suggest that a low northern cap emissivity is not responsible for the failure of the control case to generate a northern residual CO_2 ice cap.

The thermal conductivity of the northern regolith may be higher than the south, which gives disadvantage to the northern hemisphere in retaining surface CO_2 ice [*Guo et al.*,

submitted-a; *Haberle et al.*, 2008; *Putzig et al.*, 2005]. In order to test the importance of the subsurface conductive heat, we performed an experiment in which we applied the global average regolith thermal conductivity at all locations (emissivities for CO_2 ice in both hemispheres were still set to 0.785). The corresponding surface CO_2 ice cycle is shown in the panel (b) of Figure 4.11. Little change can be found between panels (a) and (b). The north polar regolith in the control case has a relatively large thermal conductivity. Reducing the thermal conductivity increases the amount of CO_2 ice, but only slightly. The decrease of ice abundance in the southern summer is barely discernable, where the thermal conductivity is slightly raised. It suggests that for this magnitude of change, the subsurface heat conduction plays a less important role in the surface energy balance.

4.3.8 The influence of argument of perihelion and eccentricity

The current eccentricity of the orbit of Mars is relatively large (0.093), and given the timing of perihelion near the southern summer solstice, the insolation received in the two polar regions during their respective summers is very different. In the southern summer near the south pole, the insolation is up to 45% larger than that in the northern summer near the north pole. Such change projects to a difference of up to 0.2 in the insolation-dependent albedo using Equation 4.1. This seems to be the decisive factor in explaining why the residual cap is located in the south. To examine this argument, we first setup a simulation in which the CO_2 ice albedo changes with insolation according to Equation 4.1, the ice emissivity is fixed to 0.8, and the regolith thermal conductivity is set to the global average. When modeled with the current orbit of Mars, the resulting surface ice cycle is shown in

panel (c) of Figure 4.11. The pattern is very similar to what is shown in panels (a) and (b). We then perform another experiment, which has the same setup except that the timing of perihelion and aphelion are swapped by 180 degrees relative to the present. Corresponding CO_2 ice annual variation is shown in panel (d) of Figure 4.11. Now the northern polar region experiences much stronger insolation during its summer than does the south. As a result of Equation 4.1, the northern cap yields higher ice albedo, and as a result a perennial cap is formed in the north. The situation for the southern polar region is exactly the opposite, causing the perennial ice to vanish in the southern summer. As a result, we are left with the rather counter-intuitive result that the extremely volatile CO_2 ice more readily survives at the pole experiencing the more intense solsticial sun light.

One implication of our results is that if the CO_2 ice albedo follows the relationship indicated by Equation 4.1, the existence of a perennial cap near the south pole is primarily dependent on the current orbit of Mars. If the orbit were different, and specifically the argument of perihelion, the pattern of the insolation annual variation will be different, and the residual ice cap may switch to the opposite hemisphere. Interestingly, the physics of this control are opposite to those that control the location of the residual water ice cap. For CO_2 stability, maximizing peak insolation is critical, whilst for water, it is minimizing insolation that is key [*Jakosky*, 1983a; b; *Richardson and Wilson*, 2002b]. As a result, we would expect water and CO_2 residual ice caps to swap hemispheres as the argument of perihelion progresses.

4.4 Conclusions and discussions

Viking orbiter data suggests an empirical linear relationship between the CO_2 ice cap albedo and the incident solar flux. When we include this relationship in MarsWRF, a GCM specifically design for the study of the Martian atmosphere, we are able to reproduce a CO_2 cap that persists throughout the full year near the south pole. This perennial cap is not located exactly at the geographical south pole, nor is it zonally symmetric, which agrees with the observations. On the other hand, the predicted perennial cap is not at the same longitude as seen in the observations.

As the atmospheric mass in the model initially increases, the condensation temperature for CO_2 increases, which makes it easier for CO_2 to condense and persist. However, the enhanced greenhouse effect introduced by the increase of the total atmospheric mass will ultimately outpace the increase of CO_2 critical temperature and eventually prevents the presence of CO_2 frost in the summer (and eventually even in the winter). With increased CO_2 inventory, we still need the frost albedo responding to the sunlight as described by Equation 4.1 in order to create an energy deficit required sufficiently large to form a perennial CO_2 ice cap. From our simulations, it is interesting to note that if the relationship between the surface CO_2 ice albedo and the incident solar flux holds, the current Martian atmospheric mass may be just large enough to maintain the southern residual cap at its current latitude. Obliquity is an important factor for determining the extents of the seasonal ice caps, but does not result in a residual southern cap until obliquity falls below roughly 15 degrees, in agreement with prior studies [*Newman et al.*, 2005].

Similar to other GCM studies of the perennial cap, none of our simulations were able to replicate the longitudinal location of the perennial cap asymmetry, as seen in the Viking observations. However, we do not include any spatial variation in the insolation-dependence of albedo that may result from the distribution of snowfall versus direct surface deposited CO_2 ice [*Colaprete et al.*, 2005]. A "complete" model of the CO_2 ice caps, seasonal and perennial, will have to combine both the time varying and spatially varying nature of the albedo, hopefully within the context of a physically-based model of the CO_2 ice cap microphysics.

Given the insolation dependence of CO_2 ice albedo, the existence of a permanent CO_2 ice cap at the south is related directly to the occurrence of peak insolation during southern summer rather than northern summer. It also requires the albedo-insolation function to increase the albedo sufficiently quickly with insolation that $F_s(1 - a)$ decreases as F_s increases (where F_s is the insolation and a the albedo). An important consequence of this function is a prediction that the residual CO_2 ice cap will switch hemispheres as the argument of perihelion progresses and alternately results in peak insolation in the north and the south. Interestingly, the CO_2 residual ice cap will be driven to the pole with highest peak insolation, while prior work on the Martian water cycle suggests that the residual water cap will always migrate to the pole with minimum peak summer insolation [*Richardson and Wilson*, 2002b]. Thus Mars may remain with a very similar configuration of poles as we see it today (with just one CO_2 ice residual cap and one water ice residual cap), albeit periodically turned on its head as the perihelion timing changes.

Various spacecraft data, including Viking, MOC, TES, MOLA and OMEGA, provide evidence for this monotonically increasing relationship between the albedo of CO_2 ice cap

and the insolation. Regardless of the details of the slope or shape of the albedo-insolation function, the fact that the albedo is an increasing function of the insolation is the key in explaining the existence of the perennial CO_2 ice cap and the cap's preferential dwelling at the pole with higher peak insolation.

Figures

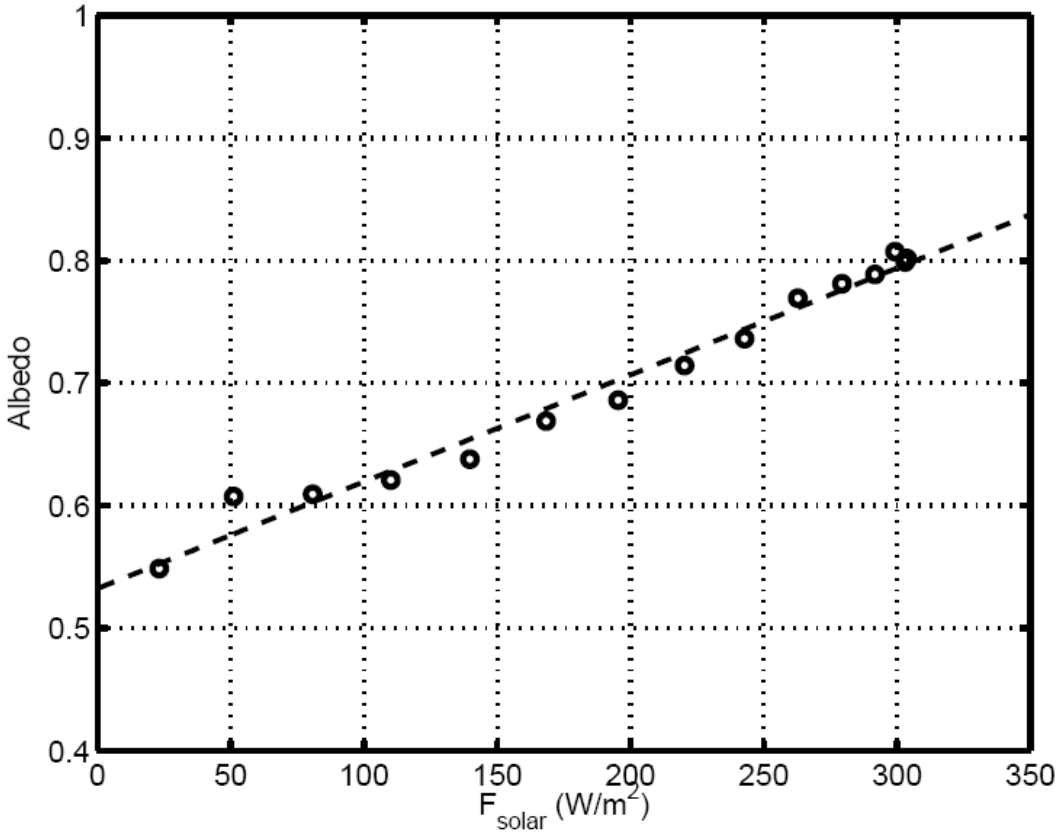

Figure 4.1: Southern residual cap albedo as a function of incident solar insolation. Open circles: observations from the Viking spacecraft; dashed line: the line from the linear fitting of the Viking data (Equation 4.1).

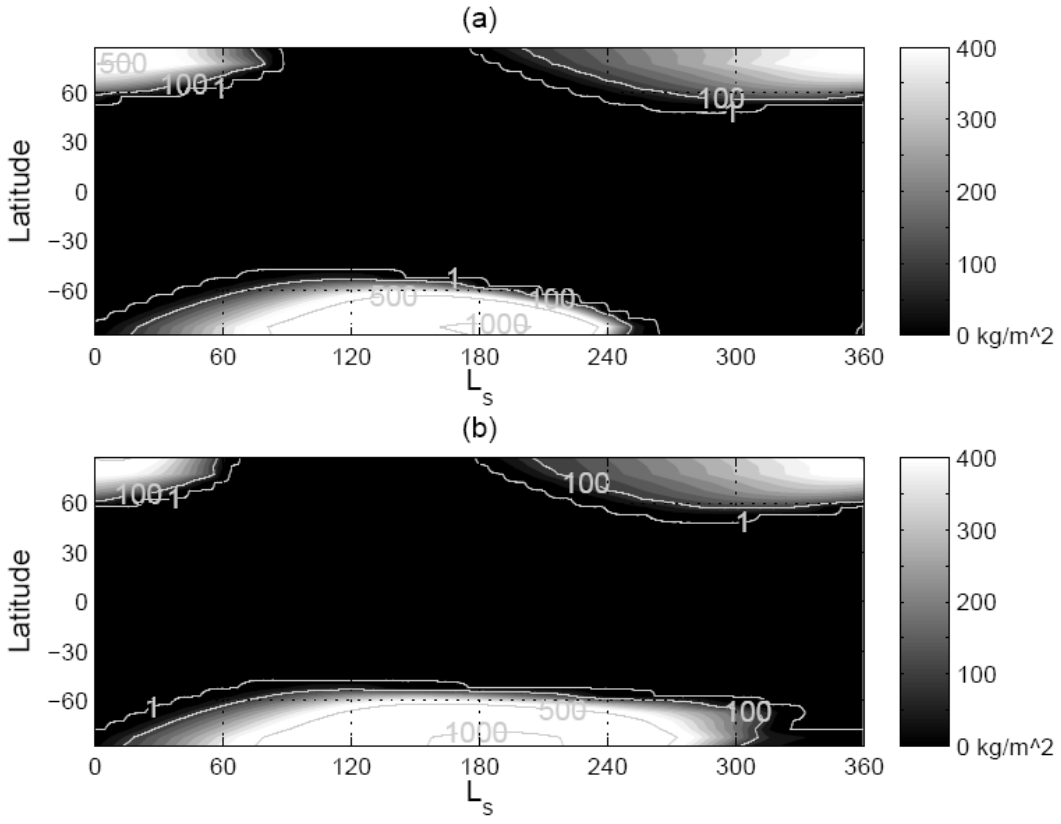

Figure 4.2: Annual variation of zonally averaged surface CO_2 ice deposition. The grey scale indicates the density of the deposition in kg/m^2. From the lower latitudes to the polar region, the grey contour lines indicate the deposition levels of 1 kg/m^2, 100 kg/m^2, 500 kg/m^2 and 1000 kg/m^2 respectively. Panel (a): the calibrated case, with time-constant CO_2 frost albedos and emissivities, the CO_2 inventory of the system is 2.83×10^{16} kg; panel (b): The setting of this experiment is identical to that of panel (a), except the frost albedo is calculated using Equation 4.1 in each time step.

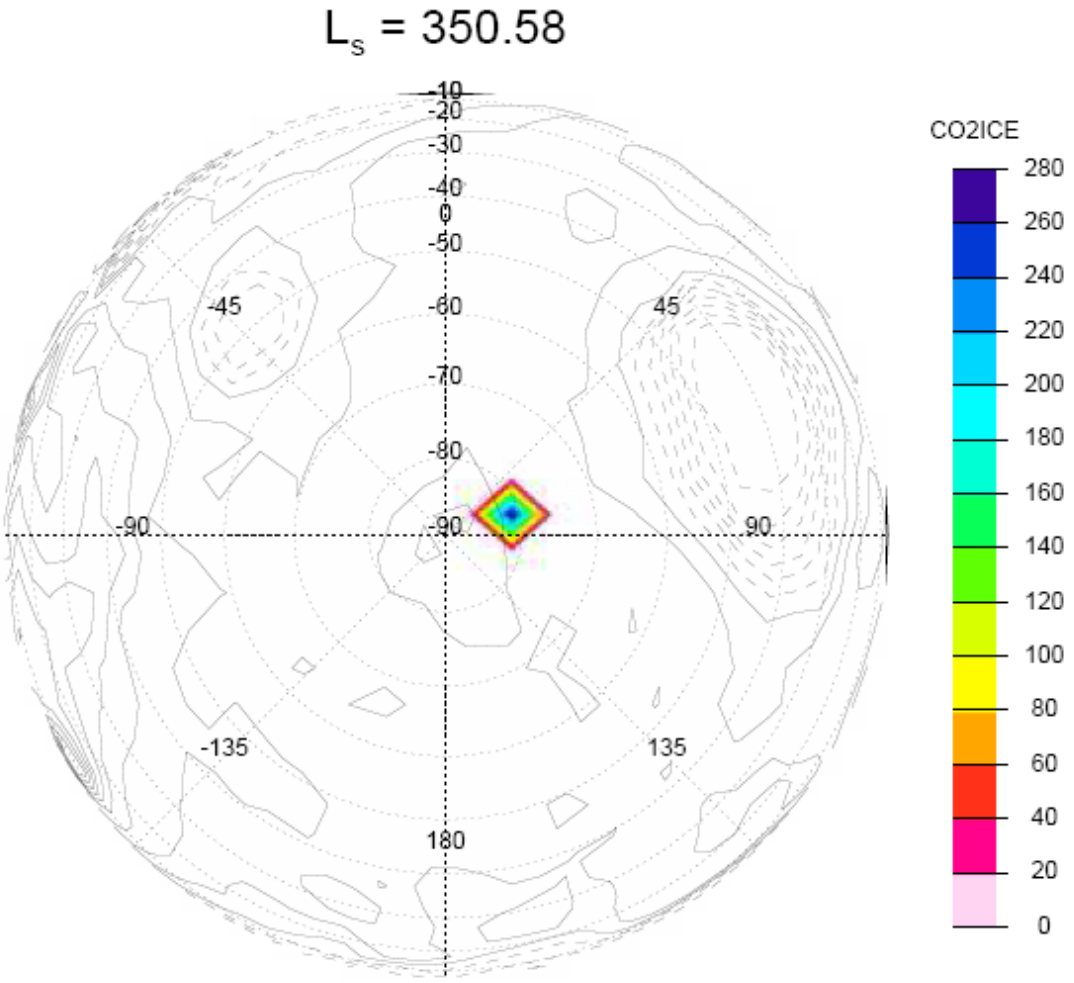

Figure 4.3: A snap shot of the southern hemisphere at Ls 350.58°. Color map represents the surface CO_2 ice abundance in kg/m^2. Black contours indicate the Mars Orbiter Laser Altimeter topography data embedded in MarsWRF, with solid contours indicating positive values and dashed contours indicating negative values.

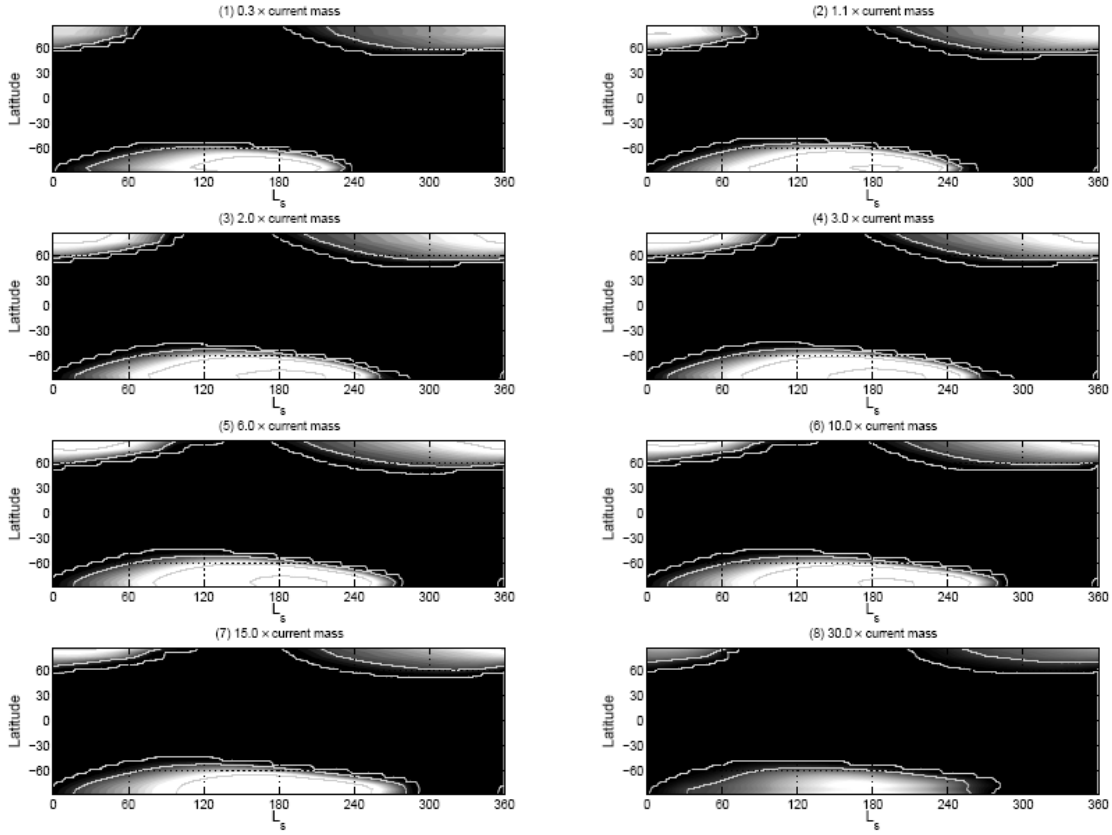

Figure 4.4: Same as Figure 4.2. Each panel corresponds to a different experiment with different total CO_2 inventory. For these experiments, the frost albedos and emissivities are time-constant and fixed to the values used in the calibrated case (albedo of the northern cap = 0.795, emissivity of the northern cap = 0.485, albedo of the southern cap = 0.461, emissivity of the southern cap = 0.785).

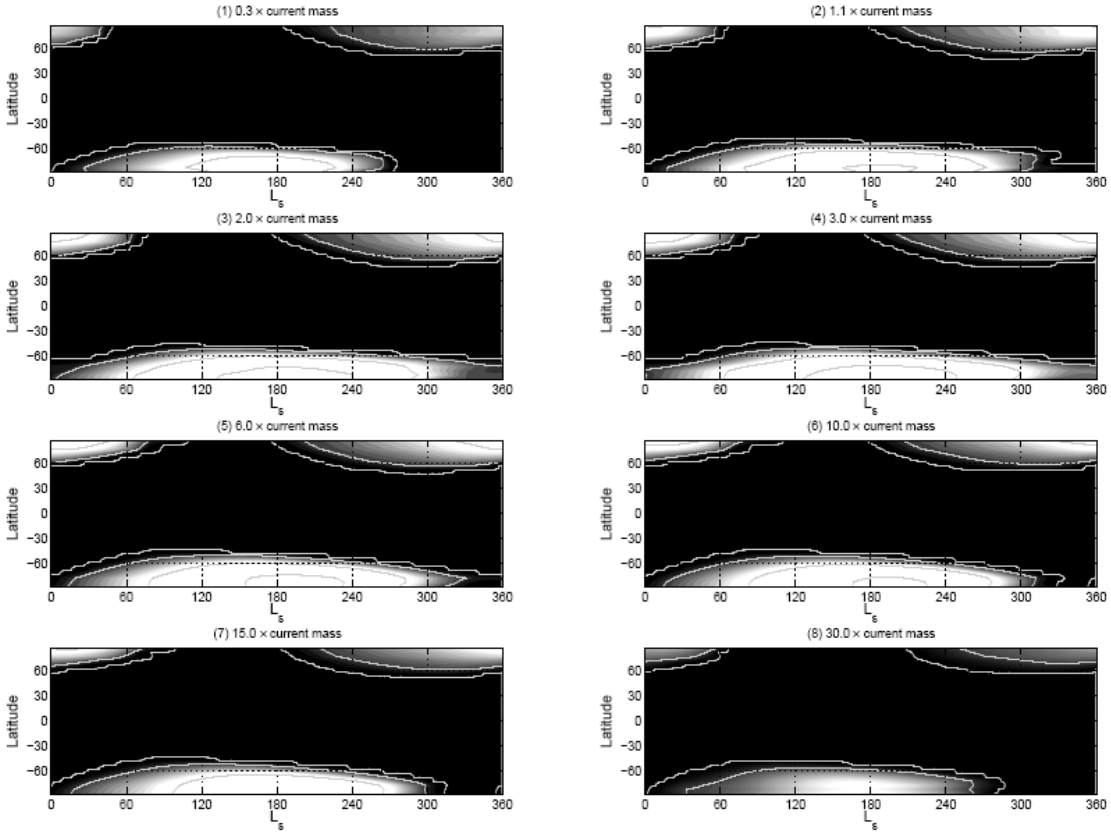

Figure 4.5: Same as Figure 4.4, except the CO_2 frost albedos insolation-dependent according to Equation 4.1.

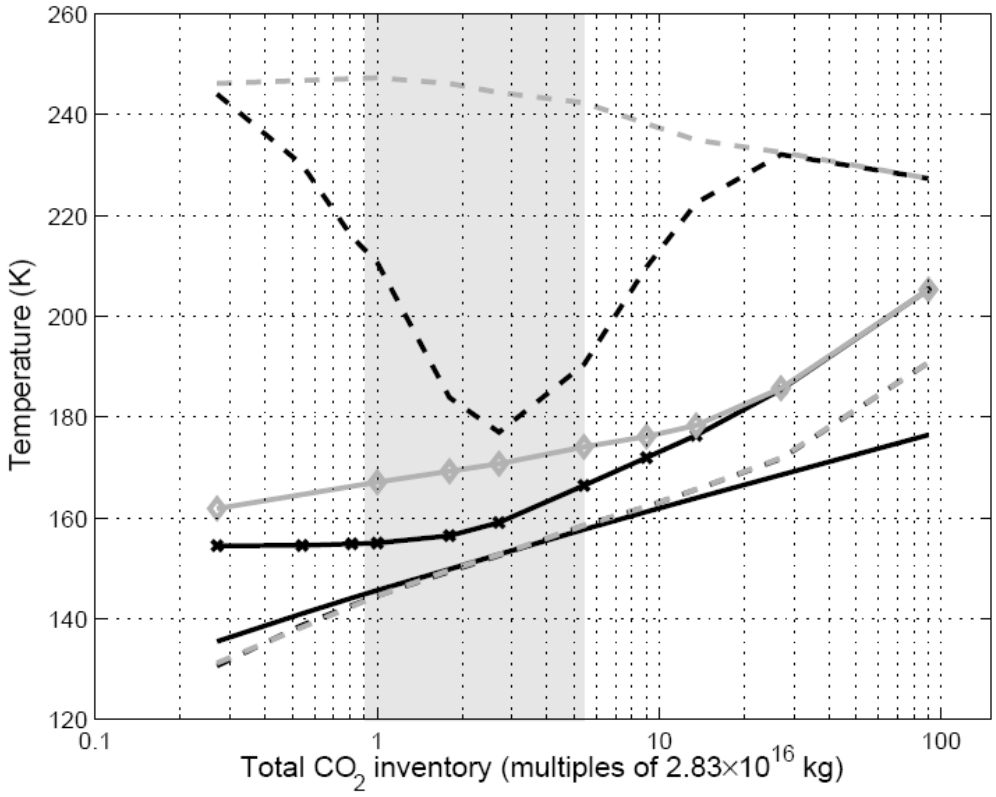

Figure 4.6: Annual near-surface atmospheric temperature variations near the south pole for experiments with different CO_2 inventories. The black solid line shows the critic temperature for CO_2 condensation. The grey line with open diamonds shows the annual average temperature for experiments with time-constant frost albedo (0.795 in the north, 0.461 in the south); the grey dashed lines indicate the temperature annual maxima and minima. The black line with crosses shows the annual average temperature for experiments with insolation-dependent frost albedo; the black dashed lines indicate the temperature annual maxima and minima. The shaded area covers the CO_2 inventories with which the MarsWRF predicts a southern perennial CO_2 cap if the CO_2 frost albedo is insolation-dependent.

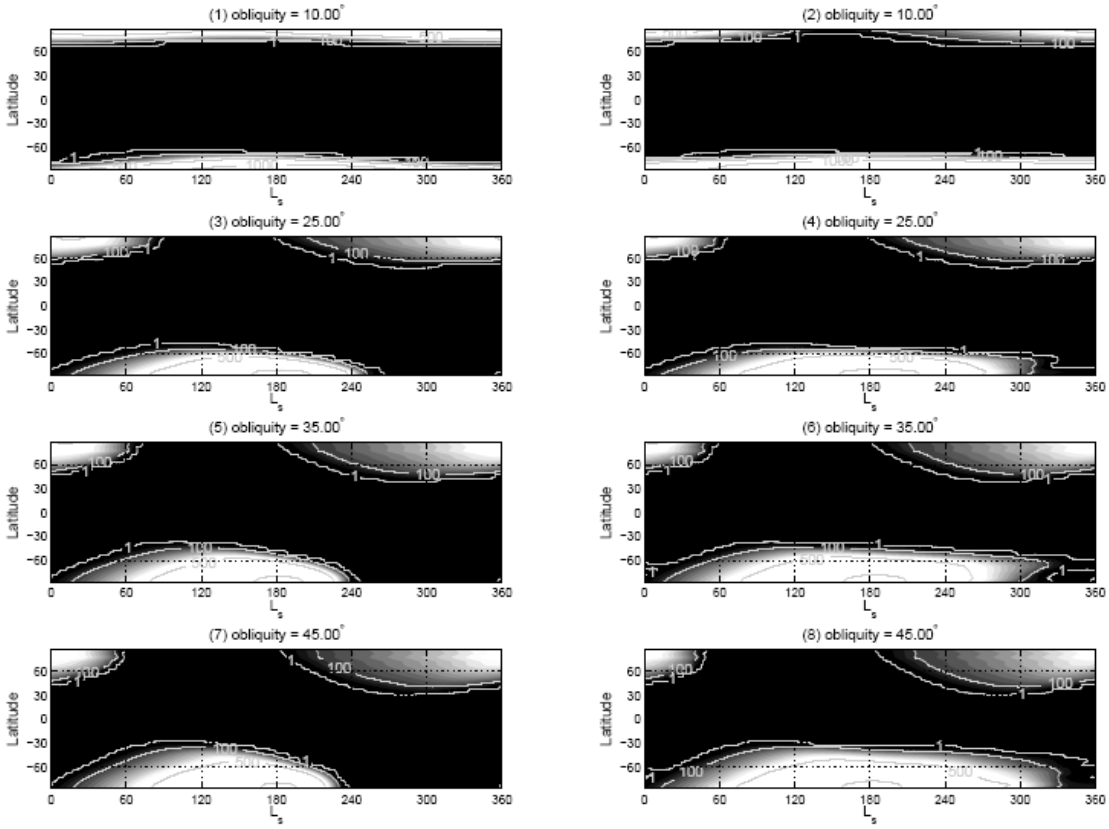

Figure 4.7: Annual variation of zonally averaged surface CO_2 deposition for simulations with different obliquity. The column of panels on the left hand side (panels (1), (3), (5), and (7)) are for simulations assuming controlled time-constant frost albedo (0.795 in the north, 0.461 in the south). The column on the right (panels (2), (4), (6) and (8)) are for simulations assuming insolation dependent frost albedo.

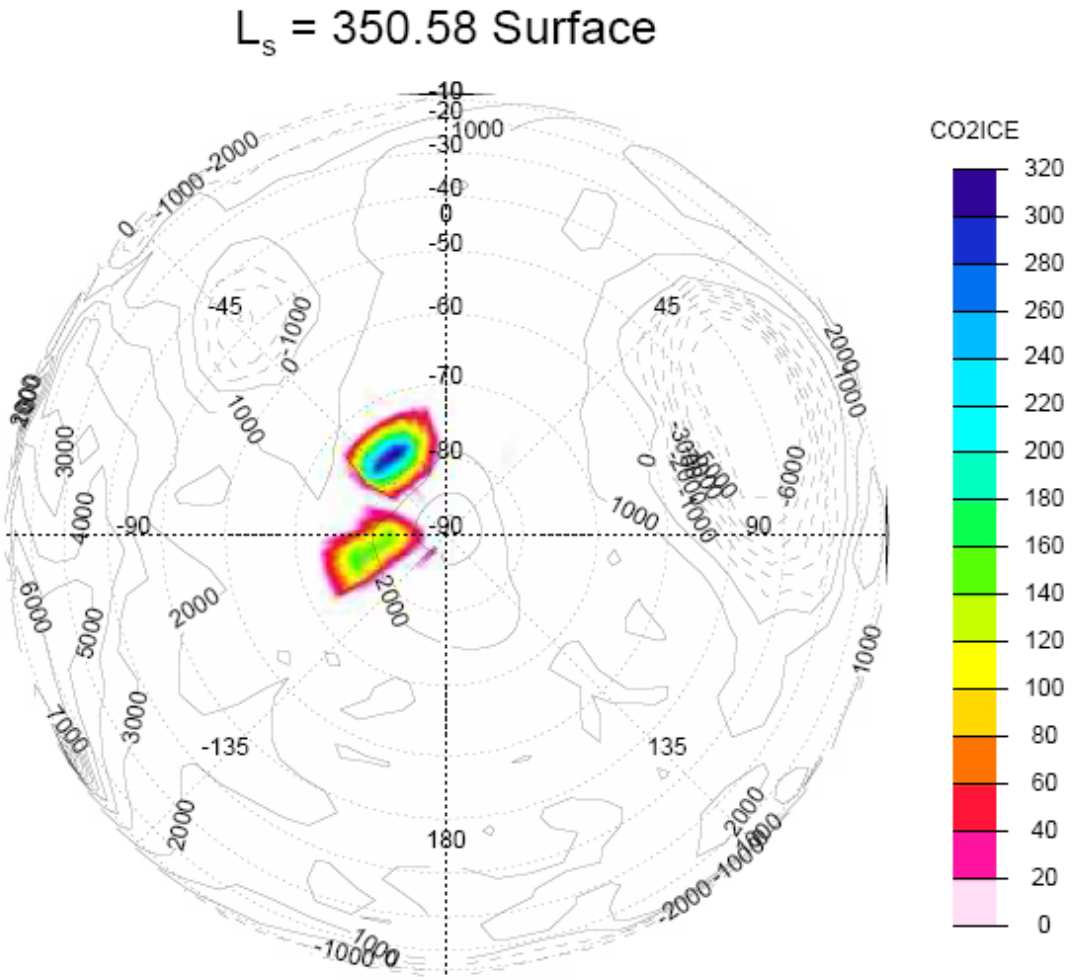

Figure 4.8: Same as Figure 4.3, except the total CO_2 inventory in this simulation is 1.53×10^{17} kg.

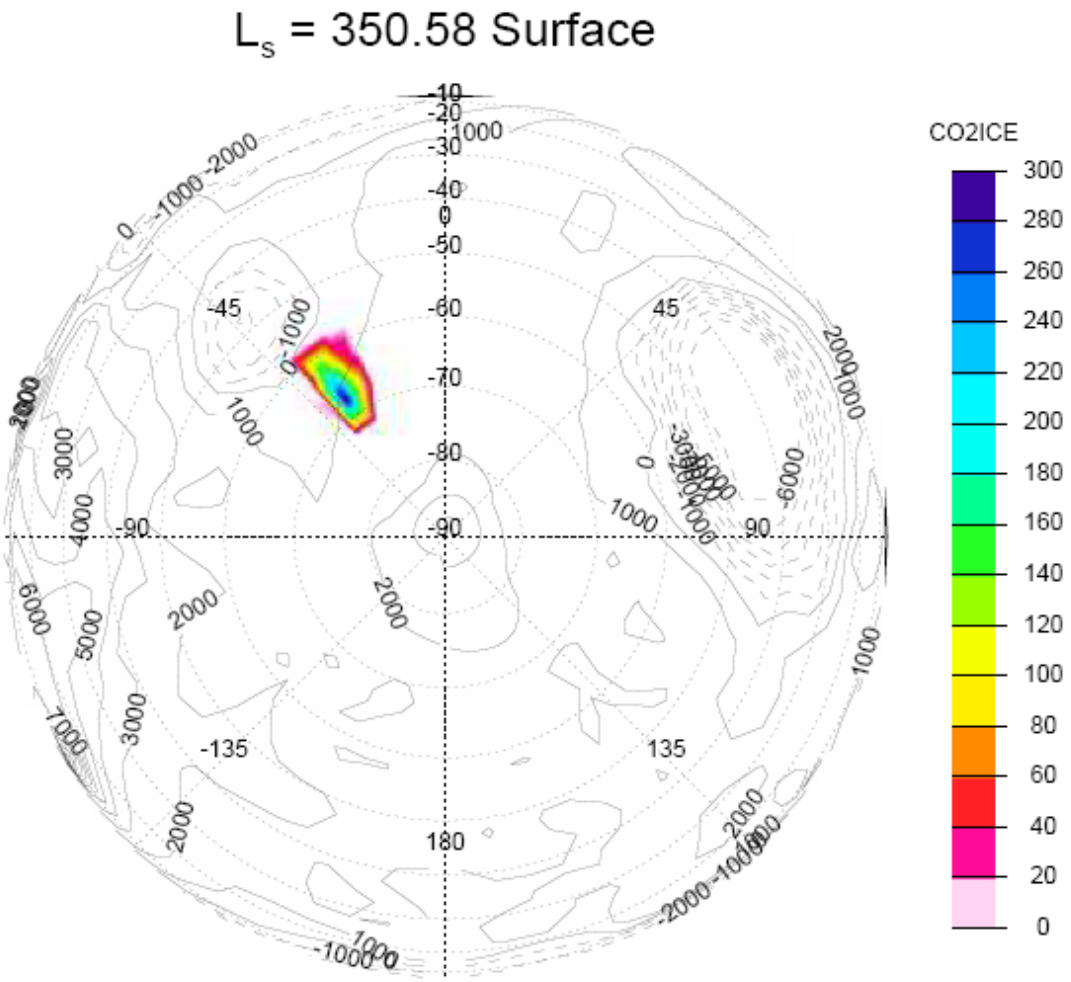

Figure 4.9: Same as Figure 4.3, except the obliquity of Mars in this simulation is 35°.

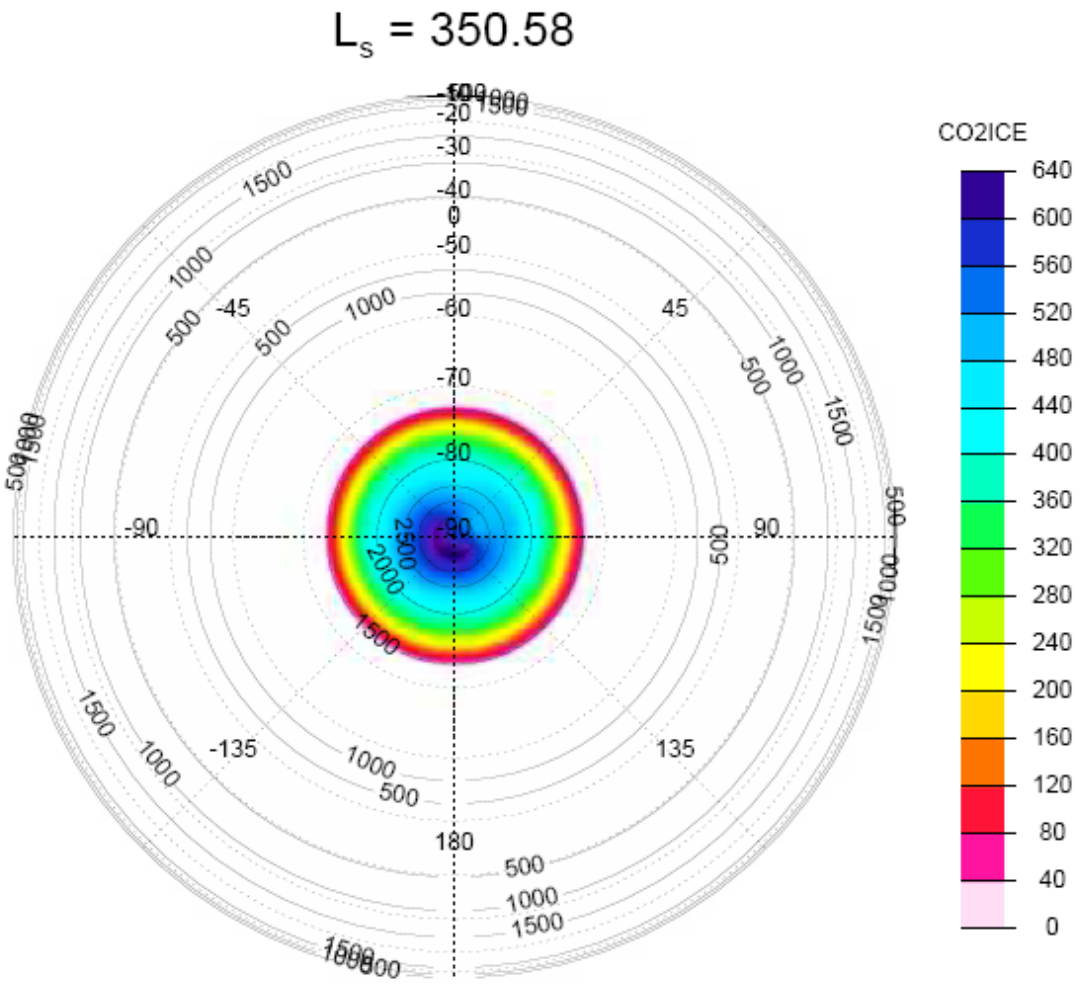

Figure 4.10: Same as Figure 4.3, except the zonal average value for topography and thermal inertia was used, and the total CO_2 inventory is 1.53×10^{17} kg.

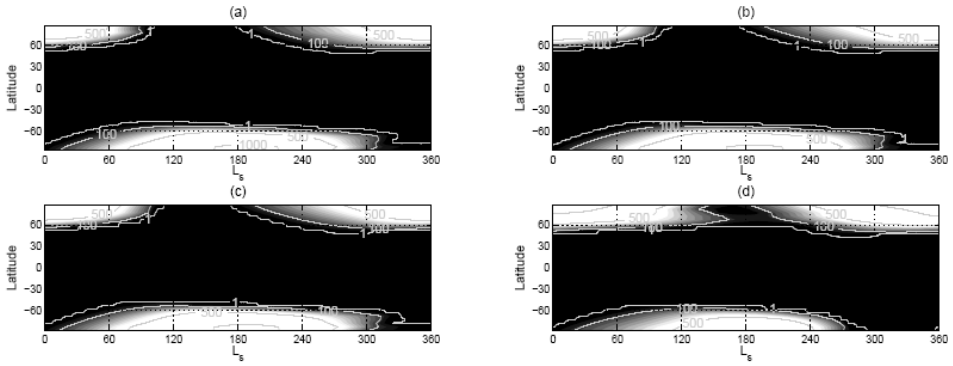

Figure 4.11: Same as Figure 4.2. Panel (a) shows the zonal averaged CO_2 ice annual cycle for the simulation which has the same setup as panel (b) of Figure 4.2 except the northern cap albedo is set to 0.785. Panel (b) is for the same setup as panel (a) except the regolith thermal inertia is set to the global average (216 J m^{-3} K^{-1}). Panel (c) is for an experiment in which the CO_2 ice albedo is decided by insolation according to Equation 4.1, ice emissivity is set to 0.8, regolith thermal inertia is set to 216 J m^{-3} K^{-1} and the current orbital parameters for Mars is used. Panel (d) is for an experiment whose setup is the same as for panel (c), except the perihelion and the aphelion is swapped.

Chapter 5: Modeling the non-condensable gas cycles

Abstract

We model the annual variation of non-condensable tracer gases in the atmosphere of Mars. Non-condensable trace gas (mostly nitrogen, N_2, and argon) mass mixing ratios are affected by the phase change of CO_2 and by atmospheric transport processes. The distribution of argon (Ar) abundance has been observed by the gamma ray spectrometer. A simple condensation scheme has been incorporated into MarsWRF. The model is able to qualitatively reproduce the Ar observations, including the seasonal evolving latitudinal distribution. However, the modeled magnitudes of maximum enrichment are much lower than observed. Whilst within measurement error, we suggest that an extra buoyancy term in the model may account for the underestimation. This missing process in the model dynamics should result from the vertical gradient in mean molecular mass as Ar mass mixing ratio increases near the surface. Smoothing Ar enrichment in the vertical should reduce susceptibility to transport by near-surface, off-cap circulation. Increasing the model resolution in the polar region also reduces the numerical diffusion and helps achieving the observed enrichment.

5.1 Introduction

In addition to the seasonal CO_2 cycle we have introduced in the previous chapters, another interesting phenomenon caused by the phase change of CO_2 is the argon (Ar) mass mixing ratio annual cycle. When CO_2 gas condenses onto the ground, the non-condensable gas is left behind in the atmosphere, leading to an enrichment of its local mass mixing ratio, and vice versa when CO_2 ice sublimates. Its distribution is further modified as a result of the atmospheric circulation. Since Ar does not react (in a fast pace) with any other known species in the atmosphere of Mars, its seasonal and geographical variations is a great indicator for tracking the motion of the atmosphere.

Ar abundance has been measured by the gamma ray spectrometer (GRS) [*Boynton et al.*, 2002] on the Mars Odyssey orbiter [*Saunders et al.*, 2004] for one and half Martian years. Because of the technical difficulties in instrumentation, only zonally averaged distributions of Ar have been reported assuming homogenous vertical distribution (latitudinal and temporal variations are available). Nonetheless, this data is extremely valuable. Successful modeling of the observed Ar cycle with a GCM is useful both as estimate in its own right and as a constraint on Mars GCMs [*Sprague et al.*, 2004; *Sprague et al.*, 2007].

Nelli et al. [2007] used the NASA Ames Research Center (ARC) Mars GCM to study the Ar enhancement in the Martian atmosphere. It was the first attempt to model the non-condensable gas cycle with a full 3D Mars GCM. They were able to reproduce the enrichment dichotomy in the two different poles observed by GRS. They also showed that the dichotomy was due to the different strength and timing of transient eddy diffusion between the two hemispheres. However, the simulated magnitude of enhancement in the

south pole during the southern winter season was only a half as much as observed. They argued that this miss match may be a result of the local maximum at about 0.5 mbar level instead of a decreasing non-condensable gas profile as a function of height.

We incorporate a simple CO_2 condensation scheme to MarsWRF [*Richardson et al.*, 2007] to study the formation of seasonal polar CO_2 ice caps. We parameterize the non-condensable gas mass mixing ratio change as a result of CO_2 condensation/sublimation and allow the tracer gas to be carried around in the atmosphere by resolved dynamic processes and by diffusion (representing sub-grid scale motions). Meanwhile, we use MarsWRF outputs, most surface pressure cycle to provide column atmospheric mass, to calibrate the GRS data and obtained the enhancement cycle of Ar. Comparing model outputs with calibrated observations provides a useful way to study the tracer gas transportation in addition to testing the validity and completeness of the GCM parameterizations of physical processes.

In section 5.2, we briefly introduce the model we use for this study, including an overview of the MarsWRF settings, the simple surface condensation scheme, the treatment for the non-condensable gas, and the convective adjustment method. Model results and discussions are shown in section 5.3. Efforts to further refine the simulations are presented in sections 5.4 and 5.5. Section 5.6 provides conclusions and discussions.

5.2 Model descriptions

5.2.1 MarsWRF setups

As stated in Chapter 2, we utilize MarsWRF for this dissertation. See *Richardson et al.* [2007] for a detailed description of the GCM. For the experiments presented in this chapter, we use the current Martian orbital parameters. Mars Global Surveyor (MGS) Thermal Emission Spectrometer (TES) dust opacity climatology is approximated by an empirical function and is fed to the radiative transfer calculations in MarsWRF. We include the simple energy balance model for CO_2 phase change for both surface condensation and atmospheric condensation as described in Chapter 2. Due to its small mass, water cycle is not included because we expect it to introduce trivial, if any, effects to the Ar cycle. CO_2 clouds and water ice clouds are not simulated.

We start with a grid structure yielding 36 × 64 × 40 (latitude, longitude, vertical) points. This setting provides a global coverage of Mars with the top of model reaching up to 0.006 Pa, or about 80 km above the surface. Its horizontal resolution is 5.0 degree of latitude by 5.6 degree of longitude. In addition, we experiment with other horizontal resolutions including 18 × 32, 72 × 128, and 144 × 256 in order to test the numerical issues related to number of grid cells of the model. A unique feature of MarsWRF is that it has a "rotated pole" mode, which allows the polar dynamics to be much better represented than the typical cylindrical projection models because the polar Fourier filter will no longer cause problems. We leverage this rotated pole ability for some of the experiments in this study.

5.2.2 CO_2 condensation

From the surface energy balance described by Equation 2.1, we work out the amount of CO_2 gas (δm_s) that is involved in the phase change at the surface. This amount can be either positive (condensation) or negative (sublimation) depending on the net energy flux. In the atmosphere, when the model predicted layer temperature in the N-th layer (T_N) goes below the critical temperature ($T_{c,N}$), which is a function of local pressure and vapor mixing ratio, δm_N amount of atmosphere is transferred to CO_2 ice and the temperature of this layer is reset to $T_{c,N}$. We have

$$\delta m_N = C_p M_N (T_{c,N} - T_N) / L, \tag{5.1}$$

where C_p is the specific heat of the Mars atmosphere, M_N is the atmospheric mass of the N-th layer. Similar treatment for CO_2 phase change has been used in previous works [*Forget et al.*, 1998; *Pollack et al.*, 1990; *Wilson and Hamilton*, 1996].

For simplicity, we assume this amount of CO_2 is instantaneously put onto the surface and considered as surface condensation for the calculation of the non-condensable gas abundance. It reduces the computation work while introducing very limited amount of bias because the atmospheric condensation is much smaller than the surface condensation. The primary importance of including the atmospheric condensation is to prevent the atmospheric temperature from going below the critical temperature [*Christensen et al.*, 1998; *Clancy et al.*, 2000; *Leovy*, 2001]. Another neglected aspect of atmospheric CO_2 condensation is the microphysics and radiative effects of CO_2 clouds [*Mischna et al.*, 2000]. Model the ratiative effect of clouds is a subject under investigation in the community. A more complete CO_2 ice cloud formation scheme, including nucleation and particle growth will be discussed in

Chapter 6. From the perspective of mass exchange involved, CO_2 cloud formation is likely to be overwhelmed by the surface phase exchange, therefore is excluded in this study. Same argument holds for water ice cloud.

5.2.3 Non-condensable gas

Besides CO_2, the Martian atmosphere is mainly comprised of N_2, Ar, CO, H_2O, and O_2. The predominant species, N_2 and Ar, do not condense in winters. We therefore denote them as non-condensable gas (or non-condensables) as oppose to the condensable CO_2 or H_2O vapor. We have

$$q_{tra} = 1 - q_{vCO2}, \tag{5.2}$$

where q_{tra} is the mass mixing ratio of all the non-condensable tracers and q_{vCO2} is the mass mixing ratio of the CO_2 vapor (note this equation holds regardless the mixing ratio is for a single grid, for a series of grid, or for the column integral). This relationship is guaranteed simply by mass conservation. When there is CO_2 phase change, we adjust the mass mixing ratios of CO_2 vapor accordingly. Assuming a constant mixing ratio of Ar (q_{Ar}) within the non-condensable gas, we have

$$q_{Ar} = c\, q_{tra}, \tag{5.3}$$

where c is the mass fraction of Ar within the non-condensable tracers. We set c = 0.458 assuming the non-condensable gases are mainly N_2 and Ar and using their volume mixing ratios given in Table 4.3 in *De Pater and Lissauer* [2001]. From (5.2) and (5.3), we can

always back out the mass mixing ratio of Ar from the mass mixing ratio of CO_2, which is carried in MarsWRF as a tracer.

When CO_2 condenses to the ground, we calculate the total amount of CO_2 gas *dm* that needs to be converted to ice.

$$dm = dm_s + \sum dm_N \ (N = 1, 2, \ldots 40), \tag{5.4}$$

where dm_s is the mass of the surface condensation, dm_N is the atmospheric condensation in the N-th layer (layer 1 is at the bottom of the atmosphere). q_{vCO2} is then adjusted accordingly in the first layer. If this amount (*dm*) is larger than the amount of CO_2 available in the lowest layer ($m_1 = q_{vCO2,1} \times M_1$, $q_{vCO2,1}$ being the mass mixing ratio of CO_2 vapor in layer 1, M_1 being the atmospheric mass of the layer 1), we set the mass mixing ratio of CO_2 in the lowest layer ($q_{vCO2,1}$) to zero and remove *dm'* of CO_2 away in the layer above, where

$$dm' = dm - m_1 = dm - q_{vCO2,1} M_1. \tag{5.5}$$

q_{vCO2} in the layer above is then modified accordingly. This adjustment keeps going upwards recursively if the next layer again does not contain enough CO_2 to match *dm'*. On the other hand, when sublimation occurs, the reverse adjustment of q_{tra} is only performed for the lowest layer of atmosphere. This algorithm guarantees column mass conservation for both CO_2 and the tracers while holding σ values (see footnote 5 in page 14) constant. It also ensures the mass mixing ratio profile of Ar to be a function decrease with height, which was not achieved by *Nelli et al.* [2007]. Sensitivity shows that the majority of the depletion of CO_2 results from surface CO_2 deposition event. As a result, whether to assume all the condensation occurring at the surface does not affect the long term climatology.

By advection and diffusion, the dynamic core of MarsWRF generates fluxes of CO_2 that tend to reverse this depletion. The inflow of CO_2 gas has to be fast enough to maintain CO_2 frost formation in the winters in order to match the observed pressure cycle. At the same time, the inflow of CO_2 will dilute the relative non-condensable concentration.

5.2.4 Buoyancy and convective adjustment

We propose a mechanism that may be related to an un-modeled vertical mixing process. We suspect that vertically mixing Ar away from the surface would make Ar less susceptible to equator-ward transport from the polar atmosphere. The proposed vertical mixing (sketched in Figure 5.1) is driven by the vertical gradient in the atmospheric mean molecular (and molar) mass between CO_2 (44 g/mol) and non-condensables (N_2 28g/mol, Ar 40 g/mol. Non-condensable being lighter mainly due to the existence of N_2). Buoyancy is introduced by this discrepancy of molecular mass in the vertical direction, and could cause convection in a thermally-stratified atmosphere. Similar ideas due to the presence of water vapor have been suggested by previous literatures [*Ingersoll*, 1970; *Weiss and Ingersoll*, 2000]. We do not present simulations with this process included, since it would require a rewriting of the model dynamical core to allow for a spatially and temporally variable average gas constant R (J kg^{-1} K^{-1}) and implication of virtual potential temperature [*Holton*, 2004]. We intend to investigate such a modification in the future.

In addition to the buoyancy caused by surface condensation, the convective available potential energy (CAPE) introduced by atmospheric CO_2 condensation may also contribute to mixing in the vertical direction [*Colaprete and Toon*, 2003; *Colaprete et al.*, 2008]. We do

not include a microphysics model to simulate cloud formation in this version of MarsWRF, yet do account for atmospheric condensation in terms of energy balance. Because CAPE boosts vertical mixing and CO_2 cloud forms mostly during polar winter times, we have more incentive for the inclusion of extra vertical mixing.

Indeed, we introduce a simple convective adjustment algorithm to the non-condensable tracer profile calculation. When there is CO_2 phase change near the surface, we calculate the tracer profile using the method described in the previous section. If the net phase change of CO_2 is from gas to solid, i.e., net condensation, we make the tracer mass mixing ratio uniformly distributed throughout the entire corresponding atmospheric column while holding the integrated column masses of both condensables and non-condensables constant. This is equivalent to forcing an infinitely fast (compared to the time step used in MarsWRF) vertical mixing when air parcels near the surface is the lightest. On the other hand, if the net phase change is from solid to gas, i.e., net sublimation, no further action is taken because the newly released CO_2 from the frost makes the lowest layer even heavier therefore providing a stable scenario. In this scenario, the non-condensable tracer is more diluted near the surface. Similar convective adjustment practices for tracers are frequently used in earth GCMs when excessive dynamical mixing is needed but could not be represented by GCM numerics.

For MarsWRF, this convective adjustment increases the enrichment of non-condensables near the south pole during the southern winter by 10 to 15 percent, depending on the coordinator system setup. Such adjustment may be favorable because it only matters the Ar cycle and helps the GCM migrate at the desirable direction. We will discuss why the

change of Ar vertical distribution results in this increase in section 5.5. Meanwhile, all the runs shown in the next section are simulated with this convective adjustment method.

5.3 Model results

In this section, we present the annual cycles from the second Martian year of the MarsWRF simulations. By this time, the modeled CO_2 (and Ar) cycle has already reached equilibrium, which takes about 200 sols to attain (we initiate the soil in MarsWRF with previous model results, which has been integrated for so long that the subsurface layers have already reached equilibrium. Hence, dynamically, the model spins up in a few tens of days, so CO_2 cycle equilibration dominates the timescale).

5.3.1 Surface pressure

The surface pressure cycles in MarsWRF near the two VL landing sites are shown in Figure 5.2. These outputs have been corrected for the difference in elevation resulting from the non-perfect alignment of the numerical model grid point with the actual lander locations. The pressure cycles have larger short term variation in the northern fall and winter (the curve is more noisy during these seasons), which agrees very well with the VL data. Additionally, the phases of the two cycles match closely with that of the VL data. There are two peaks every year: the higher peak appears between Ls 240° and 270°, while the lower one appears near Ls 60°. The decrease of surface pressure after the two peaks is due to the surface condensation in the northern and southern hemispheres, respectively. Over the course of a

year, one can find a small phase shift and some disagreements of the absolute values between the model and the observation. The features above were also reported by other GCM studies [*Forget et al.*, 1998; *Haberle et al.*, 2008; *Hourdin et al.*, 1993], and MarsWRF compares well with previous GCM models of the CO_2 cycle and surface pressure observations. While better pressure cycle can be done via tuning of seasonal CO_2 ice emissivity, albedo, and total CO_2 inventory in the system [*Guo et al.*, submitted-a], whose physical meaning can be explained by the aliasing of physical processes, the setup used in the chapter assumes same emissivities and albedos for ices in different hemispheres, providing physical consistency. Besides, the resulted surface pressures are within 5% of the observed value recorded by the VLs. Such surface pressure error is likely to be good enough for resolving the Ar cycle.

5.3.2 Surface CO_2 ice deposition

The zonally averaged CO_2 ice surface deposition is shown by the black contour lines in Figures 5.3 and 5.4. At both poles, CO_2 frost forms during the winter season. The southern seasonal cap extends a little further to the mid-latitude region than the seasonal cap in the north. The surface density of CO_2 ice is higher in the south, where it reaches 1085 kg/m^2, corresponding to a thickness of 70 cm. It agrees very well with the Mars Orbiter Laser Altimeter (MOLA) measurement of the seasonal elevation change in the southern polar region [*Smith et al.*, 2001]. The maximum density in the northern pole is roughly 800 kg/m^2, which is consistent with other model predictions and GRS observations [*Aharonson et al.*, 2004; *Feldman et al.*, 2003].

5.3.3 Annual cycle of Ar

The annual cycle of zonally averaged column Ar mass mixing ratio (q_{Ar}) is shown in Figure 5.3. The averaged mass mixing ratio of Ar agrees with what was measured by the VLs [*Owen et al.*, 1977]. As expected, enrichment of Ar in terms of its mass mixing ratio is seen during the growing phase of CO_2 frost. After the winter solstices, the seasonal caps start to retreat and q_{Ar} decreases accordingly due to the sublimation of CO_2 ice, which dilutes the non-condensables. As soon as the polar caps are completely gone, terminating the supply of pure CO_2 at the surface, further decrease of q_{Ar} also halts. Instead, q_{Ar} increases because of the mixing with air from lower latitudes. The annual process is also evident in Figure 5.4, which shows selected latitudinal cross sections derived from Figure 5.3.

We notice that the q_{Ar} cycles at different latitudinal bands transit in phase steadily. In the tropical regions, the cycles at opposite hemispheres do not diverge a lot in phase. Starting from the equator, the higher peak moves to the later part of a year as the sampling location moves to the north; and vice versa, the higher peak moves to the earlier part of a year as the sampling location moves to the south. For instance, in Figure 5.4, the thin blue curve (7.5°N) and the thick dashed blue curve (7.5°S) are very close to each other. The thin red curve (82.5°N) and the thick dashed red curve (82.5°S) are out of phase by roughly 180 degree, which is simply due to the timing of seasons at different poles.

In the equatorial regions, the q_{Ar} cycle has an obvious negative correlation with the surface pressure cycle (see Figure 5.2). The troughs/peaks in the q_{Ar} cycles coincide with the peaks/troughs in the surface pressure cycles. The lower troughs of q_{Ar} are evident at the period when the higher peaks of the surface pressure present. Notice in a hydrostatic model atmosphere, surface pressure is simply the mass of air in a column times the gravity divided

by the surface area. Therefore, this negative correlation between the q_{Ar} cycle and the surface pressure cycle suggests that the total Ar mass in low latitudes is relatively constant.

The peak value of q_{Ar} near the south pole is much higher than that near the north pole. This dichotomy of enrichment between two different poles is the most obvious in Figures 5.3 and 5.4. This dichotomy has been reported by observation teams and simulated using other GCMs [*Nelli et al.*, 2007; *Sprague et al.*, 2007]. The cause is thought to be the different behavior of eddy activities at different hemispheres. Stronger pole-ward transient eddies near the south polar region during souther winters help build up the high enrichment. On the other hand, during northern winters, strong stationary waves, transient eddies, and the zonal averaged transports tend to cancel each other. As a result, the total transport in the north pole is very stable and not much enhancement of the Ar can be built up during that period of time [*Nelli et al.*, 2007].

The zonally averaged column Ar mass per unit area (m_{Ar}) annual variation is shown in Figure 5.5. In general, m_{Ar} is larger in the northern hemisphere because of the different atmosphere thickness resulting from the topography. The Hellas basin introduces an increase of Ar mass between 30°S and 60°S. In the tropical region (between 30°N and 30°S for example), the column Ar mass does not change much in a Martian year. At higher latitudes (60°N/S or more), we see enrichment of m_{Ar} in the beginning of the winter seasons, which indicates transportation of Ar from the lower latitudes to the polar regions. This additional amount of Ar, combined with the decrease of total air mass is responsible for the increase of q_{Ar}. Similarly, a deficit of Ar mass can be found when the surface CO_2 frost starts to sublimate. It suggests an equator-ward flow transporting Ar away from the polar regions. When the sublimation is over, the meridional mixing brings Ar back to the poles and the

cycle starts over. Notice the enrichment dichotomy is less obvious when viewed as total column mass. It is offset by the huge atmospheric mass difference because of the huge elevation difference between the two hemispheres.

We represent our simulation in terms of the enhancement factors (EFs) and compare with calibrated data from GRS [*Sprague et al.*, 2004; *Sprague et al.*, 2007] in Figure 5.6. The EF is essentially the column mass mixing ratio normalized by the reference value given by the VLs. It tells us the relative enrichment of non-condensable gas as to the "standard" VL value near the equator (the definition of EFs was provided by *Nelli et al.* [2007]). The comparison of MarsWRF results and GRS data are presented in Figure 5.6. A similar annual pattern in the southern polar region (black dashed curve in Figure 5.6) can be identified. Both curves dwell above average between Ls 30° to 150°; and the small dip at Ls 70° is evident. The peak EF in MarsWRF outputs, however, is much smaller compared to the GRS record. The maximum EF is almost 10 times as much as the minimum value for the GRS records, while the difference is about 2 to 3 folds in the MarsWRF simulations. The peak EF of GRS is 6 while MarsWRF predicts 1.6 near the south pole, even lower than what has been reported by the ARC MGCM [*Nelli et al.*, 2007].

This mismatch is seemingly a result of excessively fast meridional mixing of Ar in the simulation for the southern hemisphere, which dilutes the q_{Ar} faster than it actually occurs. The increase of q_{Ar} after the complete sublimation of the southern seasonal CO_2 cap is much more abrupt than what the observations show. It suggests that the modeled polar vortex may have disappeared too rapidly, or may have not been strong enough, allowing excessive meridional mixing. In addition, the seasonal variation we found in the northern polar region is not obvious in the data. Even though our absolute values are within the detection error of

the GRS measurement, it seems at least plausible from the data that there may be different mechanisms controlling the dynamics of Ar in different hemispheres.

5.4 Transportation in polar region and effects of model resolution

In winter times, CO_2 ice condensed on the surface locks the surface temperature at the poles to the frost point, significantly lower than the soil temperature away from the seasonal caps. Because of this big thermal contrast between high and mid latitudes, strong circum-polar jets form. These high speed winds circling the seasonal caps form a polar vortex, cutting the Hadley circulation at 50 to 60 degree latitude [*Forget et al.*, 1999; *Richardson and Wilson*, 2002a]. It is almost universally agreed that the edge of the polar vortex forms some kind of barrier, so that the air in side it is to some extent isolated [*Sobel et al.*, 1997]. The dash lines in Figure 5.7 show the EFs at the two poles if there is absolutely no atmospheric motion. The underlying assumption for this thought experiment is that when CO_2 condenses, the non-condensables will be left behind, idling at the same location (latitude) where the condensation happens. For the southern hemisphere, the gradient of this "imaginary" curve keeps with the GRS observation from Ls 0° to 90°. It essentially suggests that for this period of time, the polar vortex is so strong that the atmosphere over the south pole does not leak any non-condensable gas away. In other words, the meridional transportation during this period is completely shut down. After Ls 90°, the two curves start to diverge. The zero-transport curve eventually over-shoots the observed curve, suggesting the containment vessel for the non-condensables breaks down.

Transportation of material across the polar vortex edge has been studied on earth and many numerical methods have been proposed [*Sobel et al.*, 1997; *Waugh and Plumb*, 1993; *Waugh et al.*, 1997]. A quantitative calculation, however, of such transportation has not been well established. In MarsWRF and many other GCMs, even if the vortex itself is not leaky (which is doubtable), wind represented in a finite number grid box coordinate system numerically strips materials away from the wall of the polar vortex. Accumulated in time, such numerical error will introduce significant but false equatorial transport of tracer, so called numerical diffusion [*Eluszkiewicz*, 2002].

In order to test the numerical behavior of MarsWRF in polar transportation, we vary the model resolution in high latitudes. Better resolution would improve the representation of the wind field and therefore reduce the numerical diffusion described above (and vice versa). There are two ways to increase the model resolution near the poles. One is simply using more grid points. This method is limited by computing power and storage space. The other method is leveraging the "rotating pole" capability of MarsWRF. There are two advantages of the latter method. Firstly, it provides more grid cells of rectangular shape at high latitudes in the "rotated" coordinate system, which is exactly what we desire. Secondly, it further reduces the numerical error due to the Fourier filter applied to the polar region in the normal cylindrical projection coordinate system. These two method can be combined (i.e. rotated pole with more gird points) to create even more desirable grid structure for polar simulations.

The standard MarsWRF runs uses a grid structure yielding 36 × 64 × 40 (latitude, longitude, vertical) points. We experiment with other horizontal resolutions including 18 × 32, 72 × 128, and 144 × 256 in both ordinary mode and "rotated pole" mode with the vertical convective adjustment. The calculation for the 144 × 256 cases take more than 4 weeks to

finish on a 64 processor parallel system. Further increase of number of grid cell will require unrealistic computation time and storage space, therefore has not been carried out. Results from these runs are compared as follows.

Figure 5.8 shows the EFs at the polar regions produced by the model using the ordinary cylindrical map projection but with different horizontal resolutions. It is clear that better resolution in the polar region helps the south polar region retaining more Ar during the southern winter. Near the south pole (upper panel of Figure 5.7), when less grid points (blue) are used, the EFs during the southern winter are even smaller than those of the standard case (red). The maximum of the blue curve reaches only 1.4. If the grid points are doubled in the horizontal directions (green), an obvious increase of EFs for the first half of the year can be identified. The peak value for that season rises from 1.6 to 2.1. Further increase of the number of grid points to 144 × 256 boosts the maximum EF to 2.7 (magenta). Meanwhile, for all the runs above, the EFs in the second half of the year remains the same, except for the half resolution case. For the northern pole (lower panel), all cases show similar annual behavior, except for, again, the low resolution case.

When compared with GRS measured EFs (grey curve with errorbars), we indeed identify the improvement in the southern winter time at the south pole. Even though the model predictions are still not close to the observed values, they approach the observation when more gird points are utilized. The maximum EF of the highest resolution case reaches 2.7, close to what *Nelli et al.* [2007] predicted, though the timing of the maximum is different. ARC MGCM predicted the maximum EF at 82.5°S to appear near Ls 120°, while MarsWRF predicts this peak to arrive 20 to 30 degrees of Ls later. Nonetheless, some features likely with higher frequencies are resolved by MarsWRF, such as the local minima near Ls 120°

and Ls 68°, which were not captured in the previous literatures. For the northern polar region, every MarsWRF simulations show EFs in general agreement with *Nelli et al.* [2007] and GRS measurements, except the coarse resolution case (blue), which has smaller variation than the rest.

The results of the rotated pole mode simulations are shown in Figure 5.9. In this mode, when coarse grids are used (18 × 32, blue), akin the ordinary coordinate system we find less enhancement for both poles through a year. The EFs with the standard resolution (red) is already improved in the south pole during the south winter. The maximum is 2.1 compared to 1.6 of the normal coordinate system simulation. On the other hand, it does not possess the same short term variability. Further increase of grid points (green and magenta) does not further lift the EF by much. The maximum increases from 2.1 to 2.2 (for both green and magenta). However, it does introduce more shorter-period variability in the winter times for both hemispheres.

From the analysis above, we conclude that the current tracer transportation calculation in MarsWRF is sensitive to the choice of horizontal grid size. In general, runs with finer grid sizes match the GRS observation better, and vice versa. It is likely that in order to resolve the polar vortex edge and represent the transportation correctly during the southern winter, MarsWRF needs to have grid boxes smaller than some critical size. This critical size could be different for different projection modes, i.e., the normal cylindrical projection and the “rotated pole”. The size of a grid box near the pole in a standard number normal projection mode is smaller than that in a standard number “rotated pole” mode, yet the former produces less enrichment of Ar during southern winter that the latter. In this sense, the “rotated pole” mode of MarsWRF has a great advantage in polar tracer transportation

studies (or in other polar atmospheric studies). It reaches comparable quality of answer to the normal projection mode with less grid points, which requires less computation power and storage space. If we are only interested in the seasonal variation of Ar, the use of standard number of mesh grids (36 × 64 × 40) in a "rotated pole" setup would suffice.

Although we have advanced the enrichment of Ar near the south pole during the southern winter by increasing the number of grids, we still do not match the GRS observations. The maximum EF from MarsWRF is at least two times too small. Further increase of model resolution is not realistic computationally, nor does it seem to solve this problem. For example, the 72 × 128 and the 144 × 256 cases differ only slightly, if any of the difference is significant. We sense that we have almost approached the limit of MarsWRF in simulating the enrichment of non-condensable gas with the current tracer transportation scheme. We tend to conclude that near the south pole during southern winter, the achievable upper bound of Ar EF by MarsWRF should be about 3, which agrees with previous literature [*Nelli et al.*, 2007].

Of course, this simulation could be further refined by utilizing better transportation scheme, which is currently under investigation. In addition, the "rotated pole" mode is a pioneer in the modeling community and needs further validations. These issues, however, are beyond the scope of this dissertation. The next generation of MarsWRF is under investigation by the Richardson group and NCAR. Some of the intrinsic shortness will hopefully be improved in the latest version of WRF.

5.5 Vertical distribution of non-condensable gas

As stated at the end of section 5.2, after introducing the convective adjustment, the peak EF during southern winter simulated by MarsWRF increases 10% to 15%. *Colaprete et al.* [2008] has shown that after the inclusion of vertical mixing due to CAPE, the column non-condensable gas can be further enriched during southern winter. *Nelli et al.* [2007] using the same GCM (without vertical convection and CAPE) mentioned that Ar has an unphysical concentration up in the atmosphere. A common character among these runs which better represent the enhancement is evident: the non-condensable gas is more dispersed vertically. If the non-condensable gas is no longer concentrated near the surface, where it is most susceptible to transport by near-surface, off-cap circulation, the column Ar can be more enriched than before because of less meridional transportation. Similar idea has been brought up by *Colaprete et al.* [2008].

However, both GCMs (MarsWRF and ARC MGCM) under-predict the enhancement compare to GRS observation. One possibility is that the simulated vertical distribution of Ar was not perfectly physical and the GCMs had missed some significant processes. Because the meridional transportation behaves differently at different altitudes, the total column Ar cycle may be sensitive to the vertical profile. In order to understand how the annual Ar cycle responses to different vertical Ar distributions, we perform some idealized experiments. When CO_2 condensates to the surface, we designate the Ar enrichment which used to focus near the surface to selected heights while keeping the wind field for advection the same. By comparing the resulted Ar EF annual cycles, we try to gain some insights about the relative importance of meridional transportation at different heights.

We test four concentrating layers: experiment 1: during condensation, Ar concentrates between 0 to 5 km (denote it as layer 1); experiment 2: between 5 to 20 km (layer 2); experiment 3: between 20 to 40 km (layer 3); experiment 4: between 40 km to model top (about 70 to 80 km at different latitudes, layer 4). The model uses the standard number of grid cells and the normal cylindrical projection. The results are shown in Figure 5.10. In the experiments that Ar is concentrated in either 0 to 5 km or 20 to 40 km, we see larger enhancement in winter seasons than the standard run with convective adjustment. The EFs near the south pole reach 2.0 in exp. 1 and 2.4 in exp. 3. However, near the north pole, they also go up to 1.7 in exp. 1 and 3.2 in exp. 3. Slight increase of EF can be found in the winter for exp. 4. As a summary, near the south pole, the tracers are better contained in the south pole during the southern winter in layer 1 (0 to 5 km) and layer 3 (20 to 40 km), while they are more vigorously transported northward in layer 2 (5 to 20 km). Near the north pole, the tracers can be sealed in the north pole efficiently in layer 1 for most of the northern winter; more efficiently in layer 3 for a part of the north winter starting at Ls 240°; and for a small fraction of winter in layer 4 (40 km and above). By contrast, the tracers are rapidly transported southward in layer 2. These behaviors suggest that in layer 3, the polar vortex edge is the least permeable to tracers, even though the zonal wind is not the strongest. On the other hand, the excessively low EFs in exp. 2 imply that the tracers are transported most vigorously equator-ward at this pressure level, where zonal wind is not the weakest. In our simulations with the convective adjustment, the excessive equator-ward transportation in layer 2 is probably cancelled by the better containment in the other layers

A local maximum of non-condensable gas found in the ARC MGCM results was believed to be the cause of the low EF in winter [*Nelli et al.*, 2007]. Interestingly, the local

enrichment is at 0.1 to 0.8 mbar, which is contained in the second layer of our experiments above. We have just shown that the equatorial transportation in layer 2 is the most active. If the concentration of Ar in layer 2 can be reduced, less equatorial transportation should increase the column EFs.

5.6 Conclusions and discussions

The Ar cycle presented in this chapter obtained from MarsWRF using a simple model of CO_2 condensation/sublimation qualitatively confirms our ideas about the dynamics associated with CO_2 surface condensation. When CO_2 condenses out in the winter seasons, non-condensable gases are left behind in the atmosphere, which increases the observed Ar mass mixing ratio. The pole-ward transportation of Ar in winter further enhances this increase. The polar enrichment dichotomy, i.e. the higher peak EF in the south, due to different dynamics in different hemispheres is resolved. When compared with GRS observations, we found that Ar is more vigorously transported in the polar regions than the tropics.

The modeled EF in the north polar region is within the detection error of GRS. We devote most of our effort trying to minimize the gap between the simulations and GRS measurements in the south. With aid of the convective adjustment, increased resolution in the polar regions, and the unique "rotate pole" feature provided by MarsWRF, we are able to increase the maximum EF from 1.6 to 2.7. This maximum agrees with previous literature, though both modeling work under-predict the peak EF by at least 100%. Further increase

seems to be limited by computation power and, more likely, the horizontal advection algorithm.

One needs to be extremely careful when consider a new advection driver. For MarsWRF, heat and momentum are also transported using the same horizontal advection algorithm and they seem to behave correctly (and physically, it should be the case). Tuning the transport of Ar to match the GRS observation may result in wrong distribution of energy and momentum, thus ruin the major purpose of the GCM.

There is still room to improve with the current advection scheme. The convective adjustment is simple and can be more sophisticated when varying gas constant is included. The "rotated pole" feature of MarsWRF is not extensively validated. With help of the next version of MarsWRF, we should be able to utilize much more computation power and better numerical methods for tracer transport.

From the comparison of EFs between a perfectly sealed polar region and the GRS observation (Figure 5.7), one may draw the conclusion that from Ls 0° to 90°, the air is perfectly contained by the southern polar vortex. It is very difficult to imagine that the atmosphere can be as efficient as a solid container in keeping gases from escaping. GCM simulations support this argument. This could potentially suggest brand new physical phenomenon or spacecraft measurement error.

Figures

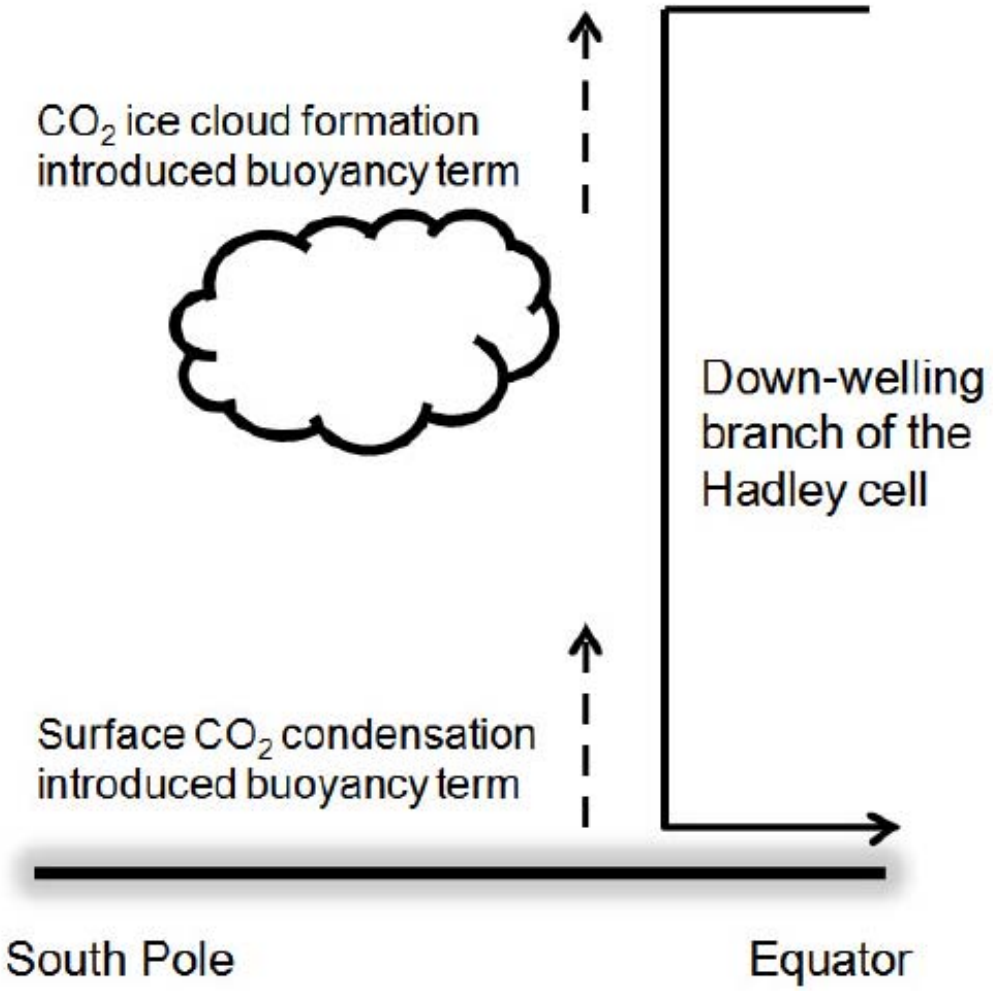

Figure 5.1: Sketch of the buoyancy effect of the non-condensable gas.

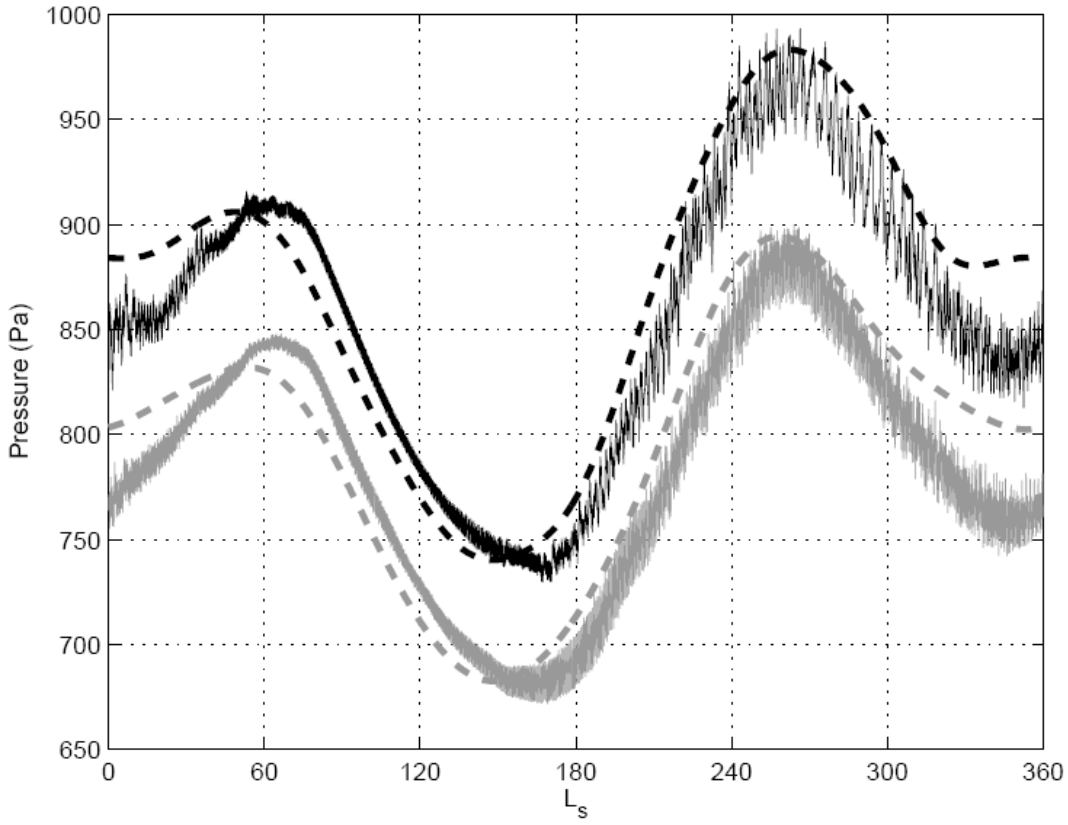

Figure 5.2: Pressure cycles at the VL landing sites. Grey dashed line: smoothed VL1 (22.5°N, 50°W) surface pressure data; black dashed line: smoothed VL2 (48.3°N, 225.9°W) surface pressure data (these two smoothed curves are polynomial fit to the VL observations provided by *Tillman et al.*, 1993); grey solid line: MarsWRF surface pressure cycle near VL1 site; black solid line: MarsWRF surface pressure cycle near VL2 site.

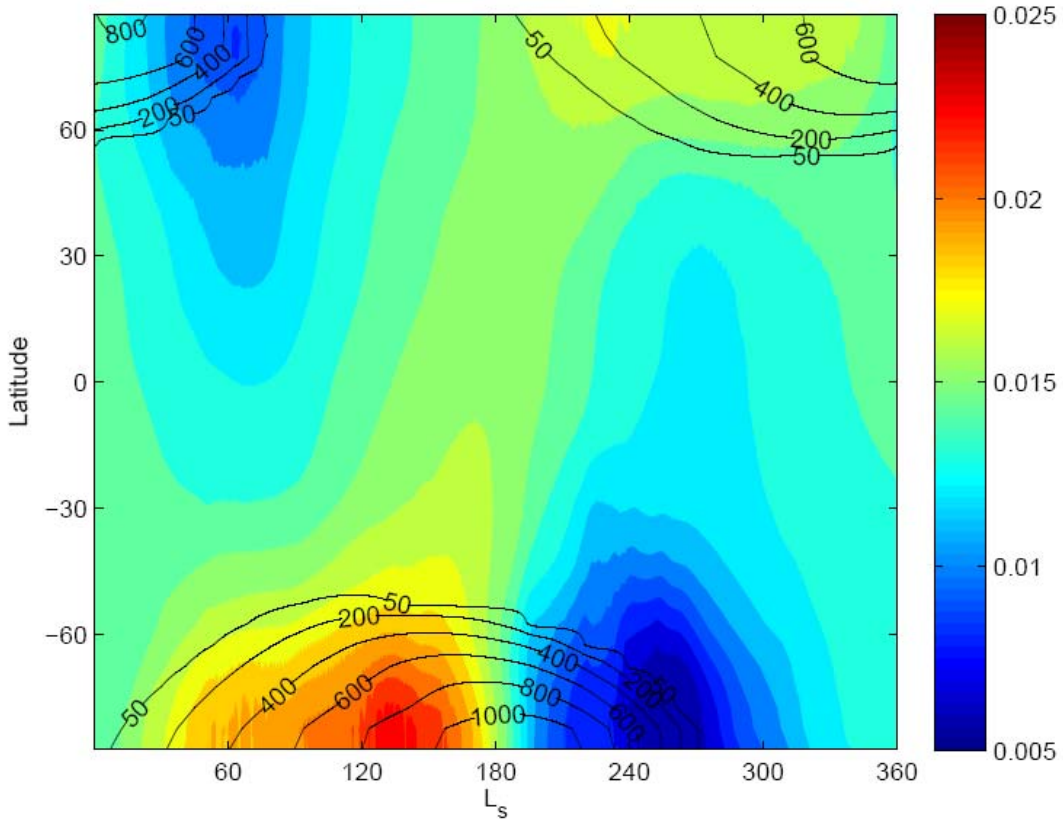

Figure 5.3: Annual Ar variation. X-axis: Ls in degree. Y-axis: north latitude. Color: Column mass mixing ratio of Ar (q_{Ar}, unitless), zonally averaged. Black contour: seasonal variation of CO_2 ice surface density (kg/m^2), zonally averaged.

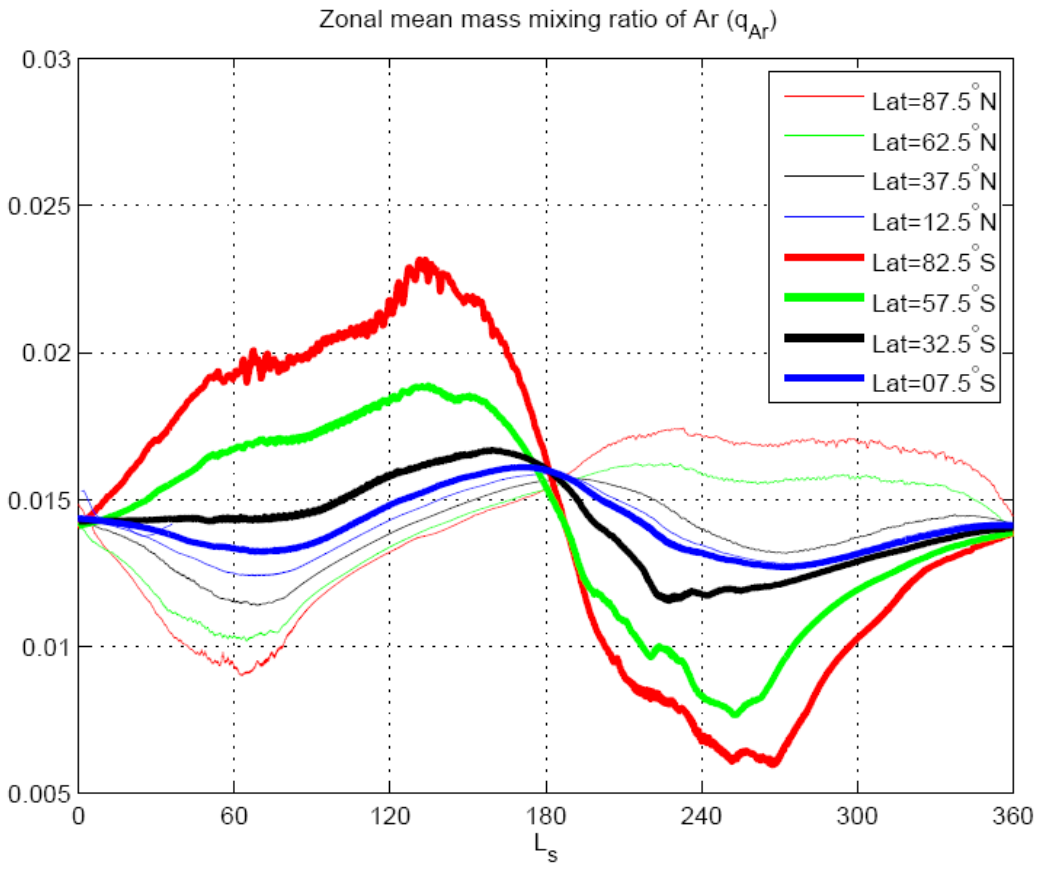

Figure 5.4: Seasonal variation of the zonally averaged column mass mixing ratio of Ar (q_{Ar}) at different latitudinal bands, whose central latitudes are 82.5°N (thin red), 57.5°N (thin green), 32.5°N (thin black), 7.5°N (thin blue), 82.5°S (thick red), 57.5°S (thick green), 32.5°S (thick black), 7.5°S (thick blue).

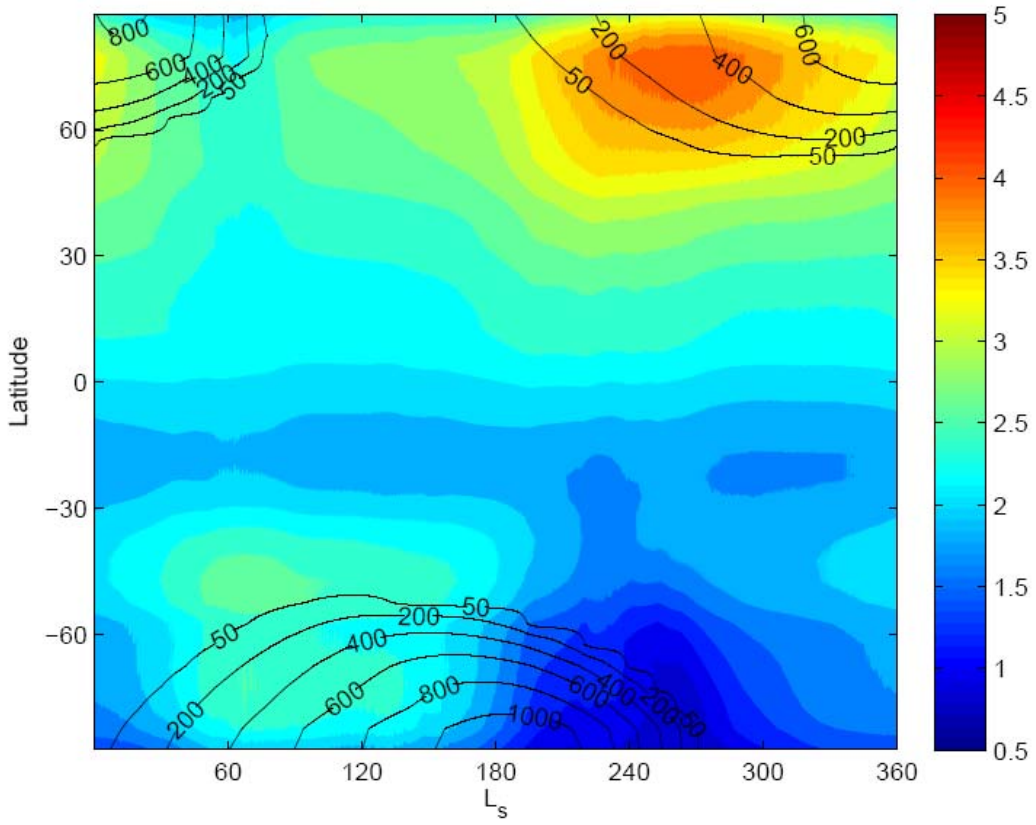

Figure 5.5: Same as Figure 5.3, except the color shows the zonally averaged column mass of Ar per unit aera (m_{Ar}, kg/m^2).

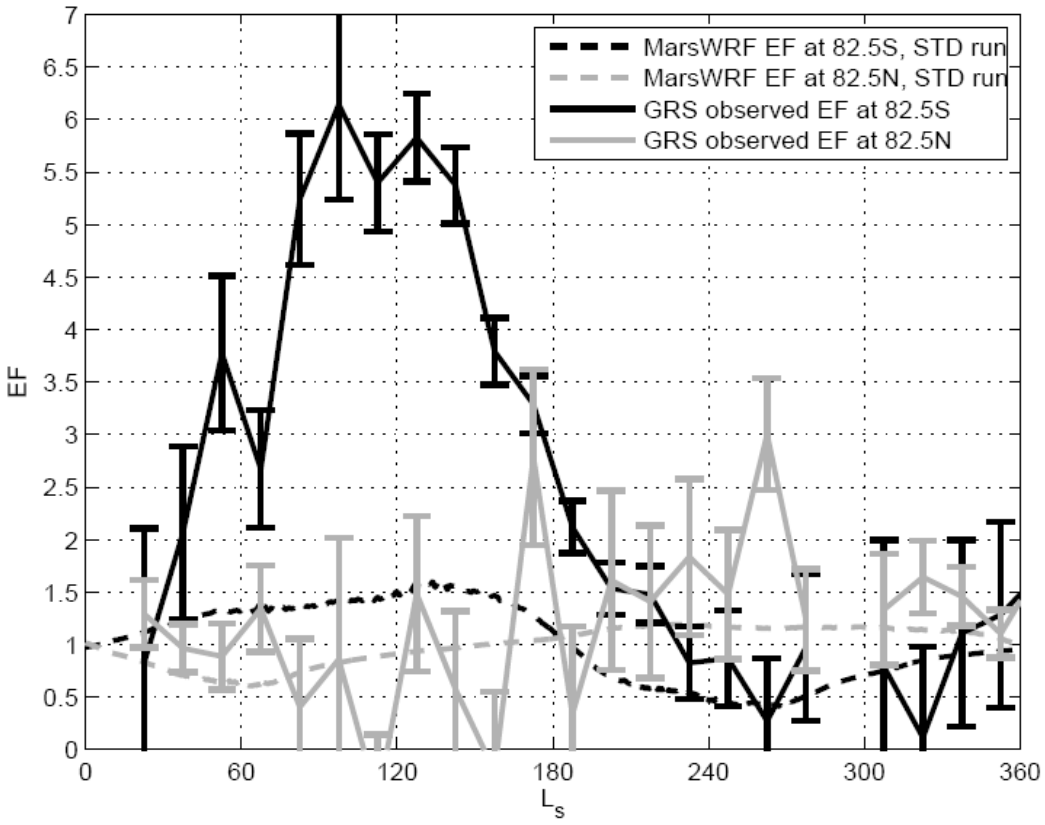

Figure 5.6: Enhancement factors (EFs) annual variation at high latitudes. Dashed lines: EFs of Ar at 82.5°S (black) and 82.5°N (grey) produced by MarsWRF. Solid lines with errobars: EFs of Ar at 82.5°S (black) and 82.5°N (grey) given by GRS observations calibrated with MarsWRF outputs.

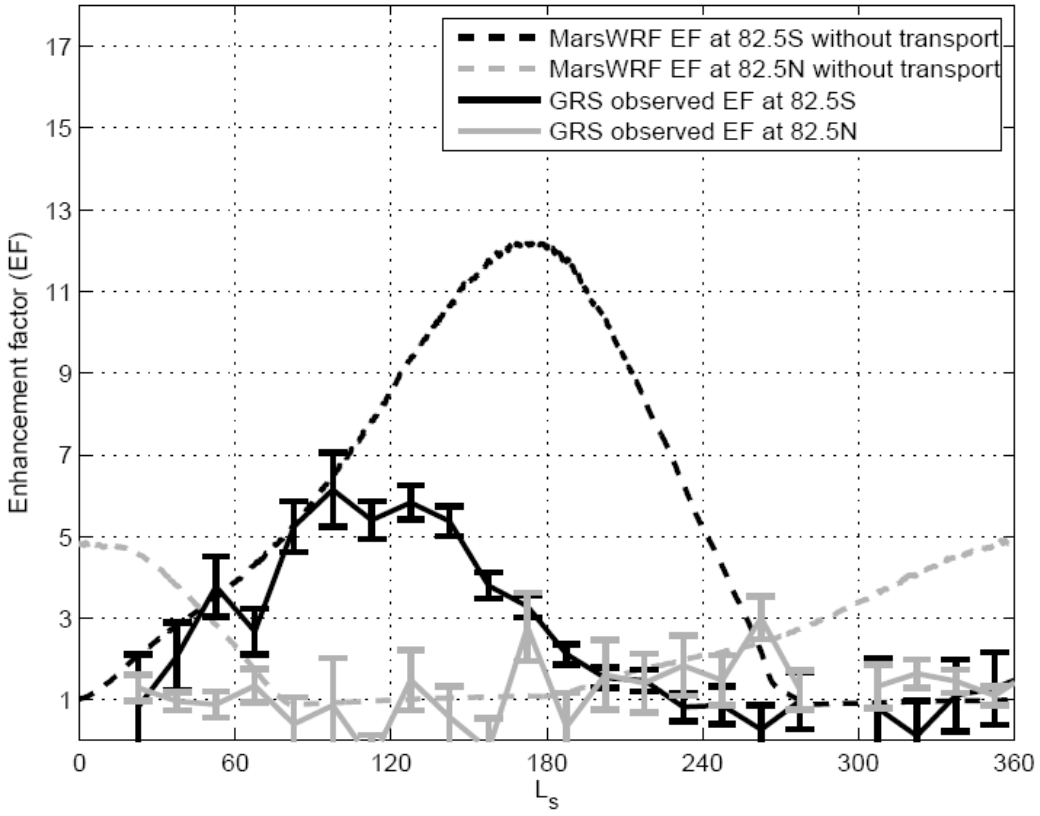

Figure 5.7: EF annual variation at high latitudes. Dashed lines: EFs of Ar at 82.5°S (black) and 82.5°N (grey) if there is no meridional transportation. i.e. for any amount of CO_2 ice deposited on the surface, the mass of Ar left in the atmosphere is proportional to the mass of the newly formed CO_2 frost. The ratio is preset to the mass mixing ratio given by VL data (1.45%). Solid lines with errobars: EFs of Ar at 82.5°S (black) and 82.5°N (grey) given by GRS observations calibrated with MarsWRF outputs.

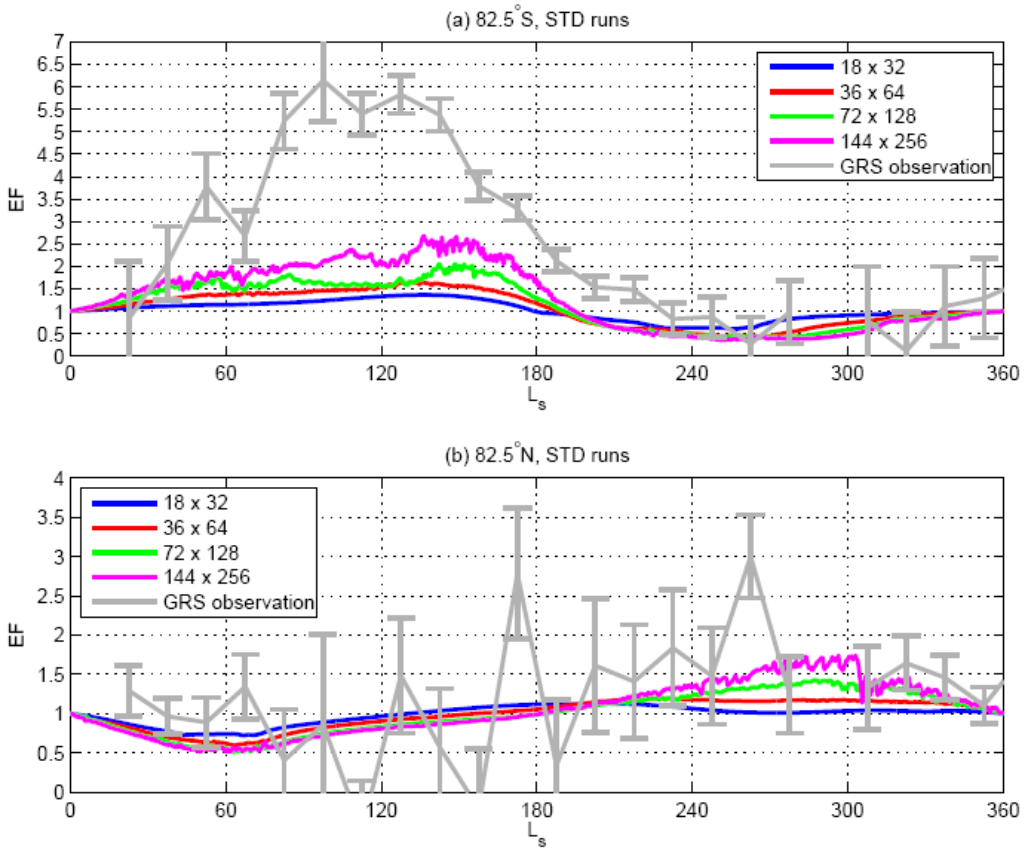

Figure 5.8: EFs at 82.5°S (upper panel) and 82.5°N (lower panel) produced by MarsWRF using the standard cylindrical map projection with the same vertical resolution (40 layers) but different horizontal spatial resolution. Blue: horizontal resolution is 18 (south-north) × 32 (east-west), or half of the standard resolution; red: 36 × 64, the standard MarsWRF setup; green: 72 × 128; purple: 144 × 256. Grey curves with errorbars: GRS measured EFs, calibrated with MarsWRF standard run surface pressure data.

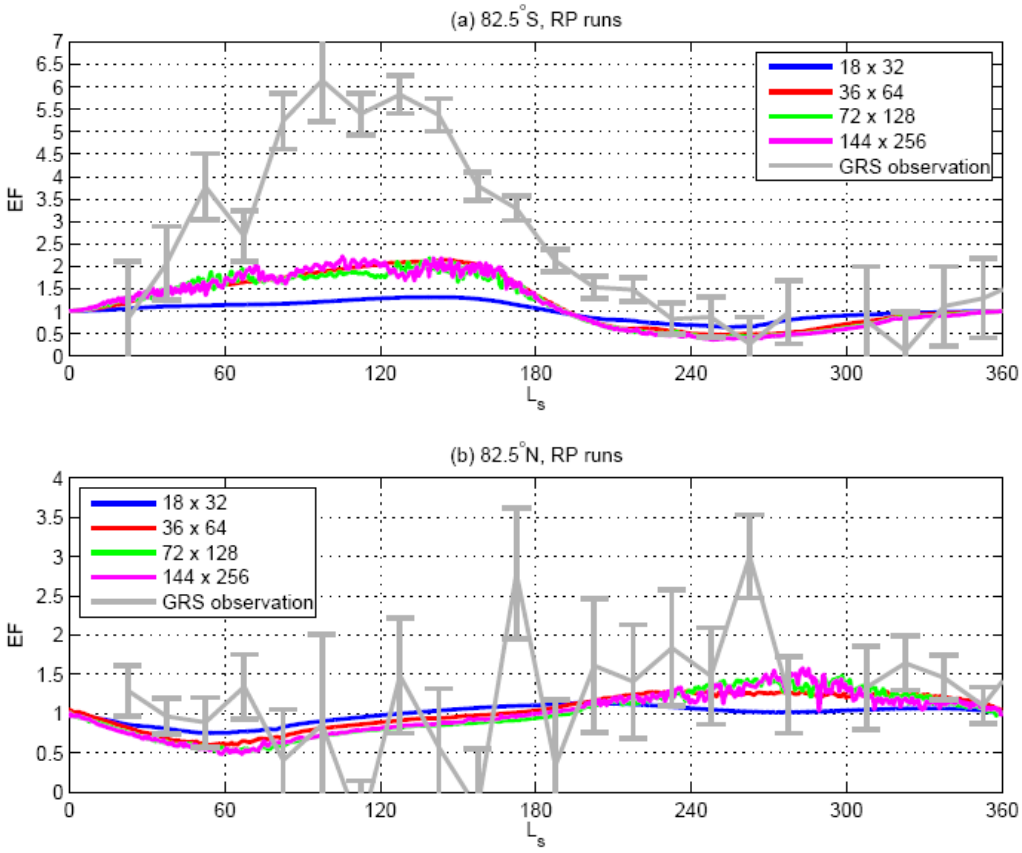

Figure 5.9: Same as Figure 5.7, except that MarsWRF is run in the "rotated pole" mode. MarsWRF data used to calibrate GRS measurement is the same.

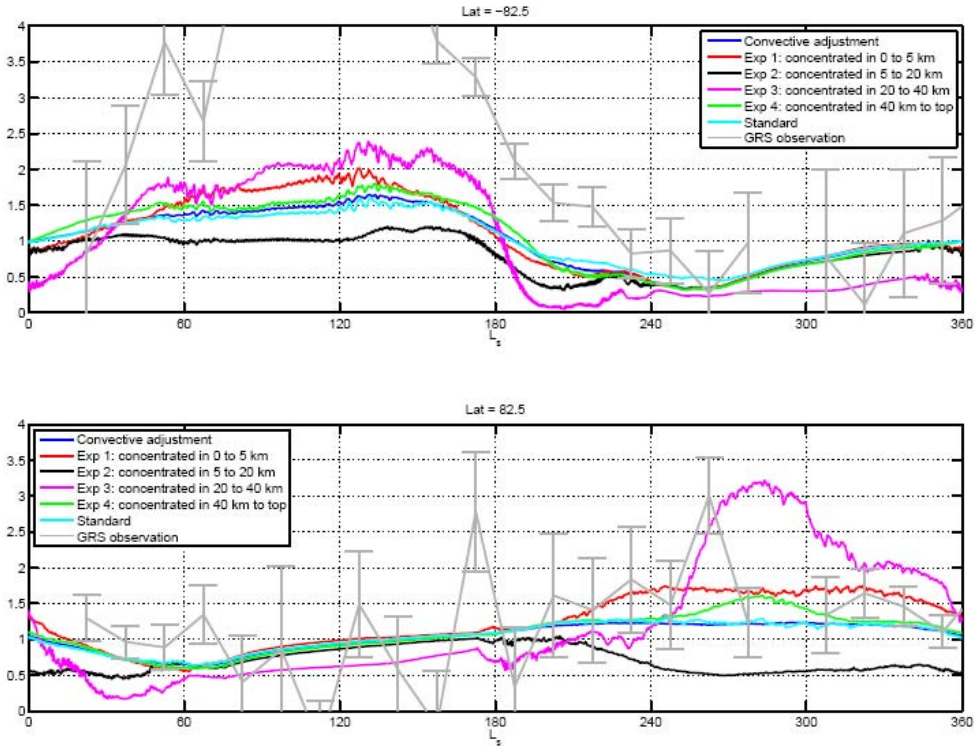

Figure 5.10: Same as Figure 5.8, different colors are for different experiment setup. Blue: with convective adjustment, Ar distributed evenly through the vertical column; red: exp 1, Ar concentrates between 0 to 5 km (layer 1); black: exp 2, Ar concentrates between 5 to 20 km (layer 2); purple: exp 3, Ar concentrates between 20 to 40 km (layer 3); green: exp 4, Ar concentrates between 40 km to model top Ar (layer 4); light blue: standard vertical distribution, Ar concentrated near the surface. Grey curves with errorbars: GRS measured EFs, calibrated with MarsWRF standard run surface pressure data.

Chapter 6: Modeling the CO_2 ice clouds

Abstract

In certain environments, CO_2 gas becomes dry ice crystals in the atmosphere of Mars. Consequently formed dry ice clouds may later precipitate to the ground, if not re-sublimate completely on the way down. In terms of mass and energy exchange, the atmospheric deposition/sublimation is seemingly trivial compared to the phase change at the surface, which predominately controls the seasonal CO_2 cycle. Albeit their direct impact seems small, CO_2 clouds may be important in altering the radiative transfer and the air dynamics, therefore having larger influence on the climate of Mars. Meanwhile, the Mars sciences have matured to a stage such that sophisticated modeling and experimental work of the microphysics process of CO_2 ice is on high demand. Some GCMs have already initiated the inclusion of corresponding treatments. In this chapter, I present my attempts to include microphysical calculations for CO_2 ice cloud formation to MarsWRF. The inherited microphysical model takes various nucleation and accumulation mechanisms into account and computes the ice particle growth rate for different atmospheric conditions. For each grid cell in the model atmosphere, I use discrete size bins to characterize the distribution of ice particles. This procedure could potentially be useful to future radiative transfer models and surface microphysics models. Preliminary results show promising agreements with spacecraft observations.

6.1 Introduction

The discovery of CO_2 ice clouds dates back to the Mariner's era when spectral signature of CO_2 ice was found in the upper atmosphere of Mars [*Herr and Pimentel*, 1970]. Subsequent space missions have provided both direct and indirect evidences for its existence in the Martian atmosphere [*Neumann et al.*, 2003]. Since then, many physical phenomena on Mars have been attributed to the CO_2 ice clouds. For example, CO_2 ice was thought to be closely associated with the energy cycle. In earth's atmosphere, radiative effect of clouds and aerosols is an important contributor to the energy balance. Unfortunately, it is also the most uncertain part because of complicated feedbacks in the earth system. In the current climate of Mars, direct radiative effects of CO_2 ice clouds may be too small to make a global impact. Nonetheless, it may alter the atmospheric dynamics by providing energy to vertical convections [*Colaprete et al.*, 2008] and contribute to the energy cycle by modifying the (effective) surface emissivity [*Byrne and Ingersoll*, 2003; *Colaprete et al.*, 2005; *Guo et al.*, submitted-b; *Kieffer et al.*, 2000]. Moreover, CO_2 cloud formed in ancient Martian atmosphere may introduce greenhouse effects significant enough to allow the existence of liquid water on the surface of Mars [*Colaprete and Toon*, 2003; *Mischna et al.*, 2000].

Atmospheric CO_2 condensation usually happens in extremely cold condition, which makes passive infrared detection difficult. Active measurements such as LIDAR detection are not as plenty due to the limitations in deep space mission instrumentation. Microphysics models and laboratory experiments therefore become important alternatives. Many GCMs have started to incorporate microphysics module to simulate CO_2 cloud formation [*Colaprete and Toon*, 2002; *Tobie et al.*, 2003]. To avoid computation complexity, the air grid is usually characterized with a single ice particle size, or a few moments (e.g. the mean and the

standard deviation) to describe the size distribution and to aid subsequent radiative calculations.

I adopt the microphysics models developed by *Wood* [1999] and integrate them to MarsWRF. Instead employing a few moments to describe the size distribution of ice particles, 15 size bins are used to cover particle sizes ranging from 10^{-10} m to 10^{-2} m with number density information. This setup should be useful to future radiative transfer and surface microphysics calculations. Although the work is still at its preliminary stage, promising results have already been generated.

I provide a brief overview to the CO_2 microphysics models in section 6.2. Section 6.3 and 6.4 present the preliminary model results from 1D and 3D simulations, respectively. Summaries and discussions of this chapter are given in section 6.5.

6.2 Microphysics model

Most of the theoretical details of the nucleation model and the particle growth model can be found in *Wood* [1999] and the literatures referred in that work. A similar nucleation model have also been discussed by [*Maattanen et al.*, 2005]. Selected background information is provided to help the reader of this dissertation to understand relevant physics concepts and model implementation.

6.2.1 Nucleation

There are three potentially active nucleation mechanisms in the atmosphere of Mars: homogeneous nucleation, heterogeneous nucleation and ion nucleation. Homogeneous nucleation refers to the formation of ice particles directly from the vapor phase. It usually requires several hundred percent of super-saturation[7]. Heterogeneous nucleation, which involves a foreign substrate as the nucleus, generally requires much smaller super-saturation ratio, but the value depends critically on the nature of the condensate-substrate interface. Icon can also promote nucleation by forming small clusters of vapor molecules bounded by electrostatic force which allows nucleation at super-saturations typically intermediate to those required for homogeneous nucleation and heterogeneous nucleation. However, ion distribution is neither modeled nor prescribed in MarsWRF. I simply ignore the ion nucleation in the following discussion.

For an environment that the partial pressure of the (CO_2) vapor and the ambient temperature are known, the equilibrium pressure is decided. The homogeneous nucleation rate (J_{hom}) and the size of the cluster (r^*) can therefore be determined. The free energy of formation of a spherical cluster of molecules with radius r is given by

$$\Delta F_{\text{hom}} = (-4\pi r^3 / 3\Omega)\, kT \ln S + 4\pi r^2 \sigma, \qquad (6.1)$$

where Ω is the molecular volume in the condensed phase, k is the Boltzmann constant, T is the temperature, S is the saturation ratio and σ is the surface energy. The critical radius r^* of

[7] Saturation ratio S is defined as $S = P_v/P_{v,eq}(T)$, where P_v is the partial pressure of the vapor, $P_{v,eq}(T)$ is the equilibrium vapor pressure over a float condensate surface at ambient temperature T. Super-saturation, s, is the saturation exceeding unity, i.e., $s = S - 1$.

the nucleus, beyond which the free energy decrease therefore favors growth, is derived by taking the derivative of the right hand side of Equation 6.1 and set it to zero:

$$r^* = 2\Omega\sigma / kT \ln S. \tag{6.2}$$

The corresponding critical free energy is

$$\Delta F^* = 16\pi\Omega^2\sigma^3 / 3(kT \ln S)^2. \tag{6.3}$$

The homogenous nucleation rate, which has a unit of $m^{-1}s^{-1}$, is given by

$$J_{\text{hom}} = \xi 4\pi r^{*2}(RT / 2\pi M_v)^{1/2} (\Delta F^* / 3\pi kTn^{*2})^{1/2} f_{\delta T} N_v [N_v \exp(-\Delta F^* / kT)], \tag{6.4}$$

where ξ is the sticking coefficient (taken to be 1), or probability that an impinging condensate molecule will stick to the critical nucleus, M_v is the molecular weight of the vapor, n^* is the number of molecules in a critical cluster, $f_{\delta T}$ is a unitless factor that accounts for the fact that the nucleus is not isothermal, N_v is the number density of the molecule in the vapor phase.

If the size, shape (assumed to be spherical) and number density of the substrate (usually assumed to be aerial dust) is also provided, one can calculate the heterogeneous nucleation rate by

$$J_{\text{het}} = 4\pi(r_{\text{CN}})^2 (ZRTdr^* \sin\theta / fvM_v) f_{\delta T} N_{\text{CN}} (N_v)^2 \exp[(2\Delta F_{\text{des}} - \Delta F_{\text{sd}} - f\Delta F^*) / kT], \tag{6.5}$$

where r_{CN} is the radius of the foreign substrate, Z is the Zeldovich factor defined as $Z = (\Delta F^* / 3\pi kTn^{*2})^{1/2}$, d is the mean jump distance of an adsorbed molecule, θ is the contact angle between the angle and the nucleus, v is the vibration frequency of the adsorbed molecule, N_{CN} is the number density of the condensation nuclei (taken to be the number density of dust

grains), ΔF_{des} and ΔF_{sd} are the free energies of activation of desorption and surface diffusion respectively, f is a factor defined by

$$f = 1/2 + 1/2\,[(1 - Xm) / g]^3 + 1/2\,X^3\,[2 - 3(X - m) / g + [(X - m) / g]^3] + 3/2\,X^2 m[(X - m) / g - 1], \quad (6.6)$$

where $g = (1 + X^2 - 2Xm)^{1/2}$, $X = r_{CN} / r^*$, and $m = \cos\theta$. Heterogeneous nucleation is only favored when $r_{CN} > r^*$. The net nucleation rate is a combination of J_{hom} and J_{het}.

6.2.2 Particle growth

The nucleation model provides the size and number density of the nuclei. Subsequent crystal particle growth model determines how fast the CO_2 ice accumulates to the nuclei, with information of the ambient temperature, pressure and saturation ratio. There are two potential crystal growth mechanisms: two-dimensional nucleation and screw dislocation growth, each providing different kinetic coefficients for different growth rate, which are probably the upper and lower bounds for a given super-saturation. Figure 6.1 shows the evaporation and condensation rates with the two assumptions (with units of $\mu m/s$) for a given atmospheric pressure, vapor mixing ratio, and nucleus size. The growth rate is considered a function of the super-saturation ratio s (in this case, a function of temperature) and a small change in s may results in big change in the growth rate. There are limitations to the growth model. For instance, the shape of the snow flakes on Mars remains largely unknown and we assumed them to be spherical, which is obviously not the case for earth. Such assumption simplifies the growth model and may provide practical information for potential radiative calculations. The actual growth mechanism in the Martian atmosphere, single ledge or two-

dimensional, is unknown. Practical compromise was given to the single ledge nucleation since it is activated a much lower super-saturation ratio. Finally, the model only predicts accurate evaporation rate at certain atmospheric conditions. In the other environments, arbitrary evaporation rate values have to be assigned according to the super-saturation. Fortunately, for any supers-saturation ratio less than zero, relatively fast evaporation can be assumed. Meanwhile, coagulation is completely ignored.

There are mass and latent heat exchanges involving with the CO_2 phase exchange, which have the potential to modify the temperature, pressure, and super-saturation of the atmospheric grid. As evidently shown in Figure 6.1, the growth rate is very responsive to the super-saturation. A slight change in super-saturation may result in a sizeable change in growth rate, even from condensation to evaporation. Therefore, I utilize an iterative method to support a dynamically adaptive computation for the particle growth in a GCM time step (180 seconds for standard MarsWRF simulations). The growth rate is first assumed to be valid for the entire time step, after which it is recalculated. If the new growth rate is significantly different from the old one, meaning the atmospheric condition is heavily modified if the assumption is true, I reduce the time scale to a third of the original and see how big the difference is. When the change of the growth rate is acceptable (less than some pre-decided threshold), I update the size of ice particle, the pressure and temperature of the atmosphere and repeat the procedure for the remaining of the time step.

6.2.3 Species array

In the physical world, there are probably only three kinds of solid particles in the atmosphere of Mars: dust grains, CO_2 ice crystals and water ice crystals (latter two very likely with dust cores, water ice is ignored in this chapter). For 3D numerical simulations, there are more "species" involved with CO_2 ice physics conceptually: aerial dust particles which also have the potential to become condensate nuclei and accumulate CO_2 ice; ice crystals which is comprised of two species: pure CO_2 ice and the dust core. In MarsWRF, these four species (dust, nuclei, ice, and core) are described by species arrays, each containing 15 elements. Each element of a given species array indicates the mass mixing ratio for particles of the corresponding size. When the atmosphere is super-saturated, the nucleation driver transfers the dust particles of associated sizes to the array of "nuclei". The growth model then calculates how much ice is accumulated to the nuclei. The amount of accumulated ice is passed to the "ice" array and the mass of the dust is passed to the "core" array. Notice the "ice particle as a whole" can be new nuclei and should be used in the growth calculation, therefore the mass of ice and core was made separately additive. Ice particle growth/evaporation requires rearrangement of the "ice" array and "core" array. Consequently, core of multiple sizes may end up in ice particles of a same size. Keeping track of that information (core size) is too expensive computationally. Therefore, only the mass in the "core" array is recorded. When evaporation drives the CO_2 ice away completely, the mass in the "core" array is redistributed to the "dust" array assuming a log-normal size distribution with a mean radius of 2 microns [*Newman et al.*, 2002a].

Atmospheric circulation and precipitation will potentially modify the species arrays in both the horizontal direction and the vertical direction. The utilization of the size bins will

provide precise information about the size distribution of dust and ice in a given atmospheric grid cell. It slows down the GCM integration significantly, but contains the required information for subsequent calculations, such as radiative transfer and surface microphysics.

The species arrays have not yet been coupled with the current atmospheric transport driver or sedimentation driver yet due to their incompleteness. Nor are the radiative and surface microphysical effects of the CO_2 ice cloud included. The Richardson research group is currently working closely with NCAR on higher quality numerical methods for these simulations.

6.3 1D simulation results

MarsWRF is setup to perform 1D simulation without atmospheric circulation at 60°N. Surface energy balance is removed from this run because the lack of sensible heat and mass input from the lower latitude will cause the atmosphere to collapse completely in winter. Radiative forcing drives the annual cycle of atmospheric temperature and pressure. The dust climatology for radiative transfer calculation is parameterized according to spacecraft measurement. A separate "dust" array which assumes the role of the potential nuclei is initialized with a column integrated optical depth of 0.1, assuming the dust's mass decreases exponentially with pressure and has a log-normal size distribution with 2 micron mean size. The modeled atmosphere has 25 layers. Once formed, the ice particles are suspended at the location of the formation. Obviously, this simulation is merely a showcase for different behaviors of the microphysics driver in various atmospheric conditions rather than an attempt to reproduce the actual atmosphere.

Model results are shown in Figure 6.2 and 6.3. Figure 6.2 presents some relevant annual cycles. Panel (a) shows the annual cycle of the temperature, panel (b) shows the super-saturation ratio in the atmosphere, and panel (c) shows the mass mixing ratio of CO_2 ice. CO_2 ice starts to form when the atmosphere becomes super-saturated (super-saturation ratio is positive). The formation process is fast and very responsive to super-saturation ratio. The ice abundance gets as high as 10% of the current amount of atmospheric weight. It seems that lower super-saturation ratios are required for the formation of ice particles in the lower atmosphere. CO_2 ice crystals do not completely disappear until the air is rather warm, suggesting a very small saturation is sufficient to maintain the existence of ice crystals once they have formed.

Panel (c) of Figure 6.3 shows the annul cycle of surface pressure, which is an indication of the total CO_2 gas in the atmosphere. Because of the removal of the CO_2 exchange at the surface, the surface pressure does not change until atmospheric condensation activates. When the condensation starts in higher atmosphere, the decrease of surface pressure is slow. As soon as CO_2 begin to condense in the lower atmosphere, a quick and large drop in surface pressure can be found. In a hydrostatic atmosphere, pressure is higher at lower altitudes. Same mass mixing ratio at different pressure level corresponds to different mass. For instance, ice mass mixing ratio at in layer 13 has similar maximum as in layer 23, however, the corresponding mass is very different. This is why the pressure drop associated with lower altitude phase change is much larger.

Panels (a) and (b) of Figure 6.3 present some snap shots of the “dust” arrays and the “ice” arrays at different altitudes at Ls 300°, well into the northern winter. For layers 23, 18 and 3, the “dust” arrays maintain the log-normal distribution, suggesting in these layers the

particle growth is not intense enough to change the ice crystal size significantly due to the relatively small super-saturation. Dust particles smaller than 10^{-4} m are almost absent in layer 8 and 13, indicating much stronger particle growth moves the dust grains to larger size ice crystals. The "ice" arrays show interesting distribution. The ice particles are either very large (~tens of microns to tenths of millimeters) or very smaller ($<10^{-8}$ m). Recall that I have not considered precipitation (or "snowing") in this experiment. If proper treatment for sedimentation is included, large ice particles are possible to fall to the ground while tiny ones may hang in the air. The larger ones are not very likely to reform due to the lack of condensation nuclei, unless some other mechanisms replenish the aerial dust at heights.

Further simulations show that the total mass of CO_2 ice formed, or equivalently the maximum decrease of surface pressure, is rather sensitive to the assigned background dust abundance. Double the "dust" array causes roughly twice the CO_2 ice mass increase or twice the surface pressure decrease throughout a Martian year. It suggests that for this setup, the cloud formation is still far from "saturation". Because the surface condensation process is absent in the simulation, the pressure is relatively high, resulting in relatively large super-saturation. When the much more hefty surface condensation is included, or the number of nuclei is large enough, the *in situ* pressure would change significantly, and the associated saturation ratio would have been strongly influenced, leading to different (probably reduced) nucleation rate and growth rate.

6.4 3D simulation results

This section shows the preliminary results of MarsWRF with CO_2 microphysics. The surface energy balance model is included in the 3D simulations, which guarantees the modeled atmosphere with more realistic pressure and temperature cycles. The "dust" array is prescribed and will not be replenished. Experiments in this section are designed for the exploration of possible distribution and morphology of CO_2 clouds in the Martian atmosphere. It costs about 24 hours on 16 CPUs for MarsWRF to integrate one Martian year without the CO_2 microphysics driver. When the microphysics module is included, the simulation is about seven times slower.

6.4.1 Control case

Figure 6.4 shows an instantaneous map of the CO_2 ice in layer 15 at Ls 107.37°, when the southern hemisphere is in winter. CO_2 ice cloud contains a few percent of the atmospheric mass and completely covers the southern polar region up to 50° S. The boundary of the cloud roughly follows the critical temperature contour. Higher concentration of ice tend to focus on higher latitudes, where the temperature is the lowest, though some patchy highs can be found near 60° S, which may be related to wave activities.

Figure 6.5 provides a zonal view of the CO_2 ice and temperature for the same time step. There seems to be two "cloud decks" over the southern pole. The lower cloud deck peaks at 3 to 4 km above the surface, extends to 60° S, and is probably associated with the low temperature induced by the surface frost coverage. The higher one concentrates at 10 to

11 km above the surface and is mostly confined to 75° S and pole-ward, which seems to be associated with a temperature low at that location.

Figure 6.6 shows the CO_2 ice map in layer 15 at northern winter. Northern winter is in general warmer than the southern winter because of the thicker atmosphere, which does not favor the formation of the CO_2 ice cloud. Cloud coverage is not continuous for the northern winter sky and the concentrations are slightly lower (negative values are due to the imperfections of the numerical Fourier filters and should be discarded). The zonal average (Figure 6.7) suggests that the northern winter cloud is thinner than its southern counterpart. It is mostly confined to the surface because the atmospheric temperature is 20 K warmer than the southern winter.

Direct detection for CO_2 ice cloud is very scarce. Mariner 6 and 7 first returned spectral evidence for solid CO_2 in the upper atmosphere of Mars [*Herr and Pimentel*, 1970]. The Mars Orbiter Laser Altimeter (MOLA) instrument received echo from above the Mars surface and attribute the strong and brief reflections to the CO_2 snow events [*Ivanov and Muhleman*, 2001; *Neumann et al.*, 2003]. The Mars Climate Sounder (MCS) also detected aerosols in the polar sky that can not be explained by dust or water ice grains [*Heavens*, personal communication]. The latitudes and altitudes of the ice clouds reported by MOLA and MCS are consistent with MarsWRF predictions.

6.4.2 Higher obliquity

The secular perturbations of all other planets in the Solar System causes the orbit of Mars to change chaotically [*Laskar*, 1990]. Different orbital parameters, including spin axis

obliquity and eccentricity result in different surface insolation annual variation [*Laskar et al.*, 2002] and modifies the climate. We experiment with a higher obliquity (40°) assuming its change would not cause any other boundary conditions in MarsWRF to vary. We also assume the eccentricity of the orbit of Mars remain the same in these experiments.

Figure 6.8 shows the atmospheric CO_2 ice distribution in the southern winter. With higher planetary obliquity, the polar winter night reaches to lower latitudes. As a result, the cloud coverage extends to lower latitudes. The boundary of the clouds shows a good correlation with the atmospheric temperature contours. On average, the concentration seems similar to the control case in this layer, but the maximum value is higher. When viewed in zonal average (Figure 6.9), the clouds maintain the "two deck" structure. Both decks extend to lower latitudes with higher abundance, while the lower concentration levitates to 10 km above the surface. These changes can be tied to the extension of cold regions in the high obliquity case.

In the northern winter, the clouds show similar pattern of change, i.e. advancing to lower latitude with higher abundance. In addition, one can find small amount of ices developing 20 km above the surface in the equatorial region and over the south pole. The equatorial clouds seem to be correlated with a temperature low while the southern polar reservoir may have developed due to the thermal wave induced high super-saturation.

6.5 Summaries and discussions

I incorporated a state-of-the-art microphysics model to MarsWRF. The work is still in its preliminary phase and lots of compromises have yet been made. However, the model has

already worked mechanically and provided results that are physically sound. It is capable of generating seasonal cycle of CO_2 ice clouds and reasonable size spectrum of ice crystals. As expected, heterogeneous nucleation dominates the nuclei generation and the crystal growing processes responds very fast to the super-saturation, which is mostly driven by air temperature and pressure. Our simple 3D simulations show good agreement with spacecraft observation even without sedimentation and advection. It may suggest that the sedimentation is negligible in the Martian atmosphere, which is probably not true for larger particles, or the re-formation of ice crystals is very fast. The latter implication requires a fast nuclei replenish mechanism.

There is much to be done to improve the physicality of the cloud formation scheme. The most urgent task is to fix the sedimentation routine and the advection routine. Such effort would give us more confidence in examining the morphology and spatial variation of the clouds. As for the current model setup, the background dust is fixed in MarsWRF. This fixed dust species is used as the potential condensation nuclei. In this scenario, when a dust particle becomes the core of an ice grain and later precipitate to the ground, it is lost from the atmosphere from then on. This is an extremely naïve assumption. The actual dust cycle on Mars will obviously change with time and its size distribution may also differ from the log-normal shape. Research on the dust cycle itself is a challenging topic in the Mars science community. The simulated dust storms usually vanish later than what have been observed [*Newman et al.*, 2002b]. There is hypothesis that the early turn-off may be a consequence of the scavenge effect due to the CO_2 ice formation.

Ideally, we should couple the dust cycle with the CO_2 cloud cycle perfectly given good dust cycle driver and good transport driver. The real challenge arises when we bring

water ice on stage. Microphysics of water ice formation also requires dust particles as nuclei. As a result, the water ice will compete with the CO_2 ice for nucleus. Moreover, the water ice particle itself can be the nucleus for CO_2 ice formation, and vice versa, the CO_2 ice particle may be coded with water ice. Coupling these three species may be an extremely complicated and computationally expensive, yet in principal attainable.

The other important aspect of CO_2 ice cloud is its radiative effect. In the current climate regime, the direct radiative effects of the CO_2 ice clouds may be less intense compared to that of the tropical water ice cloud belt, because it concentrates mostly in the polar night, where incoming sunlight is the weakest. On the other hand, modification of surface ice albedo and emissvity due to CO_2 snow and surface microphysics may have profound impact to the energy cycle [*Guo et al.*, submitted-a] and may explain the existence of the residual CO_2 cap in the south pole [*Colaprete et al.*, 2005; *Guo et al.*, submitted-b]. The cooling or heating effect of CO_2 ice cloud may be more important for a denser Martian atmosphere [*Mischna et al.*, 2000]. The microphysics model is ideal for precise radiative calculation because it provides the size information along with the geographic distribution.

All the published CO_2 microphysics models have only been partially validated [*Maattanen et al.*, 2005; *Wood*, 1999]. As we mentioned earlier, direct detection of CO_2 ice cloud is scarce, so is the laboratory experiment to constrain the nucleation and growth model. This is a much harder task than writing down the physical formulations and may require another Ph.D. dissertation as a first attempt.

Figures

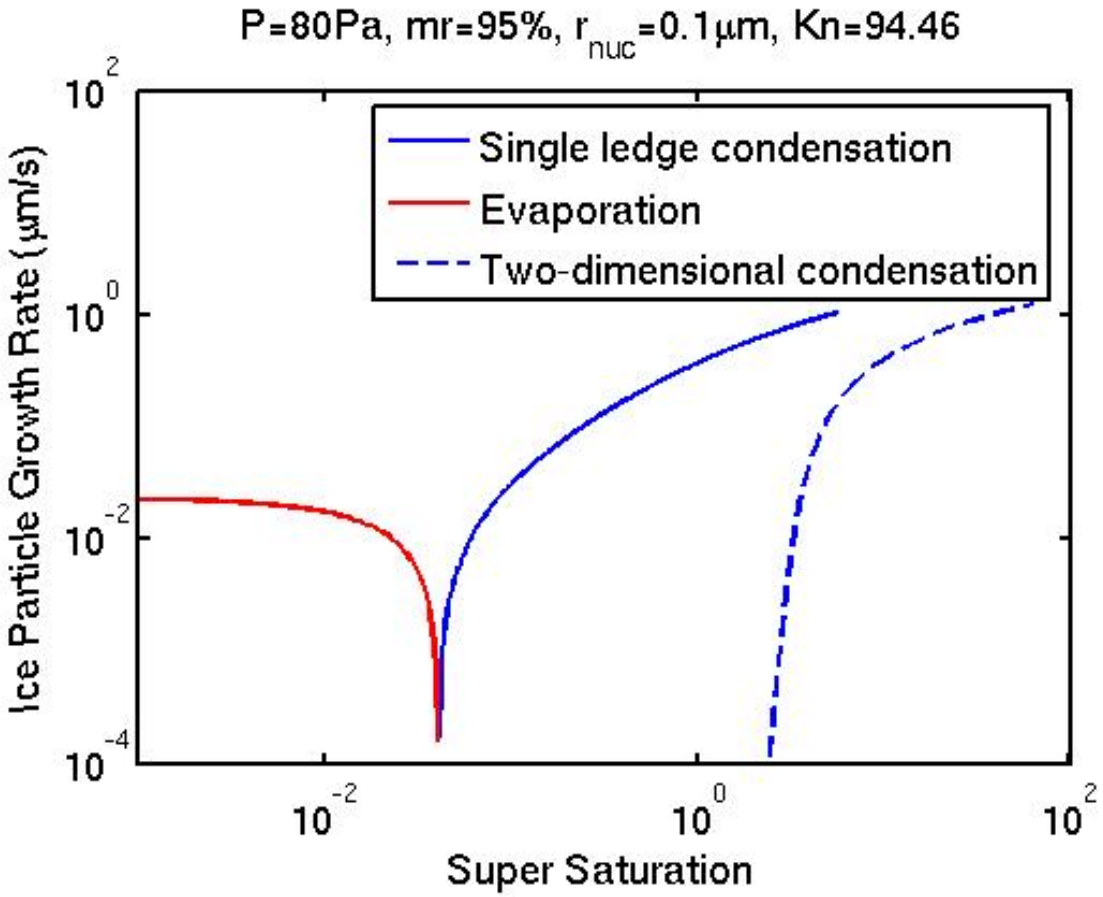

Figure 6.1: Ice particle growth rate for given condition, reproduction of Figure 8.7 in *Wood* [1999]. Ambient pressure is 90Pa, CO_2 vapor mixing ratio is 90%, size of the crystal is 0.1 micron.

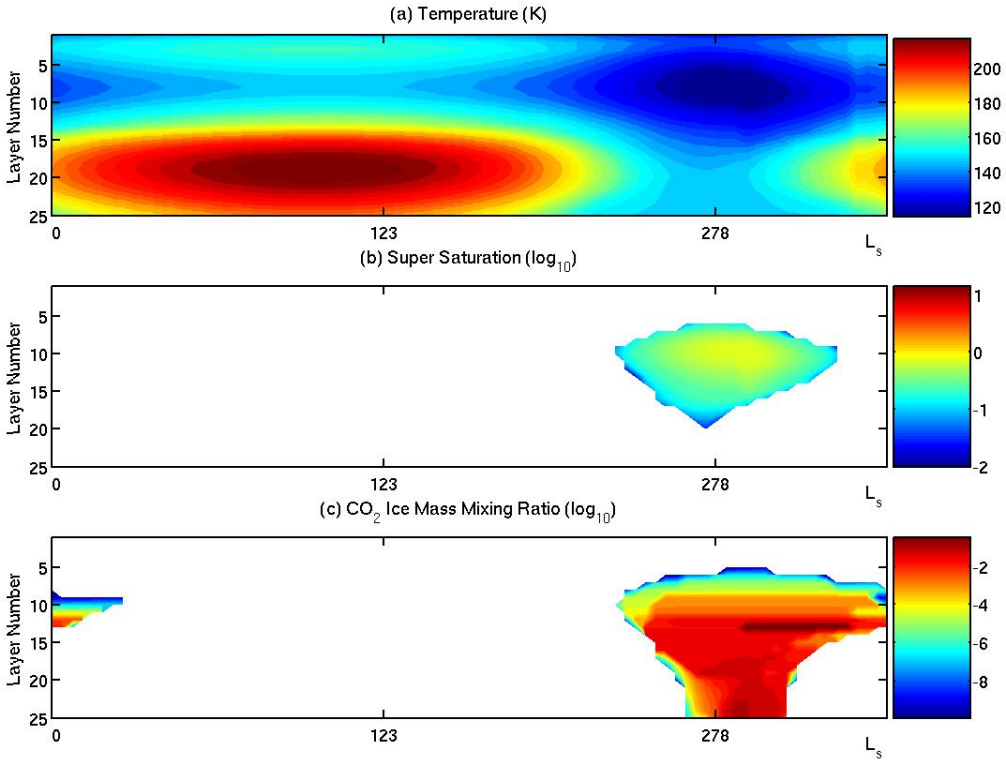

Figure 6.2: Annual cycles in the one dimensional MarsWRF at 60°N latitude. Panel (a): temperature annual cycle (layer number 25 is the closest to the surface); panel (b): super-saturation ratio annual cycle shown in log scale, truncated at 0.01; panel (c): CO_2 ice mass mixing ratio annual cycle shown in log scale.

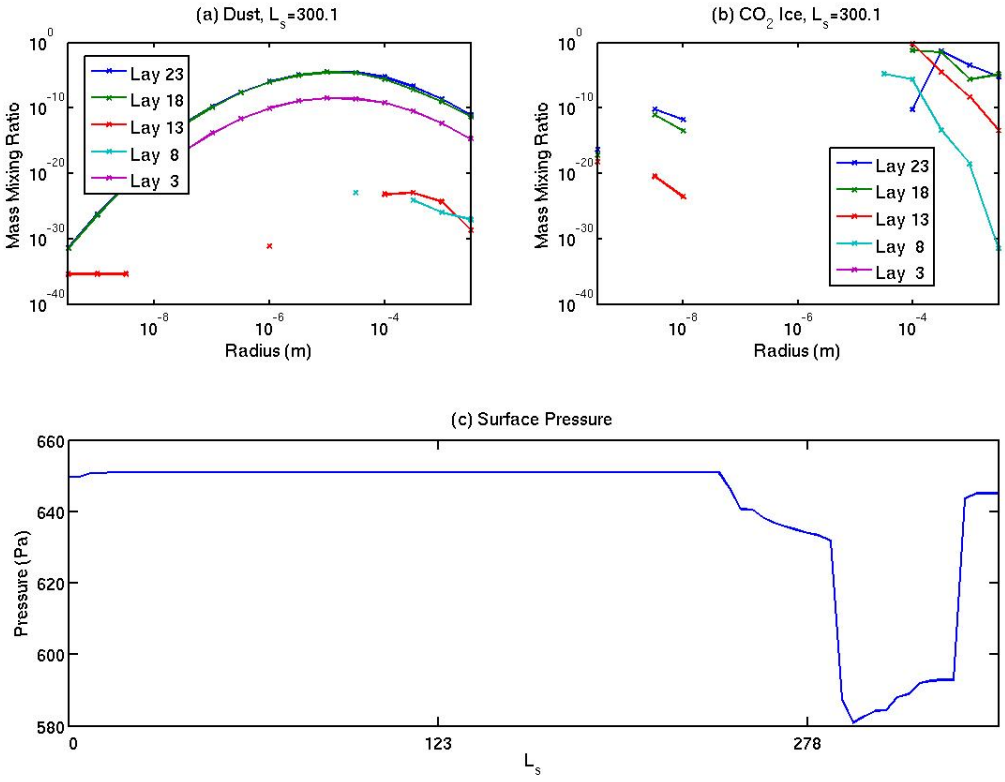

Figure 6.3: 1D simulation results. Panel (a): snap shot of the "dust" arrays at Ls 300° for different layers; panel (b): snap shot of the "ice" array; panel (c): surface pressure annual cycle.

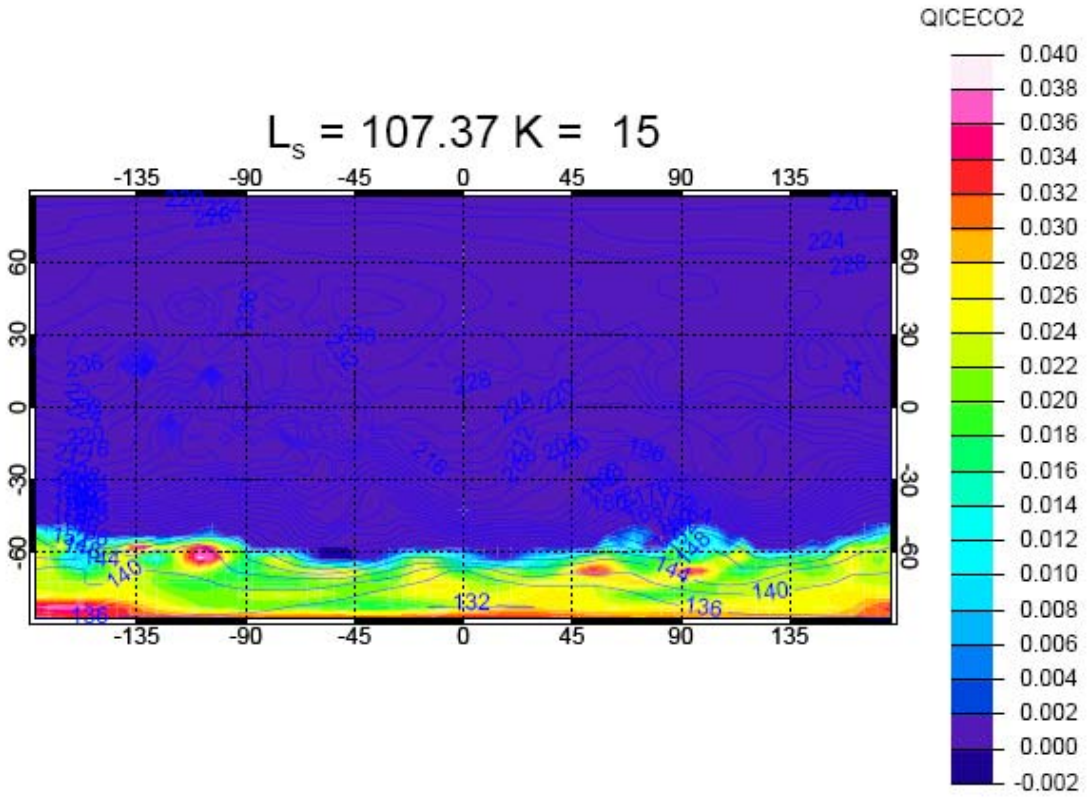

Figure 6.4: CO_2 ice cloud and atmospheric temperature distribution. The x axis shows the eastern longitude while the y axis shows the northern latitude. Color map shows an instantaneous mass mixing ratio map of the CO_2 ice at layer 15 at Ls 107.37°. Contour lines indicate the atmospheric temperature.

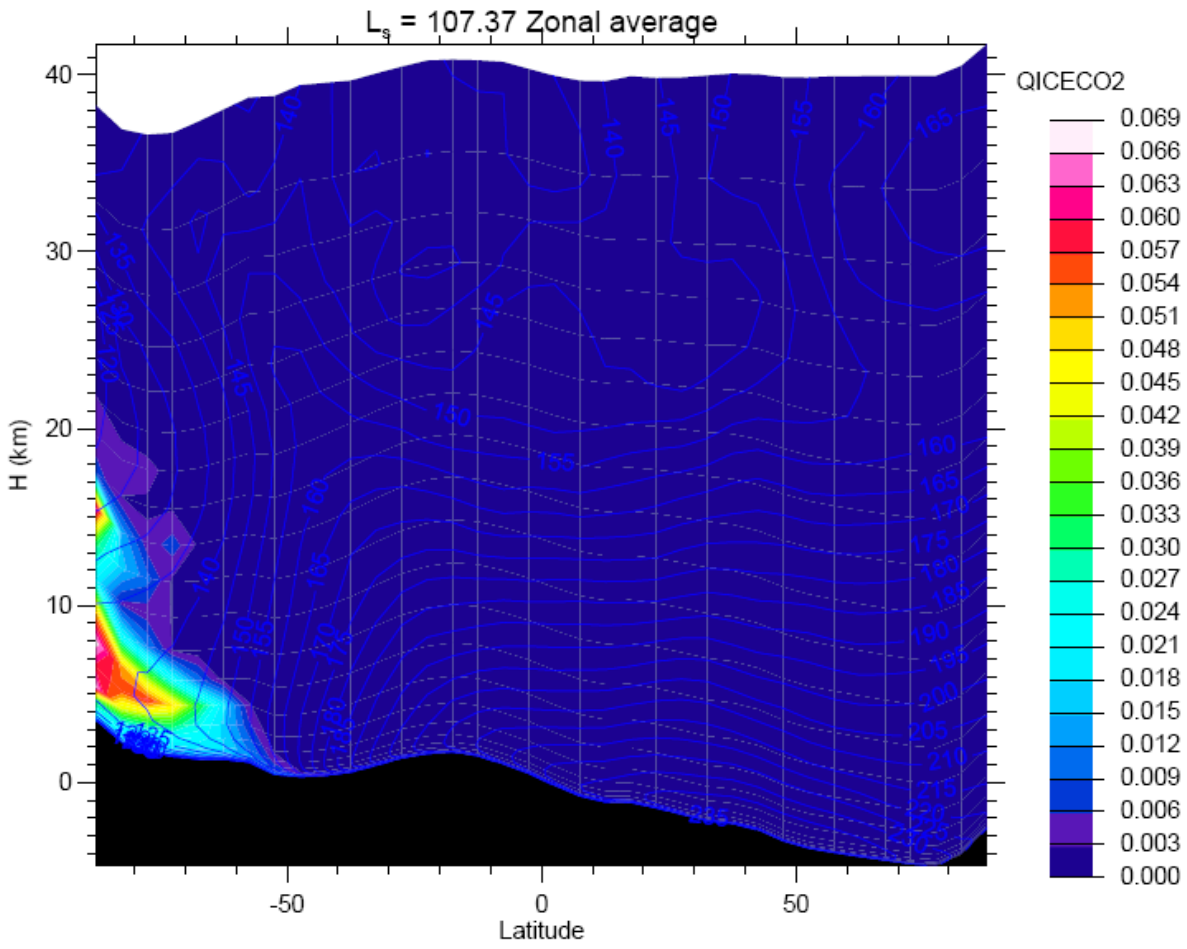

Figure 6.5: Zonal average of CO_2 ice mass mixing ratio and temperature at Ls 107.37°. The x axis shows the northern latitude and y axis shows the altitude.

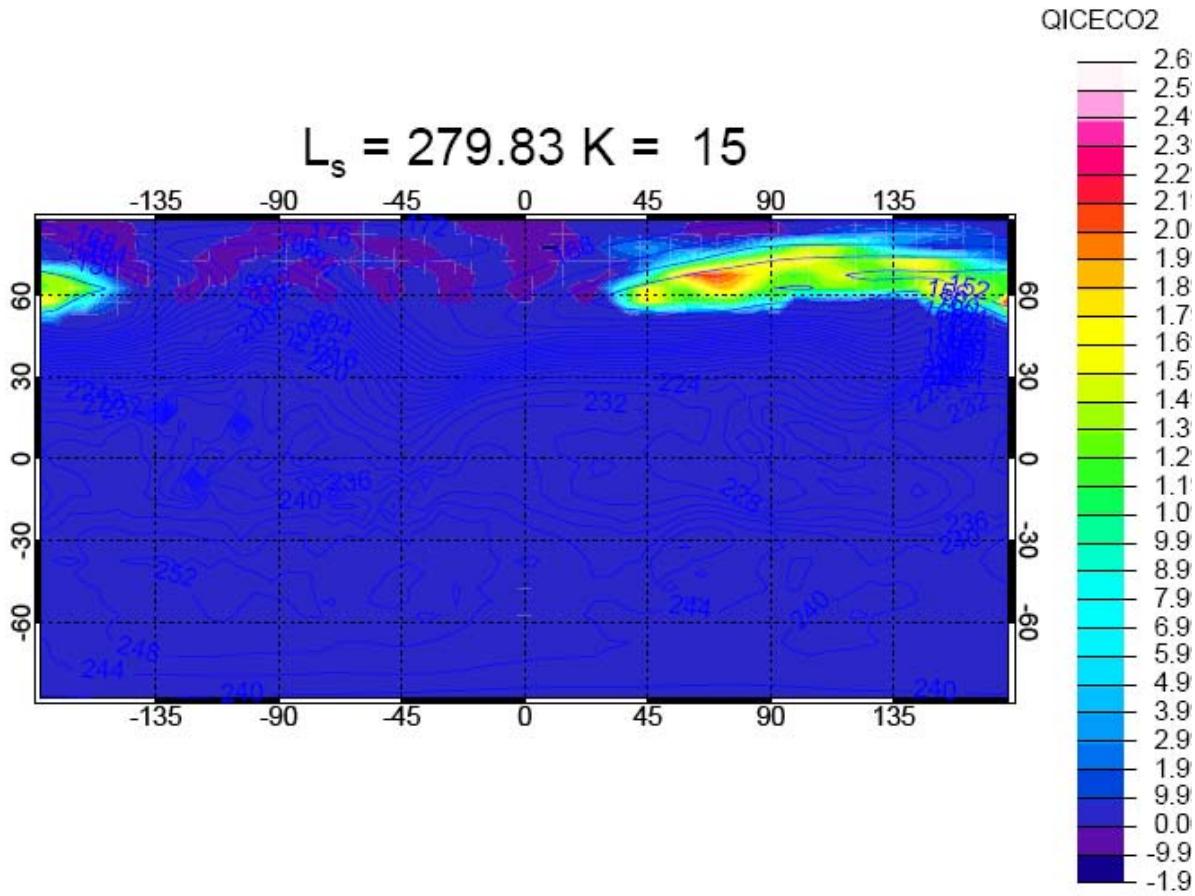

Figure 6.6: Same as Figure 6.4, except the time is at Ls 279.83°.

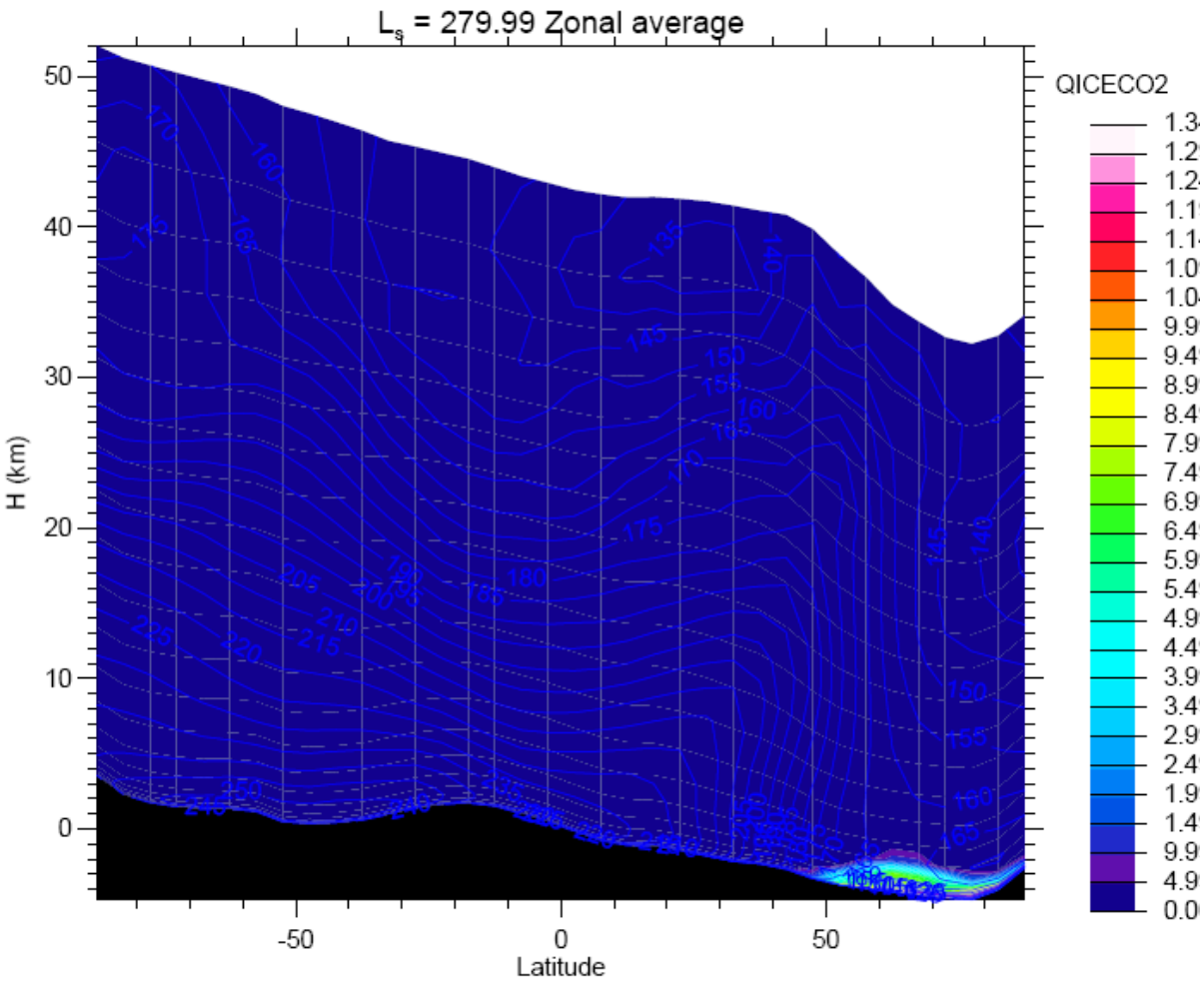

Figure 6.7: Same as Figure 6.5, except the time is at Ls 279.83°.

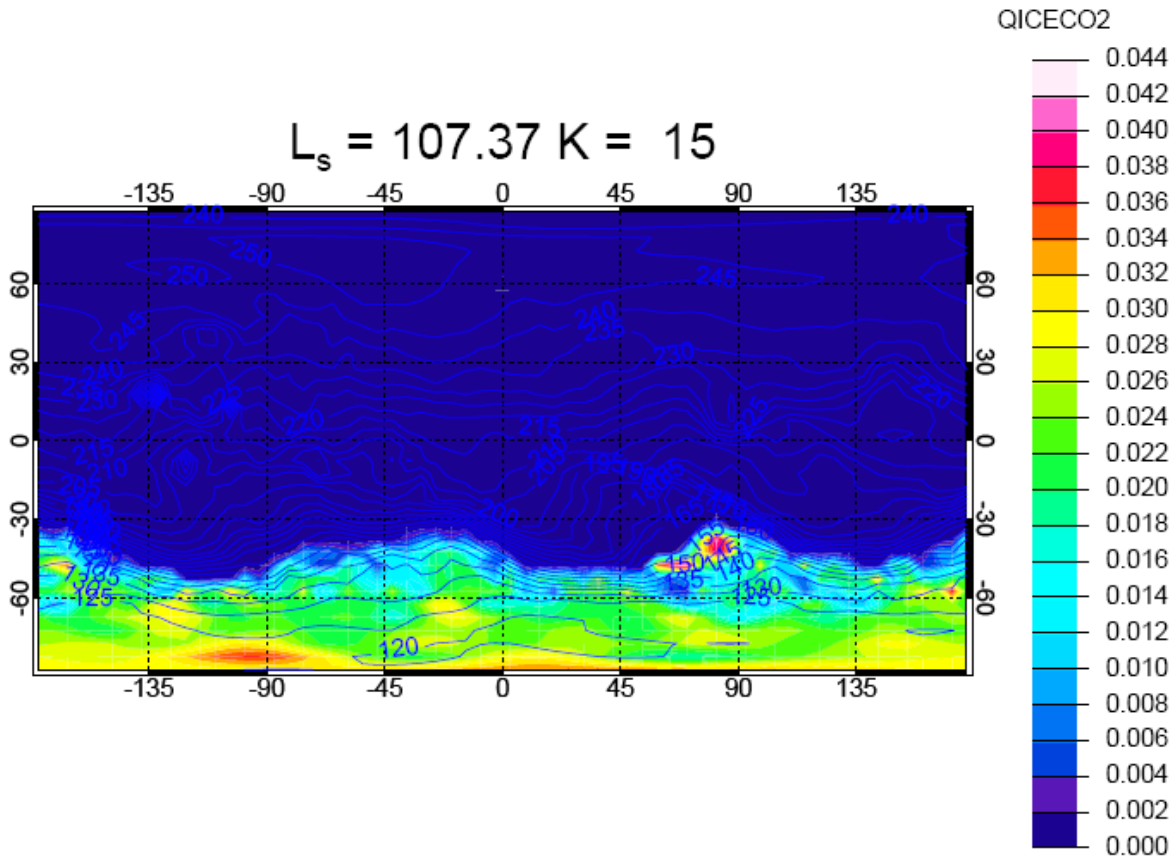

Figure 6.8: Same as Figure 6.4, except the obliquity of Mars is set to 40°.

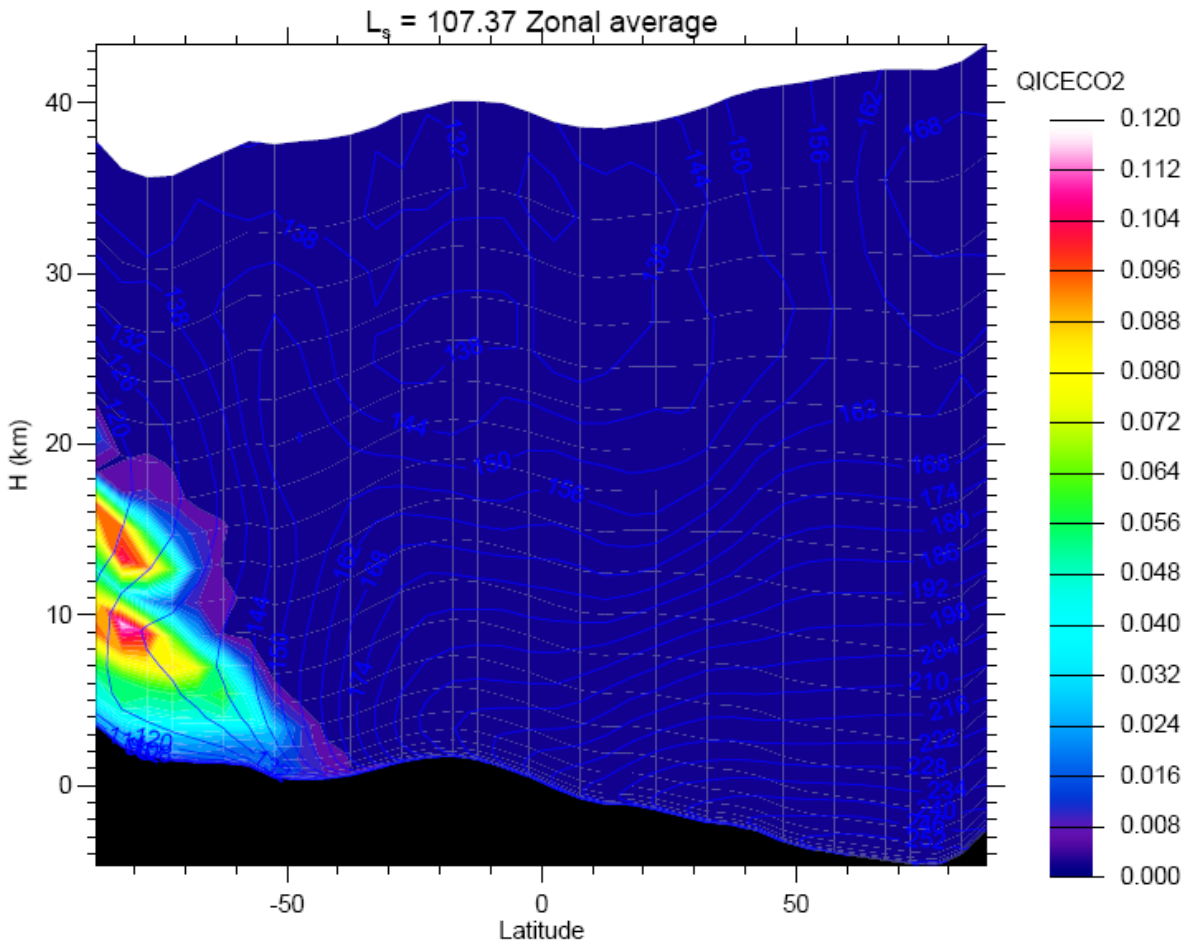

Figure 6.9: Same as Figure 6.5, except the obliquity of Mars is set to 40°.

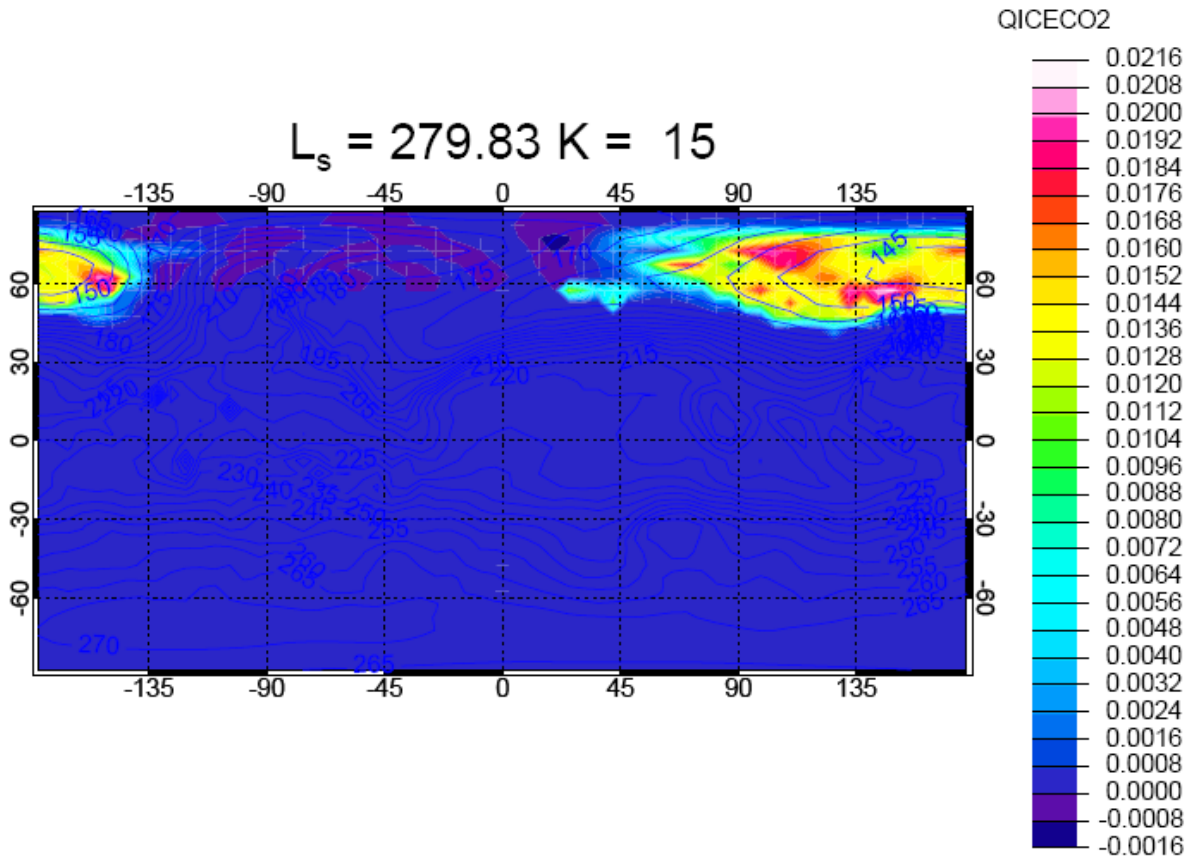

Figure 6.10: Same as Figure 6.6, except the obliquity of Mars is set to 40°.

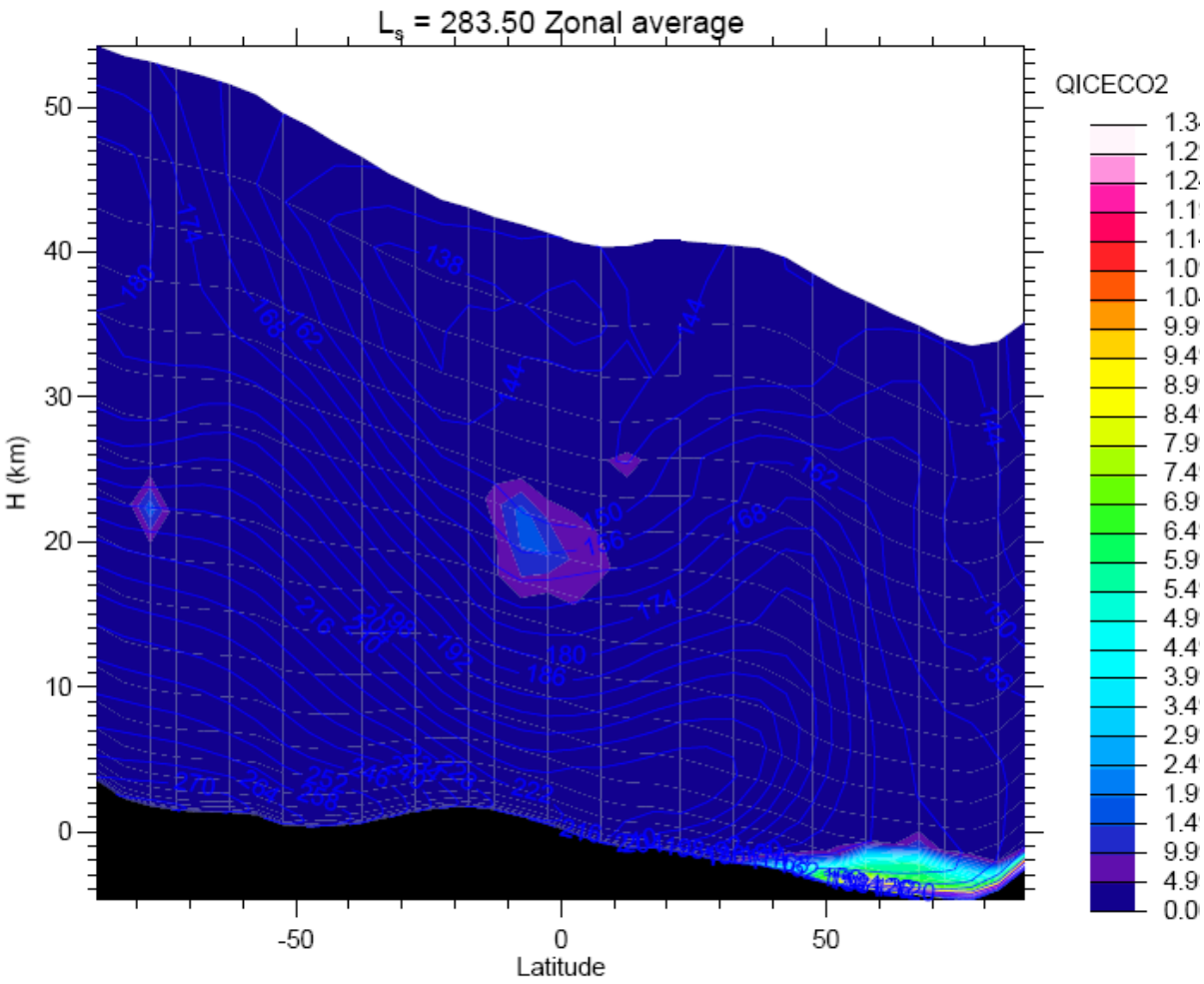

Figure 6.11: Same as Figure 6.7, except the obliquity of Mars is set to 40°.

Bibliography

Aharonson, O., M. T. Zuber, D. E. Smith, G. A. Neumann, W. C. Feldman, and T. H. Prettyman (2004), Depth, distribution, and density of CO2 deposition on Mars, *J. Geophys. Res.*, *109*(E5), 10.

Basu, S., M. I. Richardson, and R. J. Wilson (2004), Simulation of the Martian dust cycle with the GFDL Mars GCM, *J. Geophys. Res.*, *109*(E11).

Basu, S., J. Wilson, M. Richardson, and A. Ingersoll (2006), Simulation of spontaneous and variable global dust storms with the GFDL Mars GCM, *J. Geophys. Res.*, *111*(E9), 33.

Bibring, J. P., Y. Langevin, F. Poulet, A. Gendrin, B. Gondet, M. Berthe, A. Soufflot, P. Drossart, M. Combes, G. Bellucci, V. Moroz, N. Mangold, B. Schmitt, and O. Team (2004), Perennial water ice identified in the south polar cap of Mars, *Nature*, *428*(6983), 627-630.

Boynton, W. V., W. C. Feldman, S. W. Squyres, T. H. Prettyman, J. Bruckner, L. G. Evans, R. C. Reedy, R. Starr, J. R. Arnold, D. M. Drake, P. A. J. Englert, A. E. Metzger, I. Mitrofanov, J. I. Trombka, C. d'Uston, H. Wanke, O. Gasnault, D. K. Hamara, D. M. Janes, R. L. Marcialis, S. Maurice, I. Mikheeva, G. J. Taylor, R. Tokar, and C. Shinohara (2002), Distribution of hydrogen in the near surface of Mars: Evidence for subsurface ice deposits, *Science*, *297*(5578), 81-85.

Byrne, S., and A. P. Ingersoll (2003), A Sublimation Model for Martian South Polar Ice Features, *Science*, *299*, 1051-1053.

Byrne, S., M. T. Zuber, and G. A. Neumann (2008), Interannual and seasonal behavior of Martian residual ice-cap albedo, *Planet Space Sci.*, *56*(2), 194-211.

Christensen, P. R., D. L. Anderson, S. C. Chase, R. T. Clancy, R. N. Clark, B. J. Conrath, H. H. Kieffer, R. O. Kuzmin, M. C. Malin, J. C. Pearl, T. L. Roush, and M. D. Smith (1998), Results from the Mars Global Surveyor Thermal Emission Spectrometer, *Science*, *279*, 1692-1698.

Clancy, R. T., B. J. Sandor, M. J. Wolff, P. R. Christensen, M. D. Smith, J. C. Pearl, B. J. Conrath, and R. J. Wilson (2000), An intercomparison of ground-based millimeter, MGS TES, and Viking atmospheric temperature measurements: Seasonal and interannual variability of temperatures and dust loading in the global Mars atmosphere, *J. Geophys. Res.*, *105*(E4), 9553-9571.

Colaprete, A., and O. B. Toon (2002), Carbon dioxide snow storms during the polar night on Mars, *J. Geophys. Res.*, *107*(E7), 16.

Colaprete, A., and O. B. Toon (2003), Carbon dioxide clouds in an early dense Martian atmosphere, *J. Geophys. Res.*, *108*(E4), 23.

Colaprete, A., J. R. Barnes, R. M. Haberle, J. L. Hollingsworth, H. H. Kieffer, and T. N. Titus (2005), Albedo of the south pole on Mars determined by topographic forcing of atmosphere dynamics, *Nature*, *435*(7039), 184-188.

Colaprete, A., J. R. Barnes, R. M. Haberle, and F. Montmessin (2008), CO_2 clouds, CAPE and convection on Mars: Observations and general circulation modeling, *Planet Space Sci.*, *56*(2), 150-180.

De Pater, I., and J. J. Lissauer (2001), *Planetary Sciences*, Cambridge University Press, Cambridge.

Eluszkiewicz, J., J. L. Moncet, T. N. Titus, G. B. Hansen, and Jg (2005), A microphysically-based approach to modeling emissivity and albedo of the martian seasonal caps, *Icarus*, *174*(2), 524-534.

Eluszkiewicz, J., R.S, Hemler, L.D.Mahlman, et al. (2002), Sensitivity of age-of-air calculations to the choice of advection scheme, *J. Atmos. Sci.*, *57*(19), 3185-3201.

Feldman, W. C., W. V. Boynton, R. L. Tokar, T. H. Prettyman, O. Gasnault, S. W. Squyres, R. C. Elphic, D. J. Lawrence, S. L. Lawson, S. Maurice, G. W. McKinney, K. R. Moore, and R. C. Reedy (2002), Global distribution of neutrons from Mars: Results from Mars Odyssey, *Science*, *297*(5578), 75-78.

Feldman, W. C., T. H. Prettyman, W. V. Boynton, J. R. Murphy, S. Squyres, S. Karunatillake, S. Maurice, R. L. Tokar, G. W. McKinney, D. K. Hamara, N. Kelly, and K. Kerry (2003), CO_2 frost cap thickness on Mars during northern winter and spring, *J. Geophys. Res.*, *108*(E9), 8.

Feldman, W. C., T. H. Prettyman, S. Maurice, J. J. Plaut, D. L. Bish, D. T. Vaniman, M. T. Mellon, A. E. Metzger, S. W. Squyres, S. Karunatillake, W. V. Boynton, R. C. Elphic, H. O. Funsten, D. J. Lawrence, and R. L. Tokar (2004), Global distribution of near-surface hydrogen on Mars, *J. Geophys. Res.*, *109*(E09006).

Fenton, L. K., P. E. Geissler, and R. M. Haberle (2007), Global warming and climate forcing by recent albedo changes on Mars, *Nature*, *446*(7136), 646-649.

Forget, F., F. Hourdin, and O. Talagrand (1998), CO_2 snowfall on Mars: Simulation with a general circulation model, *Icarus*, *131*(2), 302-316.

Forget, F., F. Hourdin, R. Fournier, C. Hourdin, O. Talagrand, M. Collins, S. R. Lewis, P. L. Read, and J. P. Huot (1999), Improved general circulation models of the Martian atmosphere from the surface to above 80 km, *J. Geophys. Res.*, *104*(E10), 24155-24175.

Guo, X., V. Natraj, D. R. Feldman, R. J. D. Spurr, R. Shia, S. P. Sander, and Y. Yung (2007), Retrieval of ozone profile from ground-based measurements with polarization: A synthetic study, *J. Quant. Spectrosc. Radiat. Transf.*, *103*(1), 175-192.

Guo, X., W. G. Lawson, M. I. Richardson, and A. D. Toigo (submitted-a), Fitting the Viking Lander surface pressure cycle with a Mars General Circulation Model, *J. Geophys. Res.*

Guo, X., M. I. Richardson, A. Soto, and A. D. Toigo (submitted-b), On the mystery of the perennial carbon dioxide cap at the south pole of Mars, *J. Geophys. Res.*

Haberle, R. M., F. Forget, A. Colaprete, J. Schaeffer, W. V. Boynton, N. J. Kelly, and M. J. Chamberlain (2008), The effect of ground ice on the Martian seasonal CO_2 cycle, *Planet Space Sci.*, *56*(2), 251-255.

Heavens, N. (personal communication).

Herr, K. C., and G. C. Pimentel (1970), Evidence for solid carbon dioxide in upper atmosphere of Mars, *Science*, *167*(3914), 47-49.

Hess, S. L., R. M. Henry, C. B. Leovy, J. A. Ryan, and J. E. Tillman (1977), Meteorological results from the surface of Mars: Viking 1 and 2, *J. Geophys. Res.*, *82*(28), 4559-4574.

Holton, J. R. (2004), *Introduction to Dynamic Meteorology*, 4th ed., 535 pp., Academic Press.

Hourdin, F., P. Levan, F. Forget, and O. Talagrand (1993), Meteorologucal variability and the annual surface pressure cycle on Mars, *J. Atmos. Sci.*, *50*(21), 3625-3640.

Ingersoll, A. P. (1970), Mars - occerrence of liquid water, *Science*, *168*(3934), 972-973.

Ivanov, A. B., and D. O. Muhleman (2001), Cloud reflection observations: Results from the Mars Orbiter Laser Altimeter, *Icarus*, *154*, 190-206.

Jakosky, B. M. (1983a), The role of seasonal reservoirs in the Mars water cycle : II. Coupled models of the regolith, the polar caps, and atmospheric transport, *Icarus*, *55*(1), 19-39.

Jakosky, B. M. (1983b), The role of seasonal reservoirs in the Mars water cycle : I. Seasonal exchange of water with the regolith *Icarus*, *55*(1), 1-18.

James, P. B., H. H. Kieffer, and D. A. Paige (1992), The seasonal cycle of carbon dioxide on Mars, in *Mars*, edited by H. H. Kieffer, et al., The University of Arizona Press.

James, P. B., R. T. Clancy, S. W. Lee, L. J. Martin, R. B. Singer, E. Smith, R. A. Kahn, R. W. Zurek, and Pa (1994), Monitoring Mars with the Hubble-Space-Telescope - 1990-1991 Observations, *Icarus*, *109*(1), 79-101.

James, P. B., B. A. Cantor, M. C. Malin, K. Edgett, M. H. Carr, G. E. Danielson, A. P. Ingersol, M. E. Davies, W. K. Hartmann, A. S. McEwen, L. A. Soderblom, P. C. Thomas, and J. Veverka (2000), The 1997 spring regression of the Martian south polar cap: Mars Orbiter camera observations, *Icarus*, *144*(2), 410-418.

James, P. B., B. P. Bonev, M. J. Wolff, and Jg (2005), Visible albedo of Mars' south polar cap: 2003 HST observations, *Icarus*, *174*(2), 596-599.

Kelly, N. J., W. V. Boynton, K. Kerry, D. Hamara, D. Janes, R. C. Reedy, K. J. Kim, and R. M. Haberle (2006), Seasonal polar carbon dioxide frost on Mars: CO_2 mass and columnar thickness distribution, *J. Geophys. Res.*, *111*(E3), 12.

Kieffer, H. H., T. Z. martin, A. R. Peterfreund, B. M. Jakosky, E. D. Miner, and F. Don Palluconi (1977), Thermal and albedo mapping of Mars during the Viking primary mission, *J. Geophys. Res.*, *82*(28), 4249-4291.

Kieffer, H. H. (1979), Mars south polar spring and summer temperature: A residual CO_2 frost, *J. Geophys. Res.*, *84*, 8263-8288.

Kieffer, H. H., T. N. Titus, K. F. Mullins, and P. R. Christensen (2000), Mars south polar spring and summer behavior observed by TES: Seasonal cap evolution controlled by frost grain size, *J. Geophys. Res.*, *105*(E4), 9653-9699.

Kieffer, H. H., and T. N. Titus (2001), TES mapping of Mars' north seasonal cap, *Icarus*, *154*(1), 162-180.

Krasnopolsky, V. A., J. P. Maillard, and T. C. Owen (2004), Detection of methane in the Martian atmosphere: Evidence for life?, *Icarus*, *172*, 537-547.

Laskar, J. (1990), The chaotic motion of the solar system. A nummerical estimate of the size of the chaotic zones., *Icarus*, *88*, 266-291.

Laskar, J., B. Levrard, and J. F. Mustard (2002), Orbital forcing of the martian polar layered deposits, *Nature*, *419*, 375-377.

Leighton, R. B., and B. C. Murray (1966), Behavior of carbon dioxide and other volatiles on Mars, *Science*, *153*(3732), 136-144.

Leovy, C. (2001), Weather and Climate on Mars, *Nature*, *412*(6843), 245-249.

Maattanen, A., H. Vehkamaki, A. Lauri, S. Merikallio, J. Kauhanen, H. Savijarvi, and M. Kulmala (2005), Nucleation studies in the Martian atmosphere, *J. Geophys. Res.*, *110*(E2), 12.

Martin, T. Z. (1986), Thermal infrared opacity of the Mars atmosphere, *Icarus*, *66*(1), 2-21.

Menemenlis, D., I. Fukumori, and T. Lee (2005), Using Green's Functions to calibrate and ocean general circulation model, *Mon. Weather Rev.*, *133*, 1224-1240.

Mischna, M. A., J. F. Kasting, A. Pavlov, and R. Freedman (2000), Influence of carbon dioxide clouds on early martian climate, *Icarus*, *145*(2), 546-554.

Mumma, M. J., G. L. Villanueva, R. E. Novak, T. Hewagama, B. P. Bonev, M. A. DiSanto, A. M. Mandell, and M. D. Smith (2009), Strong release of methane on Mars in norther summer 2003, *Science Express*.

Nelli, S. M., J. R. Murphy, A. L. Sprague, W. V. Boynton, K. E. Kerry, D. M. Janes, and A. E. Metzger (2007), Dissecting the polar dichotomy of the noncondensable gas enhancement on Mars using the NASA Ames Mars General Circulation Model, *J. Geophys. Res.*, *112*(E08S91).

Neumann, G. A., D. E. Smith, and M. T. Zuber (2003), Two Mars years of clouds detected by the Mars Orbiter Laser Altimeter, *J. Geophys. Res.*, *108*(E4), 17.

Neumann, G. A., M. T. Zuber, M. A. Wieczorek, P. J. McGovern, F. G. Lemoine, and D. E. Smith (2004), Crustal structure of Mars from gravity and topography, *J. Geophys. Res.*, *109*(E08002).

Newman, C. E., S. R. Lewis, P. L. Read, and F. Forget (2002a), Modeling the Martian dust cycle - 2. Multiannual radiatively active dust transport simulations, *J. Geophys. Res.*, *107*(E12), 15.

Newman, C. E., S. R. Lewis, P. L. Read, and F. Forget (2002b), Modeling the Martian dust cycle - 1. Representations of dust transport processes, *J. Geophys. Res.*, *107*(E12), 18.

Newman, C. E., S. R. Lewis, and P. L. Read (2005), The atmospheric circulation and dust activity in different orbital epochs on Mars, *Icarus*, *174*(1), 135-160.

Owen, T., K. Biemann, D. R. Rushneck, J. E. Biller, D. W. Howarth, and A. L. Lafleur (1977), The composition of the atmosphere at the surface of Mars, *J. Geophys. Res.*, *82*(28), 4635–4639.

Paige, D. A. (1985), The annual heat balance of the Martian polar caps from VIking observations, California Institute of Technology, Pasadena.

Paige, D. A., and A. P. Ingersoll (1985), Annual heat balance of the Martian polar caps: Viking observations, *Science*, *228*(4704), 1160-1168.

Paige, D. A., K. E. Herkenhoff, and B. C. Murray (1990), Mariner-9 observations of the south polar-cap of Mars: evidence for residual CO_2 frost *J. Geophys. Res.*, *95*, 1319-1335.

Paige, D. A. (1992), The thermal stability of near-surface ground ice on Mars, *Nature*, *356*, 43-45.

Paige, D. A., J. E. Bachman, and K. D. Keegan (1994), Thermal and albedo mapping of the polar regions of Mars using Viking thermal mapper observations 1. North polar region, *J. Geophys. Res.*, *99*(E12), 25959-25991.

Paige, D. A., and K. D. Keegan (1994), Thermal and albedo mapping of the polar regions of Mars using Viking thermal mapper observations 2. South polar region, *J. Geophys. Res.*, *99*(E12), 25993-26013.

Pollack, J. B., T. Roush, F. Witteborn, J. Bregman, D. Wooden, C. Stoker, O. B. Toon, D. Rank, B. Dalton, and R. Freedman (1990), Thermal emission-spectra of Mars (5.4-10.5-MU-M) - Evidence for sulfates, carbonates, and dydrates, *J. Geophys. Res.*, *95*(B9), 14595-14627.

Pollack, J. B., R. M. Haberle, J. R. Murphy, J. Schaeffer, and H. Lee (1993), Simulations of the general-circulation of the Martian atmosphere .2. seasonal pressure variations, *J. Geophys. Res.*, *98*(E2), 3149-3181.

Putzig, N. E., M. T. Mellon, K. A. Kretke, and R. E. Arvidson (2005), Global thermal inertia and surface properties of Mars from the MGS mapping mission, *Icarus*, *173*, 325-341.

Richardson, M. I. (1998), Comparison of microwave and infrared measurements of Martian atmospheric temperatures: Implications for short-term climate variability, *J. Geophys. Res.*, *103*(E3), 5911-5918.

Richardson, M. I., and R. J. Wilson (2002a), A topographically forced asymmetry in the martian circulation and climate, *Nature*, *416*(6878), 298-301.

Richardson, M. I., and R. J. Wilson (2002b), Investigation of the nature and stability of the Martian seasonal water cycle with a general circulation model, *J. Geophys. Res.*, *107*(E5), 29.

Richardson, M. I., R. J. Wilson, and A. V. Rodin (2002), Water ice clouds in the Martian atmosphere: General circulation model experiments with a simple cloud scheme, *J. Geophys. Res.*, *107*(E9), 29.

Richardson, M. I., and M. A. Mischna (2005), Long-term evolution of transient liquid water on Mars, *J. Geophys. Res.*, *110*(E3), 21.

Richardson, M. I., A. D. Toigo, and C. E. Newman (2007), PlanetWRF: A general purpose, local to global numerical model for planetary atmospheric and climate dynamics, *J. Geophys. Res.*, *112*(E9), 29.

Saunders, R. S., R. E. Arvidson, G. D. Badhwar, W. V. Boynton, R. P. Christensen, F. A. cucinotta, W. C. Feldman, R. G. Gibbs, C. K. Jr., M. R. Landano, R. A. Mase, G. W.

McSmith, M. A. Meyer, I. G. Mitrofanov, G. D. Pace, J. J. Plaut, W. P. Sidney, D. A. Spencer, T. W. Thompson, and C. J. Zeitlin (2004), 2001 Mars Odyssey mission summary, *Space Sci. Rev.*, *110*, 1-36.

Schmidt, F., S. Doute, B. Schmitt, M. Vincendon, J.-P. Bibring, Y. Laugevin, and T. O. Team (2009), Albedo control of seasonal south polar cap recession on Mars, *Icarus*, *200*, 374-394.

Schorghofer, N., and O. Aharonson (2005), Stability and exchange of subsurface ice on Mars, *J. Geophys. Res.*, *110*(E05003).

Smith, D. E., M. T. Zuber, and G. A. Neumann (2001), Seasonal variations of snow depth on Mars, *Science*, *294*(5549), 2141-2146.

Smith, M. D. (2002), The annual cycle of water vapor on Mars as observed by the Thermal Emission Spectrometer, *J. Geophys. Res.*, *107*(E11), 19.

Smith, M. D., R. J. Conrath, J. C. Pearl, and P. R. Christensen (2002), Thermal Emission Spectrometer observations of Martian planet-encircling dust storm 2001A, *Icarus*, *157*(1), 259-263.

Smith, M. D. (2004), Interannual variability in TES atmospheric observations of Mars during 1999-2003, *Icarus*, *167*(1), 148-165.

Sobel, A. H., R. A. Plumb, and D. W. Waugh (1997), Methods of calculating transport across the polar vortex edge, *J. Atmos. Sci.*, *54*(18), 2241-2260.

Sprague, A. L., W. V. Boynton, K. E. Kerry, D. M. Janes, D. M. Hunten, K. J. Kim, R. C. Reedy, and A. E. Metzger (2004), Mars' south polar Ar enhancement: A tracer for south polar seasonal meridional mixing, *Science*, *306*(5700), 1364-1367.

Sprague, A. L., W. V. Boynton, K. E. Kerry, D. M. Janes, N. J. Kelly, M. K. Crombie, S. M. Nelli, J. R. Murphy, R. C. Reedy, and A. E. Metzger (2007), Mars' atmospheric argon: Tracer for understading Martian atmospheric circulation and dynamics, *J. Geophys. Res.*, *112*(E03S02).

Szwast, M. A., M. I. Richardson, and A. R. Vasavada (2006), Surface dust redistribution on Mars as observed by the Mars Global Surveyor and Viking orbiters, *J. Geophys. Res.*, *111*(E11), 36.

Tillman, J. E. (1988), Mars global atmospheric oscillations: Annually synchronized, transient normal mode oscillations and the triggering of global dust storms, *J. Geophys. Res.*, *93*, 9433-9451.

Tillman, J. E., N. C. Johnson, P. Guttorp, and D. B. Percival (1993), The Martian annual atmospheric pressure cycle: Years without great dust storms, *J. Geophys. Res.*, *98*(E6), 10963-10971.

Tobie, G., F. Forget, and F. Lott (2003), Numerical simulation of the winter polar wave clouds observed by Mars Global Surveyor Mars Orbiter Laser Altimeter, *Icarus*, *164*(1), 33-49.

Wang, H., and A. P. Ingersoll (2002), Martian clouds observation by Mars Global Surveyor Mars Orbiter Camera, *J. Geophys. Res.*, *107*(E10).

Watters, T. R., P. J. McGovern, and R. P. I. III (2007), Hemispheres apart: The crustal dichotomy on Mars, *Annu. Rev. Earth Planet. Sci.*, *35*, 621-652.

Waugh, D. W., and R. A. Plumb (1993), Contour advection with surgery: A technique for investigating finescale structure in tracer transport, *J. Atmos. Sci.*, *51*(4), 530-540.

Waugh, D. W., R. A. Plumb, J. W. Elkins, D. W. Fahey, K. A. Boering, G. S. Dutton, C. M. Volk, E. Keim, R. S. Gao, B. C. Daube, S. C. Wofsy, M. Loewenstein, J. R. Podolske, K. R. Chan, M. H. Proffitt, K. Kelly, P. A. Newman, and L. R. Lait (1997), Mixing of polar vortex air into middle latitudes as revealed by tracer-tracer scatterplots, *J. Geophys. Res.*, *102*(11D), 13119-13134.

Weiss, B. P., and A. P. Ingersoll (2000), Cold spots in the Martian polar regions: Evidence of carbon dioxide depletion?, *Icarus*, *144*(2), 432-435.

Wilson, R. J., and K. Hamilton (1996), Comprehensive model simulation of thermal tides in the Martian atmosphere, *J. Atmos. Sci.*, *53*(9), 1290-1326.

Wood, S. E., and D. A. Paige (1992), Modeling the Martian seasonal CO_2 cycle .1. Fitting the Viking Lander pressure curves, *Icarus*, *99*(1), 1-14.

Wood, S. E. (1999), Nucleation and growth of CO_2 ice crystals in the Martian atmosphere, UCLA, Westwood.

Zuber, M. T., S. C. Solomon, R. J. Phillips, D. E. Smith, G. L. Tyler, O. Aharonson, G. Balmino, W. B. Banerdt, J. W. Head, C. L. Johnson, F. G. lemoine, P. J. McGovern, G. A. Neumann, D. D. Rowlands, and S. Zhong (2000), Internal structure and early thermal evolution of Mars from Mars Global Surveyor topography and gravity, *Science*, *287*, 1788-1793.

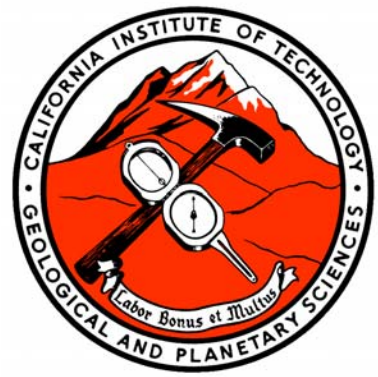
CALIFORNIA INSTITUTE OF TECHNOLOGY
GEOLOGICAL AND PLANETARY SCIENCES
Labor Bonus et Multus